A monoclonal antibody targeting nonjunctional claudin-1 inhibits fibrosis in patient-derived models by modulating cell plasticity

Natascha Roehlen, Antonio Saviano, Houssein El Saghire, Emilie Crouchet, Zeina Nehme, Fabio del Zompo, Frank Juehling, Marine Oudot, Sarah C. Durand, François Ht Duong, et al.

▶ **To cite this version:**

Natascha Roehlen, Antonio Saviano, Houssein El Saghire, Emilie Crouchet, Zeina Nehme, et al.. A monoclonal antibody targeting nonjunctional claudin-1 inhibits fibrosis in patient-derived models by modulating cell plasticity. Science Translational Medicine, 2022, 14 (676), 10.1126/scitranslmed.abj4221 . hal-04045641

HAL Id: hal-04045641
https://hal.science/hal-04045641v1

Submitted on 24 Mar 2023

HAL is a multi-disciplinary open access archive for the deposit and dissemination of scientific research documents, whether they are published or not. The documents may come from teaching and research institutions in France or abroad, or from public or private research centers.

L'archive ouverte pluridisciplinaire **HAL**, est destinée au dépôt et à la diffusion de documents scientifiques de niveau recherche, publiés ou non, émanant des établissements d'enseignement et de recherche français ou étrangers, des laboratoires publics ou privés.

A monoclonal antibody targeting non-junctional Claudin-1 inhibits fibrosis in patient-derived models by modulating cell plasticity

Authors: Natascha Roehlen[1]†, Antonio Saviano[1,2]†, Houssein El Saghire[1], Emilie Crouchet[1], Zeina Nehme[1], Fabio Del Zompo[1], Frank Jühling[1], Marine A. Oudot[1], Sarah C. Durand[1], François H.T. Duong[1], Sara Cherradi[1], Victor Gonzalez Motos[1], Nuno Almeida[1], Clara Ponsolles[1], Laura Heydmann[1], Tessa Ostyn[3], Antonin Lallement[1,4], Patrick Pessaux[1,2], Emanuele Felli[1,2], Andrea Cavalli[5], Jacopo Sgrignani[5], Christine Thumann[1], Olga Koutsopoulos[1], Bryan C. Fuchs[6#], Yujin Hoshida[7], Maike Hofmann[8], Mogens Vyberg[9], Birgitte Martine Viuff[10], Elisabeth D. Galsgaard[10], Greg Elson[11], Alberto Toso[11], Markus Meyer[11], Roberto Iacone[11], Tamas Schweighoffer[11], Geoffrey Teixeira[11], Solange Moll[12], Claudio De Vito[12], Tania Roskams[3], Irwin Davidson[4], Danijela Heide[13], Mathias Heikenwälder[13], Mirjam B. Zeisel[1§], Joachim Lupberger[1], Laurent Mailly[1], Catherine Schuster[1], Thomas F. Baumert[1,2,15*]

Affiliations:

[1]Université de Strasbourg, Inserm, Institut de Recherche sur les Maladies Virales et Hépatiques UMR-S1110, 67000 Strasbourg, France.

[2]Service d'hépato-gastroentérologie, Hôpitaux Universitaires de Strasbourg, 67000 Strasbourg, France.

[3]Department of Imaging and Pathology, University of Leuven, 3000 Leuven, Belgium.

[4]Department of Functional Genomics and Cancer, Institut de Génétique et de Biologie Moléculaire et Cellulaire, CNRS/INSERM/UNISTRA, 67400 Illkirch Cedex, France.

[5]Institute for Research in Biomedicine, Università della Svizzera Italiana, 6500 Bellinzona, Switzerland.

[6]Division of Gastrointestinal and Oncologic Surgery, Massachusetts General Hospital Cancer Center, Harvard Medical School, Boston, MA 02215, USA.

[7]Liver Tumor Translational Research Program, Harold C. Simmons Comprehensive Cancer Center, Division of Digestive and Liver Diseases, University of Texas Southwestern Medical Center, Dallas, TX 75390, USA.

[8]Department of Medicine II (Gastroenterology, Hepatology, Endocrinology and Infectious Diseases), Freiburg University Medical Center, Faculty of Medicine, University of Freiburg, 79106 Freiburg, Germany.

[9]Center of RNA Medicine, Department of Clinical Medicine, Aalborg University Copenhagen, 2450 København, Denmark, and Department of Pathology, Copenhagen University Hospital Hvidovre, 2650 Hvidovre, Denmark.

[10]Novo Nordisk A/S, 2760 Måløv, Denmark.

[11]Alentis Therapeutics, 4123 Allschwil, Switzerland.

[12]Department of Pathology, University Hospital of Geneva, 1205 Geneva, Switzerland.

[13]Division of Chronic Inflammation and Cancer, German Cancer Research Center, 69120 Heidelberg, Germany.

[14]Institut Universitaire de France, 75006 Paris, France.

† These authors contributed equally to this work and share fist authorship.

[#]Present address: Ferring Research Institute 4245 Sorrento Valley Boulevard San Diego, CA 92121, USA.

[§]Present address: Cancer Research Center of Lyon (CRCL), UMR Inserm 1052 CNRS 5286 Mixte CLB, Université de Lyon 1 (UCBL1), 69008 Lyon, France.

[*]Corresponding author. E-mail: thomas.baumert@unistra.fr.

Overline: FIBROSIS

One Sentence Summary: Claudin-1 is a mediator of and therapeutic target for organ fibrosis.

Abstract: Tissue fibrosis is a key driver of end-stage organ failure and cancer, overall accounting for up to 45% of deaths in developed countries. There is a large unmet medical need for anti-fibrotic therapies. Claudin-1 (CLDN1) is a member of the tight junction protein family. Although the role of CLDN1 incorporated in tight junctions is well established, the function of non-junctional CLDN1 (njCLDN1) is largely unknown. Using highly specific monoclonal antibodies targeting a conformation-dependent epitope of exposed njCLDN1, we show in patient-derived liver 3D fibrosis and human liver chimeric mouse models that CLDN1 is a previously unknown mediator and target for liver fibrosis. Targeting CLDN1 reverted inflammation-induced hepatocyte pro-fibrogenic signaling and cell fate and suppressed the myofibroblast differentiation of hepatic stellate cells. Safety studies of a fully humanized antibody in non-human primates did not reveal any serious adverse events even at high steady-state concentrations. Our results provide preclinical proof-of-concept for CLDN1-specific mAbs for treatment of advanced liver fibrosis and cancer prevention. Antifibrotic effects in lung and kidney fibrosis models further indicate a role of CLDN1 as a therapeutic target for tissue fibrosis across organs. In conclusion, our data pave the way for further therapeutic exploration of CLDN1-targeting therapies for fibrotic diseases in patients.

INTRODUCTION

Organ fibrosis is the result of excessive accumulation of extracellular matrix (ECM) that results from a wound healing response to repeated and chronic tissue injury. Organ fibrosis accounts for up to 45% of deaths in developed countries(*1*) and is a major risk factor for tumor development. Yet, approved therapies that aim to treat fibrosis are either absent, as for the liver, or show limited efficacy and safety as for the lung(*2-4*). Importantly, several key features and cellular drivers appear to be similar across different organs suggesting common pathways in the development of end-stage organ fibrosis(*1*).

The major causes of liver fibrosis are chronic hepatitis B (HBV) and C (HCV), alcoholic liver disease (ALD) and non-alcoholic steatohepatitis (NASH). Hepatocellular carcinoma (HCC) nearly always arises in the context of advanced liver fibrosis. Thus, direct anti-fibrotic agents are urgently needed to improve patient survival and outcome in advanced fibrosis by preventing liver disease progression, cancer risk and mortality(*2*).

Claudin-1 (CLDN1) is a member of the tight junction protein family(*5*) which is expressed in a junctional and non-junctional (nj) form. In the liver, njCLDN1 serves as a cell entry factor of HCV(*5, 6*), a major cause of liver fibrosis and cancer. Previous studies demonstrated that CLDN1 expression is upregulated in liver cirrhosis and HCC(*7*). Furthermore, CLDN1 overexpression induces epithelial-mesenchymal transition in liver cells(*8*), a pathogenic mechanism implicated in fibrosis and cancer.

Although its function within tight junctions for cell-cell-adhesion is well established, the role of njCLDN1 in disease biology and as a therapeutic target is largely unknown. We have previously developed monoclonal antibodies (mAbs) targeting the extracellular loop 1 of CLDN1 expressed on the hepatocyte basolateral membrane outside the tight junctions which potently

inhibit HCV cell entry into hepatocytes. Using a panel of mAbs targeting the ECL1 of CLDN1 combined with patient-derived models, we investigated the role of CLDN1 as a mediator and target for liver fibrosis.

RESULTS

CLDN1 expression is associated with liver fibrosis and disease progression

We first analyzed *CLDN1* gene expression in liver tissues of patients with chronic liver disease (HBV, HCV, or NASH) in several independent cohorts from Gene Expression Omnibus (GEO) and in a NASH cohort from the University of Strasbourg (table S1). *CLDN1* is upregulated in liver tissue of patients with liver disease of all major etiologies (**Fig. 1A**). *CLDN1* expression is associated with fibrotic disease progression in patients with NASH and HCV-infected individuals post transplantation(*12*) (**Fig. 1B**). Corroborating a pathogenetic role of CLDN1 for liver fibrosis, *CLDN1* is the most highly expressed *CLDN* family member in fibrotic liver (fig. S1A**)** and the only family member significantly upregulated in fibrosis (fig. S1B, $p<0.0001$).

We next investigated *CLDN1* expression in the liver at the single-cell level. Comprehensive expression studies including analysis of single cell (sc) and single nucleus (sn) RNA-seq data (**Fig. 1C-E,** fig. S2A-D) showed that *CLDN1* was highly expressed by hepatocytes and cholangiocytes ($p<0.0001$, U-test, respectively) with increasing expression towards liver bipotent progenitor cells(*17*) (**Fig. 1D**).

Within the liver microenvironment, activated hepatic stellate cells (aHSCs)/human liver myofibroblasts (HLMFs) robustly expressed *CLDN1* (**Fig. 1C,** fig. S2C). In contrast, *CDLN1* abundance in liver endothelial cells, monocytes/macrophages and lymphocytes appeared low or absent (**Fig. 1C, E,** fig. S2A-E). *CLDN1* expression in hepatocytes, cholangiocytes, progenitor cells and fibroblasts was confirmed at the protein level by in situ hybridization (ISH), immunohistochemistry (IHC) and double color immunofluorescence (**Fig. 1F-H** and fig. S2E).

In the fibrotic liver, scRNA analyses revealed that *CLDN1* was differentially expressed in a subpopulation of diseased hepatocytes at the epithelial-stromal interface (**Fig. 1E-F)** and

correlated with grade of de-differentiation towards a progenitor or bile-duct like cell type(*16*) ($p=3.75 \times 10^{-8}$, fig. S2F**)**. Within the mesenchymal cell compartment in fibrotic liver, *CLDN1* was highly expressed by mesothelial cells ($p<0.0001$, U-test, GSE136103, **Fig. 1E** and S2G**)** that have previously been described as fibrosis-associated fibroblast progenitor cells(*18, 19*) (fig. S2H). Taken together, our studies show that *CLDN1* is robustly expressed in hepatocytes, liver progenitor cells, cholangiocytes, mesenchymal cells including aHSCs/HLMFs and mesothelial cells. The up-regulation of *CLDN1* expression in fibrotic liver and its association with disease progression among different etiologies suggests a functional role in liver fibrosis.

To study the expression of njCLDN1 protein in human healthy and fibrotic liver, we used our well characterized panel of humanized CLDN1-specific antibodies specifically targeting a conformation-dependent epitope in the EL1 of CLDN1(*9-11*). Structural modeling revealed that this epitope is only accessible outside tight junctions (**Fig. 1I**). A subsequent genome-wide protein array demonstrated that these antibodies selectively bound CLDN1 without any cross-reactivity (fig. S3). Non-fibrotic or healthy liver tissues showed low or non-detectable njCLDN1 expression. In contrast, njCLDN1 was specifically upregulated in advanced fibrosis compared to total CLDN1 detected by an antibody targeting the intracellular CLDN1 C-terminal domain (**Fig. 1J**). Consistent with scRNASeq analyses (**Fig. 1E-F**), CLDN1 upregulation in cirrhosis was associated with epithelial cellular adhesion molecule (EPCAM) expression, corroborating a role of non-junctional CLDN1 for hepatocyte-cholangiocyte plasticity that is frequently observable as ductular reaction(*20*) (**Fig. 1K**). Immunofluorescence and confocal microscopy of aHSCs/HLMFs isolated from patients with non-alcoholic fatty liver disease (NAFLD) validated the presence of homogenous membranous CLDN1 expression in these stromal cells (fig. S4A-B).

We next aimed to elucidate drivers of *CLDN1* upregulation in chronic liver disease. TNF-α-NFκB signaling is a key pathway upregulated in chronic inflammatory liver tissue, liver fibrogenesis and carcinogenesis(*2*). Treatment of aHSCs with TNF-α significantly enhanced *CLDN1* expression (**Fig. 1L,** $p<0.0001$). A similar upregulation was observed in TNF-α-treated primary human hepatocytes, albeit to a lower magnitude (**Fig. 1L**). TNF-α-mediated upregulation was reduced after pharmacological inhibition of NFκB signaling in both aHSCs and primary human hepatocytes (**Fig. 1L**). To determine whether TNF-α treatment directly induced *CLDN1* expression via recruitment of NFκB to the *CLDN1* locus, we performed CUT&Tag and ChIP-seq using antibodies against the p65 subunit of NFκB in LX2 stellate cells with or without 24 hours treatment with TNF-α. Two previously defined ENCODE cis-regulatory elements upstream and downstream of *CLDN1* showed robust TNF-α-dependent p65 recruitment (**Fig. 1M**). These sites, previously identified as bound by NFκB in the ReMAP2022 data set, were validated by ChIP-seq and CUT&Tag (**Fig. 1M**). These data show that *CLDN1* is a direct target gene of TNF-α-NFκB pathway. Collectively, these results suggest TNF-α-NFκB signaling drives *CLDN1* upregulation in chronic inflammatory liver disease.

In vivo knockdown of CLDN1 using GalNAc siRNA technology reduces liver fibrosis

We next assessed the effect of in vivo CLDN1 knockdown in a patient-derived human liver chimeric mouse model that expresses human CLDN1 and closely recapitulates key features of clinical liver fibrosis based on *Fah*$^{-/-}$*/Rag2*$^{-/-}$*/Il2rg*$^{-/-}$ *(FRG)-NOD* mice robustly repopulated with primary human hepatocytes (*21*). To model NASH-induced advanced fibrosis, we applied a well-established long-term choline-deficient, L-amino acid-defined, high fat diet (CDA-HFD)(*22*) (**Fig. 2A**). For hepatocyte-specific *in vivo* knockdown of human CLDN1 we designed *CLDN1*

specific siRNAs covalently linked to a ligand containing three *N*-acetylgalactosamine (GalNAc) residues(*23*). After 12 weeks of diet, mice were randomized to 2 groups receiving either siRNA targeting *CLDN1* or control siRNA at 3mg/kg/week for 8 weeks. GalNAc siRNAs reduced CLDN1 protein expression in Huh7 liver cells and in vivo (fig. S5A, fig. S2B, C). Mice treated with *CLDN1*-targeting GalNAc siRNA showed significantly reduced fibrosis compared to mice treated with GalNac control siRNA (**Fig. 2B, C**, table S2, p=0.045). Moreover, mice in the CLDN1 knockdown group developed significantly fewer liver nodules (**Fig. 2B, C**, table S2, p=0.044). Taken together, these data suggest that CLDN1 plays a functional role in diet-induced liver fibrosis.

Targeting non-junctional CLDN1 reduces fibrosis in a human liver chimeric mouse model

We next evaluated the therapeutic effect of the humanized anti-human CLDN1 mAb H3L3 in the humanized mouse model of NASH-associated liver fibrosis (*21*). After 16 weeks of CDA-HFD diet, mice were randomized to 2 groups and received a weekly intraperitoneal (i.p.) injection of either the humanized CLDN1 mAb or an equivalent vehicle control for 8 weeks (**Fig. 2D**) while the diet was continued. Sirius red staining and fibronectin-1 (FN1) staining analysis revealed reduced liver fibrosis in independently performed studies (**Fig. 2E-H**, table S3). The anti-fibrotic effects were independent from the degree of human engraftment as shown by an absent correlation between human albumin (quantifying the humanization extent of the mice(*21*)) and fibrosis (fig. S5B). Humanized mice treated with CLDN1 mAb H3L3 showed downregulated hepatic gene expression of fibrosis markers, including tissue metallopeptidase inhibitor 1 (*Timp1*) and collagen type I alpha 1 chain (*Col1a1*) (**Fig. 2H**). Last, CLDN1 mAb-treated mice exhibited strongly

reduced plasma concentrations of C-reactive protein (CRP), a secreted inflammatory biomarker (fig. S5C).

Macroscopic examination of humanized livers revealed significantly reduced liver nodules in CLDN1 mAb-treated mice in both experiments (**Fig. 2G-H**, fig. S6 and table S3, $p<0.05$ and $p=0.009$ respectively in experiments 1 and 2). Detailed histopathology analyses revealed that the expansive nodules consisted of nodular growing mouse hepatocytes, reactive ductules, and human hepatocytes (fig. S6). Improvement of liver disease was associated with a marked effect on the expression of a clinical prognostic liver signature (PLS) predicting liver disease progression, outcome, and survival in patients with chronic liver disease including NASH(*25*). mAb treatment significantly reverted the poor-prognosis status of the PLS in the livers of humanized mice (fig. S5D).

A CLDN1-specific mAb reduces fibrosis and hepatocarcinogenesis in a mouse model of NASH fibrosis and HCC

To further validate anti-fibrotic and cancer-preventive effects of targeting CLDN1 in a fully immunocompetent mouse model, we engineered a murinized version of our previously established rat anti-human CLDN1 mAb(*9*). Despite lower affinity of these antibodies to mouse CLDN1 compared to the human one(*10*), the murinized CLDN1 mAb showed satisfactory target-engagement (fig. S7A-G).

In addition to CDA-HFD to induce NASH and fibrosis, we injected one dose of diethylnitrosamine (DEN) to accelerate hepatocarcinogenesis(*22*). At week 9, the mice were randomized in 2 groups and received a weekly i.p. injection of either the murinized CLDN1 mAb or an equivalent vehicle control for 16 weeks (**Fig. 3A).** Two mice in the control group died during

214 the experiment of unknown causes; no deaths occurred in the CLDN1 mAb-treated mice. Sirius
215 red staining and automated analysis of the collagen proportional area revealed significantly
216 reduced fibrosis in the CLDN1 mAb group with a relative median fibrosis improvement of 28.4%
217 (**Fig. 3B-C**, table S4, p=0.003). Furthermore, CLDN1 mAb-treated mice showed significantly
218 reduced abundance of FN1 (**Fig. 3B-C**, p=0.01) and *Col1a1* (**Fig. 3D**, p=0.004), two major
219 components of the fibrotic ECM(*2*). Reduced expression of *Acta2* and α-smooth muscle actin (α-
220 SMA) in a subset of the treated mice (**Fig. 3D,** fig. S8A-B) suggested reduced prevalence or
221 activity of HLMFs.

222 We observed a significant improvement of liver steatosis and NAFLD activity score in
223 CLDN1 mAb-treated animals (**Fig. 3E**, fig. S8A, respectively p=0.047 and p=0.0098). Similarly,
224 administration of the mAb was accompanied by a significant reduction of ALT concentrations
225 (p=0.033**)** whereas total bilirubin and alkaline phosphatase concentrations remained unchanged
226 (table S5). Staining for immune cell subpopulations revealed a moderately reduced infiltration of
227 $CD4^+$ T cells with no changes in the other main immune cell types in CLDN1 mAb-treated mice
228 (**Fig. 3F** and fig. S8C-D). In situ hybridization in paraffin-embedded tissues of inflammatory
229 cytokines demonstrated a reduction of *Ccl2* (fig. S8E), a cytokine involved in liver inflammation
230 and fibrosis and recruitment of circulating monocytes(*24*). In contrast, there was no effect on in
231 situ expression of *Ccl20* and *Cxcl10*.

232 Similarly to the humanized mouse model, we observed a robust reversion of the poor
233 prognosis status of the clinical PLS which predicts survival, fibrosis progression and HCC risk in
234 patients with chronic liver disease (fig. S8F). Macroscopic and microscopic examination of mouse
235 livers showed a marked difference in liver tumor development and burden (**Fig. 3G-I,** table S4).
236 Histopathological analyses revealed that the tumor nodules consisted of preneoplastic lesions or

well-differentiated HCC (fig. S9), confirming the validity of this model for HCC prevention studies as well as a robust inhibition of hepatocarcinogenesis by the antibody. Extensive safety studies including histopathology of major organs, complete serum chemistry, and renal and liver function tests did not show any detectable adverse effects (fig. S10, table S5).

Treatment with CLDN1-specific mAb inhibits fibrosis progression in a mouse model of biliary fibrosis

To validate the anti-fibrotic efficacy of the CLDN1 mAb in another mouse model of fibrosis, we assessed the effects of CLDN1 mAb in the 3,5-diethoxycarbonyl-1,4-dihydrocollidine (DDC) model, a widely accepted animal model for biliary fibrosis modeling obstructive cholestasis and fibrosis(*27*). Seven-week-old C57BL/6J were fed a 0.1% DDC-supplemented diet and after 1 week, when peri-biliary fibrosis was established, they were randomized into groups receiving weekly i.p. injection of CLDN1 mAb or vehicle control for 3 weeks (**Fig. 3J**). Sirius red staining and automated analysis of collagen proportional area revealed significantly reduced fibrosis and total FN1 (**Fig. 3L-K,** table S6, respectively $p<0.0001$ and $p=0.001$) as well as reduced Ishak score (**Fig. 3M,** table S6).

Validation of the profibrogenic role of CLDN1 in patient-derived 3D liver fibrosis and NASH models

We next validated the antifibrotic effects of the CLDN1 mAb in patient-derived *ex vivo* models. The 3D ExVivo Human Liver Tissue model (Organovo) mimics distinct features of NASH and fibrosis and allows the assessment of liver disease therapeutics(*28*) (**Fig. 4A**). In this human NASH model, mAb treatment reduced hepatocyte ballooning and macro- and micro-steatosis in

three out of four tissue preparations (**Fig. 4B**). Image-based quantification of the collagen proportional area revealed that median fibrosis in CLDN1 mAb-treated ExVivo tissues was significantly reduced compared to control mAb-treated tissues (2.69% vs. 6.14%, **Fig. 4C**, $p<0.0001$).

We studied effects of CLDN1 on fibrosis in patient-derived human liver spheroids, 3D micro-tissues recapitulating the liver microenvironment(*29*). Liver tissues from patients with and without chronic liver disease and fibrosis (table S7) were dissociated and cultured in ultra-low attachment plates (**Fig. 4D)**. This protocol allows the formation of patient-derived spheroids harboring original liver cell populations (**Fig. 4E**). Treatment with a profibrogenic medium containing transforming growth factor beta (TGF-β), free fatty acids (FFA) and lipopolysaccharides (LPS) induced the expression of *COL1A1*, *COL3A1*, *COL4A1*, and *CTGF* (**Fig. 4F**). Treatment of patient spheroids with CLDN1 mAb reduced the induction of these pro-fibrogenic markers (**Fig. 4F**). Moreover, CLDN1 mAb treatment decreased collagen deposition compared to resmetirom, a NASH compound having reached late-stage clinical development (*30*) (**Fig. 4G**).

Last, we aimed to validate the effect of CLDN1 on the PLS predicting liver disease progression, survival and HCC risk in liver tissues from patients with advanced fibrosis(*31*). Liver slices of NASH patients with NASH with different stages of fibrosis (table S8) were incubated with CLDN1 mAb or control and analyzed for expression of the clinical PLS (**Fig. 4H**). Treatment with CLDN1 mAb significantly reverted the PLS from poor to good prognosis for samples of patients #1-4 (NASH fibrosis #1-#5, poor prognosis genes: false discovery rate (FDR) = 0.16, 0.16, 0.09, 0.17 and 0.28, respectively; good prognosis genes: FDR= 0.50, 0.004, 0.09, 0.20, 0.80, respectively, **Fig. 4I**).

Targeting CLDN1 reverses inflammation-induced perturbation of cell plasticity in hepatocytes, progenitor cells, and myofibroblasts

We next aimed to evaluate the molecular mechanism of the antifibrotic effect of the CLDN1-specific mAb. Given the association of CLDN1 expression with cell state, we assessed scRNA-seq-derived cell lineage marker genes in human liver chimeric mice side-by-side with transcriptomic data derived from a clinical cohort of NASH patients with mild or advanced fibrosis (**Fig. 5A**). Gene sets encompassing marker genes of the $EPCAM^+$ progenitor compartment were significantly enriched in patients with NASH and advanced fibrosis (Cell cluster maker genes C4, C39, C24, C7: NES=1.99, 2.05, 2.07, 2.19, FDR<0.001), whereas genes characterizing healthy mature hepatocytes were strongly downregulated (C30, C17, C14, C11: NES=-1.39, -1.71, -2.21, -2.23, FDR<0.02) (**Fig. 5B).** Similar results were obtained in fibrotic livers derived from two NASH fibrosis mouse models compared to corresponding regular diet mice (fig. S11A-B). Treatment with CLDN1 mAb considerably reverted the hepatocyte-progenitor cell plasticity in both mouse models (**Fig. 5C**, fig. S11C, D) suggesting that CLDN1-specific mAb treatment reverts the disease-induced immature progenitor phenotype of hepatocytes back to a mature phenotype.

We next examined the effect of CLDN1 on cell plasticity of mesenchymal cells in the DEN-CDAHFD mouse model. Expression of marker genes of $PDGFRA^+$ scar-associated myofibroblasts (table S9, markers from(*16*)) was induced both in livers of NASH patients with NASH with advanced fibrosis as well as fibrotic mouse livers (**Fig. 5D,** fig. S11E). CLDN1 mAb treatment significantly suppressed expression of these scar-associated myofibroblast gene signatures in the immunocompetent NASH fibrosis mouse model (FDR<0.001, **Fig. 5E**). Similarly, examining cell circuit modules driving cirrhosis in patients, we found reduced gene expression related to

myofibroblast differentiation and ECM production (module 1 and 24) as well as restoration of physiological hepatocyte metabolism (module 9, 22 and 23) (**Fig. 5F**, upper panel) in mice treated with CLDN1-specific mAb.

Collectively, our integrative analyses in patient liver tissues and patient-derived mouse models suggest that treatment with CLDN1 mAb reverses fibrosis-associated cell fate and plasticity in hepatocytes and fibroblasts.

Targeting CLDN1 reverses perturbation of liver cell circuits and signaling mediating chronic inflammation and fibrosis

To unravel the specific cell circuits and signaling pathways involved in liver disease progression in vivo and restored by mAb treatment, we analyzed transcriptional signatures of fibrosis- and carcinogenesis-related signaling in the mouse models (fig. S12A). Fibrotic mouse NASH livers exhibited upregulated fibrosis-associated pathways similar to NASH patients with NASH with advanced fibrosis (**Fig. 5F**). Treatment with CLDN1 mAb reversed the induction of these fibrogenic circuits, with the most pronounced effects on TNF-α-NFκB signaling (**Fig. 5F**). Similarly, carcinogenesis-associated pathways were upregulated in NASH patients with advanced fibrosis but suppressed by CLDN1 mAb treatment in both animal models (**Fig. 5F**). Similar results were obtained by unbiased GSEA of hallmark gene sets in both mouse models (fig. S12B). The suppression of key target pathways such as NFκB (RELA and RELB) and MAPK (p-p38) was confirmed by immunohistochemistry in the DEN-CDAHFD NASH fibrosis mouse model (**Fig. 5G,** fig. S12C-E).

CLDN1-specific mAb inhibits pro-fibrotic signaling and modulates cell-matrix interaction and plasticity in hepatocytes

Next, we investigated the specific effects of CLDN1 mAb on signaling and plasticity in the cell types identified in the expression and binding studies. Using stable CLDN1 knockout (KO) and pharmacological intervention, we found that CLDN1 is a driver of the poor prognosis status of the PLS in cell-based models(*25*) (fig. S13A-C). Reversal of the poor prognosis status was CLDN1 mAb dose-dependent (fig. S13C). RNA-seq and GSEA further confirmed mAb-mediated suppression of hepatocyte-progenitor cell plasticity (fig. S13D) as well as pro-fibrogenic and carcinogenic signaling (fig. S13E) in cell culture models of both viral and metabolic liver disease.

To study the molecular events after CLDN1 mAb target engagement, we identified the molecular partners of CLDN1 at the membrane of epithelial cells using Huh7 cells with high CLDN1 expression as a tractable model for immature liver epithelial cells. Co-immunoprecipitation of CLDN1 identified more than 300 proteins as potential CLDN1 interactants (data file S2). String analysis with clustering revealed 3 clusters of proteins interacting with CLDN1 (**Fig. 6A**): cell adhesion proteins, integrins and ECM proteins as well as proteins related to cell proliferation and fate. Epithelial growth factor receptor (EGFR), EPCAM, the ECM receptor integrin alpha 5 (ITGA5), and ECM component laminin 5 (LAMA5) were confirmed as molecular partners by Western blot analyses (**Fig. 6B**). Next, we investigated the consequences of these cell membrane molecular interactions on pro-fibrotic and pro-carcinogenic signaling mediated by these pathways. CLDN1 mAb treatment suppressed EGFR and extracellular signal-regulated kinases (ERK) phosphorylation (**Fig. 6C-D**) and inhibited SRC proto-oncogene, non-receptor tyrosine kinase (SRC) signaling, a key downstream pathway of cell-ECM mechanoreceptors(*32*). Plasma membrane isolation showed a decrease of SRC recruitment at the

cell membrane after treatment (**Fig. 6E**). Moreover, CLDN1 mAb inhibited SRC activation by phosphorylation in a 3D Huh7 spheroid model (**Fig. 6F**). Unbiased proteomic assessment of signaling in a Huh7-LX2 co-culture model using phospho-specific antibody capture arrays validated CLDN1 mAb-induced suppression of SRC family and MAPK kinase (p38) activation and revealed downregulation of other known profibrotic and pro-carcinogenic downstream effectors including CREB5 and TOR(*33*)(**Fig. 6G**). The effects of CLDN1 mAb on EGFR-MAPK and ITGA5-SRC signaling were further validated in precision cut liver slices (PCLS) of patient-derived tissues (fig. S14A) as well as in patient-derived multicellular spheroids exposed to profibrogenic injury (**Fig. 6H**). Besides SRC and EGFR, we detected reduced kinase activity of other kinases known to mediate fibrosis progression, such as IGF1R and IKK-E as well as reduced activity of kinases involved in carcinogenesis, including ARG, ABL, AKT1/2, and HER2 (**Fig. 6H**). A comparative analysis with a liver fibrosis kinome atlas suggests that CLDN1 mAb treatment in patient spheroids reverts the profibrogenic signaling cascade identified in patients with advanced liver fibrosis (fig. S14B)(*34*).

Collectively, our data indicate that CLDN1 interacts with EPCAM, EGFR, ITGA5, laminin, and other proteins at the cell membrane of liver epithelial cells. Target engagement of CLDN1 mAb with cell surface CLDN1 inhibits downstream profibrogenic and pro-carcinogenic signaling mediating cell plasticity, fibrogenesis, and carcinogenesis (fig. S14C).

Treatment with CLDN1-specific mAb modulates liver progenitor cell phenotype and plasticity

Given the high abundance of CLDN1 expression in liver progenitor cells and cholangiocytes, effects on liver cell plasticity might also be mediated via direct effects of CLDN1

mAb on ductal cells which play a role in fibrotic liver disease(*35*). The “ductular reaction”, a regenerative cholangiocyte and liver progenitor cell proliferation, has been reported as a potential anti-fibrotic target(*35*). We generated intrahepatic bile duct-derived organoids from human cirrhotic liver tissue and treated these cells with CLDN1 mAb or control mAb for 4 days. These organoids showed high expression of CLDN1 and progenitor markers (fig. S15A). CLDN1 mAb treatment modulated the phenotype of the organoids with an altered morphology, such as thinner walls and cystic deformation (**Fig. 7A, left panel**). Computational analysis of the organoid size further confirmed functional effects on organoid growth (**Fig. 7A, right panel**). Transcriptomic profiling of organoids by RNA-seq revealed pronounced effects of the antibody on liver organoid gene expression (**Fig. 7B**). Computational assessment indicated enrichment of upregulated genes into developmental pathways and downregulated genes into proliferative biological processes (**Fig. 7C**, fig. S15B-C) suggesting functional effects on cell proliferation and plasticity of CLDN1 mAb on progenitor cells and cholangiocytes. Validation of significant downregulation of the expression of liver progenitor cell marker TACSTD2/TROP2(*15*) in mAb-treated organoids confirmed the functional effect of treatment on cell plasticity (p=0.04, **Fig. 7D**).

CLDN1-specific mAb inhibits profibrogenic differentiation in aHSCs by interfering with TNF-α-NFκB signaling

We evaluated direct effects of CLDN1 mAb on mesenchymal cells by RNA-seq analysis of CLDN1 mAb-treated patient-derived aHSCs/HLMFs (**Fig. 7E**). Marker genes of scar-associated myofibroblasts type A (table S10), the major phenotype of fibrotic myofibroblasts(*16*),were significantly inhibited in CLDN1-mAb treated HLMFs (FDR<0.08, **Fig. 7E)**. Moreover, CLDN1 mAb strongly suppressed TNF-α-NFκB signaling in HLMFs as validated

by Western Blot analyses of the TNF-α canonical pathway (**Fig. 7F-H**). Assessment of TGF-β signaling did not reveal major effects of the antibody on the TGF-β canonical SMAD2/3 signaling pathway, but showed inhibition of TGF-β induced non-canonical pathways, such as pAKT, p-P38 and pERK signaling (**Fig. 7H, I**). Last, we confirmed direct downstream effects on myofibroblast effector functions. Indeed, CLDN1 mAb treatment of HLMFs from different donors (table S12) markedly inhibited key activation markers, including *ACTA2*, *COL1A1* and *FN1* (**Fig. 7J**).

CLDN1 is a candidate target for treatment of lung and kidney fibrosis

The mechanistic role of CLDN1 during fibrosis is not necessarily limited to the liver. Several studies have suggested a role of CLDN1 in the pathogenesis of chronic kidney disease(*37*). Upregulation of *CLDN1* expression in patients with glomerulonephritis as well as murine fibrotic kidneys(*38*) (**Fig. 8A**) suggests the involvement of *CLDN1* in the pathogenesis of renal fibrotic disease. Furthermore, *CLDN1* was significantly overexpressed in patients with idiopathic pulmonary fibrosis (IPF) with increasing expression along disease progression (p=0.03, **Fig. 8B**).

To investigate the role of CLDN1 as a therapeutic target in other organs, we used two state-of-the-art mouse models for kidney and lung fibrosis (**Fig. 8C**). Treatment with the murinized CLDN1-specific mAb (fig. S2) resulted in robust anti-fibrotic effects in the unilateral ureteral obstruction (UUO) mouse model of kidney fibrosis(*40*) (**Fig. 8D-E**, table S13). Moreover, histological assessment of mouse kidneys revealed suppression of macrophage infiltration by CLDN1 mAb (**Fig. 8F**).

We studied the effects of CLDN1 mAb in a bleomycin-induced pulmonary fibrosis mouse model and compared to dexamethasone, an off-label used drug with protective effects in patients

with lung fibrosis(*3*) (**Fig. 8C**). Treatment with CLDN1 mAb suppressed lung fibrosis in these animals (**Fig. 8G-H**, table S14). Similar to the liver, CLDN1 was expressed and regulated via TNF-α-NFκB signaling in both lung (**Fig. 8I-J**) and kidney fibroblasts (**Fig. 8J**). In line with the role of CLDN1 in liver cell fate and differentiation, treatment of IPF patient-derived myofibroblasts resulted in reversal of pro-fibrogenic lung fibroblast differentiation states(*41*) (**Fig. 8K**). CLDN1 mAb strongly suppressed expression of marker genes of $ACTA2^{+}$ myofibroblasts, $PLIN2^{+}$ lipomyofibroblasts, and $HAS1^{hi}$ fibroblasts (table S15-17). As observed in HLMFs, CLDN1 mAb-treatment suppressed TNFα-NFκB signaling in primary lung fibroblasts (**Fig. 8L**). These findings suggest CLDN1 as a candidate target for kidney and lung fibrosis which warrants further investigation.

ALE.F02, an CLDN1 therapeutic candidate antibody for treating human fibrotic diseases, is safe in cynomolgus monkeys

To ensure the safety of CLDN1 mAbs in a species with full human target homology and equivalent antibody affinity, we expanded toxicity studies to non-human primates (table S18). As a candidate for future human therapeutic applications, we chose a fully humanized variant which we designated ALE.F02. Differently from H3L3, the Fc region of the ALE.F02 molecule contains three mutations (L234F, L235E, and P331S) which have been introduced to reduce binding to Fc gamma receptors. In cynomolgus monkeys (*M. fascicularis*), the sequence of human CLDN1 and the antibody's binding epitope is 100% conserved. A rapid escalation protocol achieved safe, multiple weekly dosing up to the highest tested dose of 150 mg/kg. No major clinical changes were observed. Notably, there was no indication of NISCH syndrome in the animals, a condition caused by genetic CLDN1 deficiency in humans. These studies confirmed that CLDN1-targeting therapies

442 are safe *in vivo* and that ALE.F02 did not affect the integrity or barrier function of tight junctions.
443 Serum analysis indicated a dose-dependent, sustainable and effective antibody concentration in
444 macaques (fig. S16A). Simulations using the macaque data predicted that PK profiles in humans
445 with a single dose of ~3-10 mg/kg ALE-F02 would saturate CLDN1 for about 2 weeks (fig. S16B).
446
447

DISCUSSION

In this study we uncovered CLDN1 as a mediator and therapeutic target for tissue fibrosis. Using the liver as a model of chronic inflammation-associated fibrogenesis and carcinogenesis we show that targeting CLDN1 by highly specific mAbs robustly reduced fibrosis and tumor development in mouse models for NASH and biliary fibrosis; strongly reduces liver fibrosis in *ex vivo* patient-derived model; and reversed transcriptomic liver disease signatures predictive of liver fibrosis progression and HCC risk. A key strength of our study is its focus on authentic patient-derived model systems, the consistency of results across complementary model systems, different organs and patient cohorts supporting its validity and translatability into the clinic.

Our comprehensive analyses provide the following model for the molecular mechanism of CLDN1 mAb mediated anti-fibrotic effects: hepatocytes and their progenitors are the primary target cells of CLDN1 mAb antifibrotic effect. Our detailed gene expression analyses *in vivo* and in patients revealed that mAb treatment restores the hepatocyte fate by suppressing hepatocyte de-differentiation following epithelial liver injury. Target engagement at the hepatocyte cell membrane interferes with the interaction of CLDN1 with EPCAM, EGFR, ITGA5 as well as the ECM, resulting in inhibition of downstream signaling of well-established pro-fibrotic and pro-carcinogenic signaling pathways across organs, such as SRC and MAPK signaling.

The second cell type mediating the anti-fibrotic properties of the mAb are likely aHSCs/HLMFs which express CLDN1 in patients. CLDN1 mAb inhibits TNF-α-NFκB as well as non-canonical TGF-β signaling resulting in inhibition of myofibroblast activation and differentiation across organs. Cross-talk between liver epithelial cells and fibroblasts modulate the ECM with decreased collagen and fibronectin production. The reprogramming of hepatocytes and its microenvironment ultimately results in the attenuation of tissue fibrosis.

Our study has some limitations: First, we can not exclude that other signaling pathways or additional mechanistic events are at play mediating the anti-fibrotic effect of the antibodies. Second, while we used a large panel of complementary model systems including patient-derived models, any model system only partially recapitulates pathogenesis of fibrosis in patients.

The large majority of liver disease therapeutics target metabolism, inflammation or cell death, which are relevant in the early stage of disease(*42, 43*). A key differentiator of CLDN1-specific mAb is the combination of robust anti-fibrotic and HCC preventive effect, which addresses the key unmet medical need in advanced liver fibrosis.

Our study also provides the opportunity to develop companion biomarkers such as TIMP1 , a clinically applied read-out for liver fibrosis as part of the ELF score, or CTGF, a biomarker candidate for fibrosis across organs(*44, 45*). Furthermore, the potent effect on the PLS may enable to stratify patients at high risk for HCC and the highest need for treatment.

Our data demonstrate that the administration of the antibody is safe without detectable adverse and off-target effects. Safety studies in non-human primates demonstrate that even repeated high dose administration does not induce any major adverse effects and support further clinical development in humans.

Beyond the liver, our *in vivo* data suggest that CLDN1 is also a candidate target for kidney and lung fibrosis(*3, 4*). Our functional studies suggest common mechanisms across organs as demonstrated by similar inhibition profiles of lung fibroblast differentiation by CLDN1 mAb via interference with TNF-α-NFκB signaling. However, given the expression of CLDN1 in organ-specific cell types in the kidney(*37*) or lung(*46*), it is likely that also additional organ-specific mechanisms are at play.

493 Collectively, the development of CLDN1-specific mAb provides an opportunity for the
494 clinical development of a first-in-class compound for treatment of organ fibrosis, a major and
495 rapidly growing unmet medical need world-wide.
496

MATERIAL AND METHODS

Study design. Computational transcriptomic analyses were conducted in publicly available and own patient cohorts of chronic liver disease. Overall and cell-type specific target expression was characterized by immunohistochemistry, immunofluorescence and in situ hybridization of multiple non-fibrotic and fibrotic tissues of different patient cohorts. *In vivo* genetic knockdown studies using siRNA were performed to validate CLDN1 as a driver of liver fibrosis. NjCLDN1 targeted by highly specific mAbs was evaluated as a target to treat fibrosis in a large set of *in vivo* and *ex vivo* models. The molecular mechanism of action was studied by co-immunoprecipitation studies, transcriptomic and proteomic analyses in cell-based models of chronic liver disease, including patient-derived 3D ex vivo models, such as spheroids and liver organoids. Finally, in preparation for clinical translation, the pharmacological and safety properties of a humanized CLDN1 antibody was validated in non-human primates. Experiments were partially blinded and performed in triplicates in at least three independent experiments, unless otherwise stated. Patient tissues for *ex vivo* and *in vitro* studies were randomly assigned. Additional methods are available in the supplementary materials.

Human subjects and patient cohorts. For transcriptomic analyses and *ex vivo* perturbation studies human liver tissue samples were obtained from patients who had undergone liver resections for HCC, colorectal cancer metastasis, or cholangiocellular carcinoma between 2014 and 2022 at Strasbourg University Hospitals, France (DC-2016-2616 and RIPH2 LivMod IDRCB 2019-A00738-49, ClinicalTrial NCT04690972). All patients provided written informed consent and the protocol followed the ethical principles of the declaration of Helsinki and was approved by the local independent ethics committees. For CLDN1 expression analysis, liver tissues were obtained from local biobanks of the Department of Imaging & Pathology, KU Leuven, the University

Hospital Geneva, Pathology at Hvidovre University Hospital, Denmark or Indivumed, Hamburg. Demographic data and clinical characteristics of patients enrolled are summarized in table S1-S2 and S5-S6, respectively. Datasets of clinical cohorts with chronic liver disease (GSE34798, GSE83148, GSE49541), chronic kidney disease (GSE11585 and GSE60685), IPF (GSE2052, GSE53845, GSE24206) were selected following comprehensive database analysis, where we identified CLDN1 as part of the microarray data. GSE34798, GSE83148, GSE49541, GSE34798, GSE115857, GSE53845 and GSE24206 were analysed using *shinyGEO*(*47*) with expression values shown as log2 expression. All other microarray data were analysed using signal intensity values. Liver scRNA-seq data (GSE124395 and GSE136103) and snRNA-seq data (GSE185477) were obtained as Seurat objects and investigated.

Bioinformatic and statistical analyses. Human RNA-seq data was mapped using HISAT2 to the human genome hg19. Mouse RNA-seq data was mapped to the mouse genome mm10 and annotated using the Gencode vM15 gene annotation. Data from humanized mice were mapped similarly, but to an artificial genome consisting of all human (hg19) and mouse (mm10) chromosomes, and only reads mapping to human chromosomes were kept for further analysis as described(*48*). Reads were counted with htseq-count, and a differentially expression analysis was performed with DESeq2 applying GENCODE 19. Gene Set Enrichment Analysis (GSEA) was used for unbiased pathway analysis using Molecular Signature Database (MSigDB)(*49*). Unbiased assessment of HALLMARK(*49*), gene ontology and curated gene sets(*49*) were used for primary screening of clinically relevant signaling pathways and cell circuits in NASH liver tissue microarray data (GSE49541), that were then subsequently analyzed in RNA-seq data of our NASH mouse models. HALLMARK pathways were further analysed in an unbiased way in RNA-seq data from two NASH mouse models. GSEA of hepatocyte and $EPCAM^{+}$ bile duct cell signature

gene sets (C8, MSigDB, derived from scRNA-seq studies in human liver(*15*)) were used for evaluation of hepatocyte cell fate. Results from GSEA were adjusted for the false discovery rate (FDR). FDR<0.25 or FDR<0.05 was considered statistically significant. All other data was compared using Student's t-test when normally distributed (Shapiro-Wilk test) or non-parametric tests (U-test, Kruskal-Wallis test) when non-normally distributed. Functional results in patient-derived cells were compared using Wilcoxon matched paired test. P <0.05 and FDR<0.25 were considered statistically significant.

ACKNOWLEDGMENTS

The authors acknowledge the proteomics platform of IGBMC, where mass spectrometry analysis was performed supported by an ARC foundation grant (Orbitrap) and a Canceropôle Grand Est foundation grant. The authors thank the CRB (Centre de Ressources Biologiques-Biological Resource Centre) of the Strasbourg University Hospitals for the management of patient-derived liver tissue. The authors thank Dr. R. Bartenschlager (University of Heidelberg, Germany), Dr. C. Rice (Rockefeller University, New York, NY) for providing plasmids for production of HCVcc Jc1 strains, Dr. M. Evans (Mount Sinai Hospital, New York, NY) for providing mouse and human CLDN1 expression plasmids, Dr. F. Chisari (The Scripps Research Institute, La Jolla, CA) for the gift of Huh7.5.1 cells, Prof. G. Christofori (University of Basel) for the gift of Huh7 cell line, Dr. S. Friedman (Mount Sinai Hospital, New York) for the gift of the LX2 stellate cell line, Dr. F. Habersetzer (Strasbourg University Hospitals) for patient serum samples for isolation of infectious HBV and Dr. D. Root (Broad Institute of MIT and Harvard, Cambridge, MA) for providing expression plasmids for lentivirues and sgRNAs for CLDN1 KO. We thank Marie Parnot (Inserm U1110, University of Strasbourg) for help with proteomic studies, Mirian Fenandez-Vaquero and Jenny Hetzer (German Cancer Research Center, Heidelberg, Germany) for help in histopathology staining, Thomas Cagarelli (Dept. of Pathology, University of Geneva) and Dr. H. Jacobs (ICS Mouse Clinic, IGBMC, Illkirch) for histopathology analyses of part of the animal and human tissues, Prof. A. Schmitt-Graeff (Dept. of Pathology, University Hospital Freiburg), Prof. Antje Prasse (Hannover Medical School) for advice in histopathology analyses of liver and lung tissues, Mikhail Gromak (Department of Medicine II, University Freiburg) for the contribution to organoid studies, Dr. Meritxell Huch (Max Planck Institute, Dresden) for critical input in analysis of organoid studies and Dr. Lynda Audjehane (Human HepCell, Faculté

de Médecine Pierre et Marie Curie, Site Saint-Antoine, Paris, France) for providing human myofibroblasts for pilot staining experiments in the initial phase of the study.

FUNDING

Funding was obtained from the following grants: European Union ERC-AdG-2014 *HEPCIR #671231* (T.F.B.), European Union ERC-AdG-2020 *FIBCAN* #101021417 (T.F.B.) ,European Union ERC-PoC-2016 *PRELICAN #7555460* (T.F.B.), European Union ERC-PoC-2018 *HEPCAN* #862551 (T.F.B.), European Union ERC Consolidator grant *HepatoMetabopath* #683000 (M.H.), European Union H2020 *HEPCAR* #667273 (T.F.B. and M.H.), Fondation ARC www.fondation-arc.org *TheraHCC2.0* IHU201901299 (T.F.B.), ANRS Grant ECTZ103701 *CLAUDIN-1* (T.F.B.), SATT Conectus, University of Strasbourg (CANCLAU) (T.F.B.), French National Research Agency LABEX ANR-10-LABX-0028_*HEPSYS* (T.F.B.), German Research Foundation (DFG) RO 5983/1-1 (N.R.), C1 KU Leuven grant (C14/20/097) (T.R.), DFG-SFB-1479 OncoEscape (TP 10) to M.H., RHU DELIVER ANR-21-RHUS-0001 (T. F. B.), Minor operating expenses were covered by Norvo Nordisk A/S.

AUTHOR CONTRIBUTIONS

T.F.B. initiated and coordinated the study. H.E.S., N.R., A.S., E.C., L.M., C.T, V.G.M., M.A.O., S.C., F.H.T.D., Z.N., N.A., C.P., L.H., S.C.D, M.H., A.L., F.D.Z. C.S., J.L., M.B.Z. and T.F.B. designed or performed experiments and analyzed data. A.S., D.H. and S.C.D. analyzed histopathology of mouse liver tissue. G.T. designed CLDN1 expression analyses and functional studies. Z.N., A.L., F.J. and I.D. performed or analyzed epigenetic experiments. S.M., T.O., T.R., M.V., C.D.V., E.D.G. and B.M.V performed CLDN1 expression analyses by IHC, IF or ISH in human or mouse liver tissue. Y.H. analyzed gene expression of the prognostic liver signature in part of the cell lines. F.J., H.E.S. and N.R. performed computational analyses, E.F. and P.P. prepared liver resections for *ex vivo* models. B.C.F., M.H. and A.T. co-designed animal experiments and edited the manuscript. A.C. and J.S. performed structural modeling of CLDN1 mAb binding to CLDN1. G.E., M.M., R.I., T.S. designed and conducted the experiments in non-human primates. G.T. helped generate figures. M.B.Z, C.S., J.L. and O.K. edited the manuscript. N.R., H.E.S., E.C., A.S. and T.F.B. designed the figures and wrote the manuscript.

COMPETING INTERESTS

Inserm, the University of Strasbourg, the Strasbourg University Hospitals and the Institut Hospitalo-Universitaire have filed patents and patent applications: US62/153,727 (Clinical gene signature-based human cell culture model and uses thereof; inventors T.F.B., Y.H.), US13/119,233 (Anti-Claudin-1 antibodies for the inhibition of hepatitis C virus infection; C. S., T. F. B.); US15/979,609 PCT/EP2016/055942 (Anti-Claudin-1 monoclonal antibodies for the prevention and treatment of HCC; T. F. B., M.B.Z); US16/086,934 PCT/EP2017/056703 (Humanized anti-Claudin 1 antibodies and uses thereof; T. F. B.) and PCT/EP2020/081941 (Anti-Claudin 1

monoclonal antibodies for the prevention and treatment of fibrotic disease; T. F. B., E. C., N. R., A. S., R. I., M. M., T. S.), which have all been licensed to Alentis Therapeutics, Basel. G. E., M. M., A. T., G. T., R. I, T. S., T. F. B, C. S, Y. H. own shares of Alentis. G. E., M. M., A. T., G. T., R. I are employees of Alentis, T. F. B. serves as a consultant for Alentis. T. S. was an employee of Alentis. B.M.V is an employee and minor stock holder of Novo Nordisk. B.C.F is an employee of Ferring Pharmaceuticals and serves on the Scientific Advisory Board of Mediar Therapeutics. Any potential conflict of interest is managed independently by the SATT Conectus and Inserm Transfert for the authors of the University of Strasbourg and Inserm.

DATA AND MATERIALS AVAILIBILITY

All data associated with this study are available in the main text or the supplementary materials. Raw data from figures are in data file S1. Transcriptomic data reported in this paper have been deposited at the Gene Expression Omnibus database (GEO) with accession numbers GSE174542, GSE174543, and GSE206581. FRG mice are available under a material transfer agreement with Yecuris. Recombinant HCV strains and Huh7.5 cell lines for infection studies are available under a material transfer agreement with Apath LLC.

SUPPLEMENTARY MATERIAL

- **Materials and Methods**
- **Figure S1-S19**
- **Table S1-S18**
- **Data File S1-S2**
- **References (51-91)**

REFERENCES and notes

1. D. C. Rockey, P. D. Bell, J. A. Hill, Fibrosis--a common pathway to organ injury and failure. *N Engl J Med* **372** (12), 1138-1149 (2015).

2. N. Roehlen, E. Crouchet, T. F. Baumert, Liver Fibrosis: Mechanistic Concepts and Therapeutic Perspectives. *Cells* **9** (4), 875 (2020).

3. L. Richeldi, F. Varone, M. Bergna, J. de Andrade, J. Falk, R. Hallowell, S. Jouneau, Y. Kondoh, L. Morrow, W. Randerath, M. Strek, G. Tabaj, Pharmacological management of progressive-fibrosing interstitial lung diseases: a review of the current evidence. *Eur Respir Rev* **27** (150), 180074 (2018).

4. M. Ruiz-Ortega, S. Rayego-Mateos, S. Lamas, A. Ortiz, R. R. Rodrigues-Diez, Targeting the progression of chronic kidney disease. *Nat Rev Nephrol* **16** (5), 269-288 (2020).

5. M. B. Zeisel, P. Dhawan, T. F. Baumert, Tight junction proteins in gastrointestinal and liver disease. *Gut* **68** (3), 547-561 (2019).

6. M. J. Evans, T. von Hahn, D. M. Tscherne, A. J. Syder, M. Panis, B. Wolk, T. Hatziioannou, J. A. McKeating, P. D. Bieniasz, C. M. Rice, Claudin-1 is a hepatitis C virus co-receptor required for a late step in entry. *Nature* **446** (7137), 801-805 (2007).

7. A. Holczbauer, B. Gyongyosi, G. Lotz, P. Torzsok, P. Kaposi-Novak, A. Szijarto, P. Tatrai, P. Kupcsulik, Z. Schaff, A. Kiss, Increased expression of claudin-1 and claudin-7 in liver cirrhosis and hepatocellular carcinoma. *Pathol Oncol Res* **20** (3), 493-502 (2014).

8. Y. Suh, C. H. Yoon, R. K. Kim, E. J. Lim, Y. S. Oh, S. G. Hwang, S. An, G. Yoon, M. C. Gye, J. M. Yi, M. J. Kim, S. J. Lee, Claudin-1 induces epithelial-mesenchymal transition through activation of the c-Abl-ERK signaling pathway in human liver cells. *Oncogene* **32** (41), 4873-4882 (2013).

9. I. Fofana, S. E. Krieger, F. Grunert, S. Glauben, F. Xiao, S. Fafi-Kremer, E. Soulier, C. Royer, C. Thumann, C. J. Mee, J. A. McKeating, T. Dragic, P. Pessaux, F. Stoll-Keller, C. Schuster, J. Thompson, T. F. Baumert, Monoclonal anti-claudin 1 antibodies prevent hepatitis C virus infection of primary human hepatocytes. *Gastroenterology* **139** (3), 953-964, 964 e951-954 (2010).

10. C. C. Colpitts, R. G. Tawar, L. Mailly, C. Thumann, L. Heydmann, S. C. Durand, F. Xiao, E. Robinet, P. Pessaux, M. B. Zeisel, T. F. Baumert, Humanisation of a claudin-1-specific monoclonal antibody for clinical prevention and cure of HCV infection without escape. *Gut* **67** (4), 736-745 (2018).

11. L. Mailly, F. Xiao, J. Lupberger, G. K. Wilson, P. Aubert, F. H. Duong, D. Calabrese, C. Leboeuf, I. Fofana, C. Thumann, S. Bandiera, M. Lutgehetmann, T. Volz, C. Davis, H. J. Harris, C. J. Mee, E. Girardi, B. Chane-Woon-Ming, M. Ericsson, N. Fletcher, R. Bartenschlager, P. Pessaux, K. Vercauteren, P. Meuleman, P. Villa, L. Kaderali, S. Pfeffer, M. H. Heim, M. Neunlist, M. B. Zeisel, M. Dandri, J. A. McKeating, E. Robinet, T. F. Baumert, Clearance of persistent hepatitis C virus infection in humanized mice using a claudin-1-targeting monoclonal antibody. *Nat Biotechnol* **33** (5), 549-554 (2015).

12. A. L. Rasmussen, N. Tchitchek, N. J. Susnow, A. L. Krasnoselsky, D. L. Diamond, M. M. Yeh, S. C. Proll, M. J. Korth, K. A. Walters, S. Lederer, A. M. Larson, R. L. Carithers, A. Benecke, M. G. Katze, Early transcriptional programming links progression to hepatitis C virus-induced severe liver disease in transplant patients. *Hepatology* **56** (1), 17-27 (2012).

13. W. Zhou, Y. Ma, J. Zhang, J. Hu, M. Zhang, Y. Wang, Y. Li, L. Wu, Y. Pan, Y. Zhang, X. Zhang, X. Zhang, Z. Zhang, J. Zhang, H. Li, L. Lu, L. Jin, J. Wang, Z. Yuan, J. Liu, Predictive model for inflammation grades of chronic hepatitis B: Large-scale analysis of clinical parameters and gene expressions. *Liver Int* **37** (11), 1632-1641 (2017).

14. C. A. Moylan, H. Pang, A. Dellinger, A. Suzuki, M. E. Garrett, C. D. Guy, S. K. Murphy, A. E. Ashley-Koch, S. S. Choi, G. A. Michelotti, D. D. Hampton, Y. Chen, H. L. Tillmann, M. A. Hauser, M. F. Abdelmalek, A. M. Diehl, Hepatic gene expression profiles differentiate presymptomatic patients with mild versus severe nonalcoholic fatty liver disease. *Hepatology* **59** (2), 471-482 (2014).

15. N. Aizarani, A. Saviano, Sagar, L. Mailly, S. Durand, J. S. Herman, P. Pessaux, T. F. Baumert, D. Grun, A human liver cell atlas reveals heterogeneity and epithelial progenitors. *Nature* **572** (7768), 199-204 (2019).

16. P. Ramachandran, R. Dobie, J. R. Wilson-Kanamori, E. F. Dora, B. E. P. Henderson, N. T. Luu, J. R. Portman, K. P. Matchett, M. Brice, J. A. Marwick, R. S. Taylor, M. Efremova, R. Vento-Tormo, N. O. Carragher, T. J. Kendall, J. A. Fallowfield, E. M. Harrison, D. J. Mole, S. J. Wigmore, P. N. Newsome, C. J. Weston, J. P. Iredale, F. Tacke, J. W. Pollard,

C. P. Ponting, J. C. Marioni, S. A. Teichmann, N. C. Henderson, Resolving the fibrotic niche of human liver cirrhosis at single-cell level. *Nature* **575** (7783), 512-518 (2019).

17. T. S. Andrews, J. Atif, J. C. Liu, C. T. Perciani, X. Z. Ma, C. Thoeni, M. Slyper, G. Eraslan, A. Segerstolpe, J. Manuel, S. Chung, E. Winter, I. Cirlan, N. Khuu, S. Fischer, O. Rozenblatt-Rosen, A. Regev, I. D. McGilvray, G. D. Bader, S. A. MacParland, Single-Cell, Single-Nucleus, and Spatial RNA Sequencing of the Human Liver Identifies Cholangiocyte and Mesenchymal Heterogeneity. *Hepatol Commun* **6** (4), 821-840 (2022).

18. Y. Li, J. Wang, K. Asahina, Mesothelial cells give rise to hepatic stellate cells and myofibroblasts via mesothelial-mesenchymal transition in liver injury. *Proc Natl Acad Sci U S A* **110** (6), 2324-2329 (2013).

19. M. B. Buechler, R. N. Pradhan, A. T. Krishnamurty, C. Cox, A. K. Calviello, A. W. Wang, Y. A. Yang, L. Tam, R. Caothien, M. Roose-Girma, Z. Modrusan, J. R. Arron, R. Bourgon, S. Muller, S. J. Turley, Cross-tissue organization of the fibroblast lineage. *Nature* **593** (7860), 575-579 (2021).

20. S. Ko, J. O. Russell, L. M. Molina, S. P. Monga, Liver Progenitors and Adult Cell Plasticity in Hepatic Injury and Repair: Knowns and Unknowns. *Annu Rev Pathol* **15**, 23-50 (2020).

21. H. Azuma, N. Paulk, A. Ranade, C. Dorrell, M. Al-Dhalimy, E. Ellis, S. Strom, M. A. Kay, M. Finegold, M. Grompe, Robust expansion of human hepatocytes in Fah-/-/Rag2-/-/Il2rg-/- mice. *Nat Biotechnol* **25** (8), 903-910 (2007).

22. N. Kishida, S. Matsuda, O. Itano, M. Shinoda, M. Kitago, H. Yagi, Y. Abe, T. Hibi, Y. Masugi, K. Aiura, M. Sakamoto, Y. Kitagawa, Development of a novel mouse model of hepatocellular carcinoma with nonalcoholic steatohepatitis using a high-fat, choline-deficient diet and intraperitoneal injection of diethylnitrosamine. *BMC Gastroenterol* **16** (1), 61 (2016).

23. A. J. Debacker, J. Voutila, M. Catley, D. Blakey, N. Habib, Delivery of Oligonucleotides to the Liver with GalNAc: From Research to Registered Therapeutic Drug. *Mol Ther* **28** (8), 1759-1771 (2020).

24. C. Baeck, A. Wehr, K. R. Karlmark, F. Heymann, M. Vucur, N. Gassler, S. Huss, S. Klussmann, D. Eulberg, T. Luedde, C. Trautwein, F. Tacke, Pharmacological inhibition of the chemokine CCL2 (MCP-1) diminishes liver macrophage infiltration and steatohepatitis in chronic hepatic injury. *Gut* **61** (3), 416-426 (2012).

25. E. Crouchet, S. Bandiera, N. Fujiwara, S. Li, H. El Saghire, M. Fernandez-Vaquero, T. Riedl, X. Sun, H. Hirschfield, F. Juhling, S. Zhu, N. Roehlen, C. Ponsolles, L. Heydmann, A. Saviano, T. Qian, A. Venkatesh, J. Lupberger, E. R. Verrier, M. Sojoodi, M. A. Oudot, F. H. T. Duong, R. Masia, L. Wei, C. Thumann, S. C. Durand, V. Gonzalez-Motos, D. Heide, J. Hetzer, S. Nakagawa, A. Ono, W. M. Song, T. Higashi, R. Sanchez, R. S. Kim, C. B. Bian, K. Kiani, T. Croonenborghs, A. Subramanian, R. T. Chung, B. K. Straub, D. Schuppan, M. Ankavay, L. Cocquerel, E. Schaeffer, N. Goossens, A. P. Koh, M. Mahajan, V. D. Nair, G. Gunasekaran, M. E. Schwartz, N. Bardeesy, A. K. Shalek, O. Rozenblatt-Rosen, A. Regev, E. Felli, P. Pessaux, K. K. Tanabe, M. Heikenwalder, C. Schuster, N.

Pochet, M. B. Zeisel, B. C. Fuchs, Y. Hoshida, T. F. Baumert, A human liver cell-based system modeling a clinical prognostic liver signature for therapeutic discovery. *Nat Commun* **12** (1), 5525 (2021).

26. D. E. Kleiner, E. M. Brunt, M. Van Natta, C. Behling, M. J. Contos, O. W. Cummings, L. D. Ferrell, Y. C. Liu, M. S. Torbenson, A. Unalp-Arida, M. Yeh, A. J. McCullough, A. J. Sanyal, Design and validation of a histological scoring system for nonalcoholic fatty liver disease. *Hepatology* **41** (6), 1313-1321 (2005).

27. V. Mariotti, M. Strazzabosco, L. Fabris, D. F. Calvisi, Animal models of biliary injury and altered bile acid metabolism. *Biochim Biophys Acta Mol Basis Dis* **1864** (4 Pt B), 1254-1261 (2018).

28. D. Carter, S. Presnell, B. David, A. Chen, Modeling NAFLD using 3D bioprinted human liver tissue. *J Hepatol* **68** (S1), S357-S358 (2018).

29. D. Antoni, H. Burckel, E. Josset, G. Noel, Three-dimensional cell culture: a breakthrough in vivo. *Int J Mol Sci* **16** (3), 5517-5527 (2015).

30. S. A. Harrison, M. R. Bashir, C. D. Guy, R. Zhou, C. A. Moylan, J. P. Frias, N. Alkhouri, M. B. Bansal, S. Baum, B. A. Neuschwander-Tetri, R. Taub, S. E. Moussa, Resmetirom (MGL-3196) for the treatment of non-alcoholic steatohepatitis: a multicentre, randomised, double-blind, placebo-controlled, phase 2 trial. *Lancet* **394** (10213), 2012-2024 (2019).

31. S. Nakagawa, L. Wei, W. M. Song, T. Higashi, S. Ghoshal, R. S. Kim, C. B. Bian, S. Yamada, X. Sun, A. Venkatesh, N. Goossens, G. Bain, G. Y. Lauwers, A. P. Koh, M. El-Abtah, N. B. Ahmad, H. Hoshida, D. J. Erstad, G. Gunasekaran, Y. Lee, M. L. Yu, W. L. Chuang, C. Y. Dai, M. Kobayashi, H. Kumada, T. Beppu, H. Baba, M. Mahajan, V. D. Nair, M. Lanuti, A. Villanueva, A. Sangiovanni, M. Iavarone, M. Colombo, J. M. Llovet, A. Subramanian, A. M. Tager, S. L. Friedman, T. F. Baumert, M. E. Schwarz, R. T. Chung, K. K. Tanabe, B. Zhang, B. C. Fuchs, Y. Hoshida, Molecular Liver Cancer Prevention in Cirrhosis by Organ Transcriptome Analysis and Lysophosphatidic Acid Pathway Inhibition. *Cancer Cell* **30** (6), 879-890 (2016).

32. I. Jang, K. A. Beningo, Integrins, CAFs and Mechanical Forces in the Progression of Cancer. *Cancers (Basel)* **11** (5), 721 (2019).

33. S. Wullschleger, R. Loewith, M. N. Hall, TOR signaling in growth and metabolism. *Cell* **124** (3), 471-484 (2006).

34. J. F. Creeden, Z. A. Kipp, M. Xu, R. M. Flight, H. N. B. Moseley, G. J. Martinez, W. H. Lee, K. Alganem, A. S. Imami, M. R. McMullen, S. Roychowdhury, A. M. Nawabi, J. A. Hipp, S. Softic, S. A. Weinman, R. McCullumsmith, L. E. Nagy, T. D. Hinds, Jr., Hepatic kinome atlas: An in-depth identification of kinase pathways in liver fibrosis of humans and rodents. *Hepatology*, (2022).

35. K. Sato, M. Marzioni, F. Meng, H. Francis, S. Glaser, G. Alpini, Ductular Reaction in Liver Diseases: Pathological Mechanisms and Translational Significances. *Hepatology* **69** (1), 420-430 (2019).

36. L. Broutier, A. Andersson-Rolf, C. J. Hindley, S. F. Boj, H. Clevers, B. K. Koo, M. Huch, Culture and establishment of self-renewing human and mouse adult liver and pancreas 3D organoids and their genetic manipulation. *Nat Protoc* **11** (9), 1724-1743 (2016).

37. K. Hasegawa, S. Wakino, P. Simic, Y. Sakamaki, H. Minakuchi, K. Fujimura, K. Hosoya, M. Komatsu, Y. Kaneko, T. Kanda, E. Kubota, H. Tokuyama, K. Hayashi, L. Guarente, H. Itoh, Renal tubular Sirt1 attenuates diabetic albuminuria by epigenetically suppressing Claudin-1 overexpression in podocytes. *Nat Med* **19** (11), 1496-1504 (2013).

38. S. Lovisa, V. S. LeBleu, B. Tampe, H. Sugimoto, K. Vadnagara, J. L. Carstens, C. C. Wu, Y. Hagos, B. C. Burckhardt, T. Pentcheva-Hoang, H. Nischal, J. P. Allison, M. Zeisberg, R. Kalluri, Epithelial-to-mesenchymal transition induces cell cycle arrest and parenchymal damage in renal fibrosis. *Nat Med* **21** (9), 998-1009 (2015).

39. A. Pardo, K. Gibson, J. Cisneros, T. J. Richards, Y. Yang, C. Becerril, S. Yousem, I. Herrera, V. Ruiz, M. Selman, N. Kaminski, Up-regulation and profibrotic role of osteopontin in human idiopathic pulmonary fibrosis. *PLoS Med* **2** (9), e251 (2005).

40. R. L. Chevalier, M. S. Forbes, B. A. Thornhill, Ureteral obstruction as a model of renal interstitial fibrosis and obstructive nephropathy. *Kidney Int* **75** (11), 1145-1152 (2009).

41. A. C. Habermann, A. J. Gutierrez, L. T. Bui, S. L. Yahn, N. I. Winters, C. L. Calvi, L. Peter, M. I. Chung, C. J. Taylor, C. Jetter, L. Raju, J. Roberson, G. Ding, L. Wood, J. M. S. Sucre, B. W. Richmond, A. P. Serezani, W. J. McDonnell, S. B. Mallal, M. J. Bacchetta, J. E. Loyd, C. M. Shaver, L. B. Ware, R. Bremner, R. Walia, T. S. Blackwell, N. E. Banovich, J. A. Kropski, Single-cell RNA sequencing reveals profibrotic roles of distinct epithelial and mesenchymal lineages in pulmonary fibrosis. *Sci Adv* **6** (28), eaba1972 (2020).

42. A. Mullard, FDA rejects NASH drug. *Nat Rev Drug Discov* **19** (8), 501 (2020).

43. P. N. Newsome, K. Buchholtz, K. Cusi, M. Linder, T. Okanoue, V. Ratziu, A. J. Sanyal, A. S. Sejling, S. A. Harrison, N. N. Investigators, A Placebo-Controlled Trial of Subcutaneous Semaglutide in Nonalcoholic Steatohepatitis. *N Engl J Med* **384** (12), 1113-1124 (2021).

44. V. W. Wong, L. A. Adams, V. de Ledinghen, G. L. Wong, S. Sookoian, Noninvasive biomarkers in NAFLD and NASH - current progress and future promise. *Nat Rev Gastroenterol Hepatol* **15** (8), 461-478 (2018).

45. S. Robert, T. Gicquel, T. Victoni, S. Valenca, E. Barreto, B. Bailly-Maitre, E. Boichot, V. Lagente, Involvement of matrix metalloproteinases (MMPs) and inflammasome pathway in molecular mechanisms of fibrosis. *Biosci Rep* **36** (4), e00360 (2016).

46. J. Lv, B. Sun, Z. Mai, M. Jiang, J. Du, CLDN-1 promoted the epithelial to migration and mesenchymal transition (EMT) in human bronchial epithelial cells via Notch pathway. *Mol Cell Biochem* **432** (1-2), 91-98 (2017).

47. J. Dumas, M. A. Gargano, G. M. Dancik, shinyGEO: a web-based application for analyzing gene expression omnibus datasets. *Bioinformatics* **32** (23), 3679-3681 (2016).

48. N. Hamdane, F. Juhling, E. Crouchet, H. El Saghire, C. Thumann, M. A. Oudot, S. Bandiera, A. Saviano, C. Ponsolles, A. A. Roca Suarez, S. Li, N. Fujiwara, A. Ono, I. Davidson, N. Bardeesy, C. Schmidl, C. Bock, C. Schuster, J. Lupberger, F. Habersetzer, M. Doffoel, T. Piardi, D. Sommacale, M. Imamura, T. Uchida, H. Ohdan, H. Aikata, K. Chayama, T. Boldanova, P. Pessaux, B. C. Fuchs, Y. Hoshida, M. B. Zeisel, F. H. T. Duong, T. F. Baumert, HCV-Induced Epigenetic Changes Associated With Liver Cancer Risk Persist After Sustained Virologic Response. *Gastroenterology* **156** (8), 2313-2329 e2317 (2019).

49. A. Liberzon, C. Birger, H. Thorvaldsdottir, M. Ghandi, J. P. Mesirov, P. Tamayo, The Molecular Signatures Database (MSigDB) hallmark gene set collection. *Cell Syst* **1** (6), 417-425 (2015).

50. K. Street, D. Risso, R. B. Fletcher, D. Das, J. Ngai, N. Yosef, E. Purdom, S. Dudoit, Slingshot: cell lineage and pseudotime inference for single-cell transcriptomics. *BMC Genomics* **19** (1), 477 (2018).

834 51. M. Ryaboshapkina, M. Hammar, Human hepatic gene expression signature of non-
835 alcoholic fatty liver disease progression, a meta-analysis. *Sci Rep* **7** (1), 12361 (2017).

836 52. R. H. Hubner, W. Gitter, N. E. El Mokhtari, M. Mathiak, M. Both, H. Bolte, S. Freitag-
837 Wolf, B. Bewig, Standardized quantification of pulmonary fibrosis in histological samples.
838 *Biotechniques* **44** (4), 507-511, 514-507 (2008).
839 53. M. Boeckh, M. M. Berrey, R. A. Bowden, S. W. Crawford, J. Balsley, L. Corey, Phase 1
840 evaluation of the respiratory syncytial virus-specific monoclonal antibody palivizumab in
841 recipients of hematopoietic stem cell transplants. *J. Infect. Dis.* **184** (3), 350-354 (2001).

842 54. P. Bankhead, M. B. Loughrey, J. A. Fernandez, Y. Dombrowski, D. G. McArt, P. D.
843 Dunne, S. McQuaid, R. T. Gray, L. J. Murray, H. G. Coleman, J. A. James, M. Salto-Tellez,
844 P. W. Hamilton, QuPath: Open source software for digital pathology image analysis. *Sci*
845 *Rep* **7** (1), 16878 (2017).

846 55. H. M. Berman, J. Westbrook, Z. Feng, G. Gilliland, T. N. Bhat, H. Weissig, I. N.
847 Shindyalov, P. E. Bourne, The Protein Data Bank. *Nucleic Acids Res* **28** (1), 235-242
848 (2000).

849 56. M. P. Jacobson, D. L. Pincus, C. S. Rapp, T. J. Day, B. Honig, D. E. Shaw, R. A. Friesner,
850 A hierarchical approach to all-atom protein loop prediction. *Proteins* **55** (2), 351-367
851 (2004).

852 57. M. P. Jacobson, R. A. Friesner, Z. Xiang, B. Honig, On the role of the crystal environment
853 in determining protein side-chain conformations. *J Mol Biol* **320** (3), 597-608 (2002).

854 58. K. Zhu, T. Day, D. Warshaviak, C. Murrett, R. Friesner, D. Pearlman, Antibody structure
855 determination using a combination of homology modeling, energy-based refinement, and
856 loop prediction. *Proteins* **82** (8), 1646-1655 (2014).

857 59. N. K. Salam, M. Adzhigirey, W. Sherman, D. A. Pearlman, Structure-based approach to
858 the prediction of disulfide bonds in proteins. *Protein Eng Des Sel* **27** (10), 365-374 (2014).

859 60. H. Beard, A. Cholleti, D. Pearlman, W. Sherman, K. A. Loving, Applying physics-based
860 scoring to calculate free energies of binding for single amino acid mutations in protein-
861 protein complexes. *PLoS One* **8** (12), e82849 (2013).

862 61. M. A. Lomize, I. D. Pogozheva, H. Joo, H. I. Mosberg, A. L. Lomize, OPM database and
863 PPM web server: resources for positioning of proteins in membranes. *Nucleic Acids Res*
864 **40** (Database issue), D370-376 (2012).

865 62. W. L. Jorgensen, J. Chandrasekhar, J. D. Madura, R. W. Impey, L. M. Klein, Comparison
866 of simple potential functions for simulating liquid water. *J Chem Phys* **79**, 926-935 (1983).

867 63. K. Roos, C. Wu, W. Damm, M. Reboul, J. M. Stevenson, C. Lu, M. K. Dahlgren, S.
868 Mondal, W. Chen, L. Wang, R. Abel, R. A. Friesner, E. D. Harder, OPLS3e: Extending
869 Force Field Coverage for Drug-Like Small Molecules. *Journal of Chemical Theory and*
870 *Computation* **15** (3), 1863-1874 (2019).

64. G. Martyna, D. Tobias, M. Klein, Constant pressure molecular dynamics algorithms. *The Journal of Chemical Physics* **101** (5), 4177-4189 (1994).

65. G. J. Martyna, M. L. Klein, M. Tuckerman, Nosé–Hoover chains: The canonical ensemble via continuous dynamics. *The Journal of Chemical Physics* **97** (4), 2635-2643 (1992).

66. K. J. Bowers, E. Chow, H. Xu, R. O. Dror, M. P. Eastwood, B. A. Gregersen, J. L. Klepeis, I. Kolossvary, M. A. Moraes, F. D. Sacerdoti, J. K. Salmon, Y. Shan, D. E. Shaw, paper presented at the Proceedings of the 2006 ACM/IEEE conference on Supercomputing, Tampa, Florida, 2006.

67. T. Tubiana, J. C. Carvaillo, Y. Boulard, S. Bressanelli, TTClust: A Versatile Molecular Simulation Trajectory Clustering Program with Graphical Summaries. *J Chem Inf Model* **58** (11), 2178-2182 (2018).

68. R. Tibshirani, G. Walther, T. Hastie, Estimating the number of clusters in a data set via the gap statistic. *J R Stat Soc Series B Stat Methodol.* **63** (2), 411-423 (2001).

69. G. C. P. van Zundert, J. Rodrigues, M. Trellet, C. Schmitz, P. L. Kastritis, E. Karaca, A. S. J. Melquiond, M. van Dijk, S. J. de Vries, A. Bonvin, The HADDOCK2.2 Web Server: User-Friendly Integrative Modeling of Biomolecular Complexes. *J Mol Biol* **428** (4), 720-725 (2016).

70. C. Dominguez, R. Boelens, A. M. Bonvin, HADDOCK: a protein-protein docking approach based on biochemical or biophysical information. *J Am Chem Soc* **125** (7), 1731-1737 (2003).

71. F. Ambrosetti, S. Jandova, A. M. Bonvin, A protocol for information-driven antibody-antigen modelling with the HADDOCK2.4 webserver. *arXiv***:2005.03283**, (2020).

72. A. Vangone, A. M. Bonvin, Contacts-based prediction of binding affinity in protein-protein complexes. *Elife* **4**, e07454 (2015).

73. J. Freeth, J. Soden, New Advances in Cell Microarray Technology to Expand Applications in Target Deconvolution and Off-Target Screening. *SLAS Discov* **25** (2), 223-230 (2020).

74. M. Charni-Natan, I. Goldstein, Protocol for Primary Mouse Hepatocyte Isolation. *STAR Protoc* **1** (2), 100086 (2020).

75. V. Kegel, D. Deharde, E. Pfeiffer, K. Zeilinger, D. Seehofer, G. Damm, Protocol for Isolation of Primary Human Hepatocytes and Corresponding Major Populations of Non-parenchymal Liver Cells. *J Vis Exp* (109), e53069 (2016).

76. L. Aoudjehane, G. Bisch, O. Scatton, C. Granier, J. Gaston, C. Housset, P. Roingeard, F. L. Cosset, F. Perdigao, P. Balladur, T. Wakita, Y. Calmus, F. Conti, Infection of Human Liver Myofibroblasts by Hepatitis C Virus: A Direct Mechanism of Liver Fibrosis in Hepatitis C. *PLoS One* **10** (7), e0134141 (2015).

77. L. Mailly, F. Xiao, J. Lupberger, G. K. Wilson, P. Aubert, F. H. T. Duong, D. Calabrese, C. Leboeuf, I. Fofana, C. Thumann, S. Bandiera, M. Lutgehetmann, T. Volz, C. Davis, H. J. Harris, C. J. Mee, E. Girardi, B. Chane-Woon-Ming, M. Ericsson, N. Fletcher, R. Bartenschlager, P. Pessaux, K. Vercauteren, P. Meuleman, P. Villa, L. Kaderali, S. Pfeffer, M. H. Heim, M. Neunlist, M. B. Zeisel, M. Dandri, J. A. McKeating, E. Robinet, T. F. Baumert, Clearance of persistent hepatitis C virus infection in humanized mice using a claudin-1-targeting monoclonal antibody. *Nat Biotechnol* **33** (5), 549-554 (2015).

78. C. A. Schneider, W. S. Rasband, K. W. Eliceiri, NIH Image to ImageJ: 25 years of image analysis. *Nat. Methods* **9** (7), 671-675 (2012).

79. S. Fafi-Kremer, I. Fofana, E. Soulier, P. Carolla, P. Meuleman, G. Leroux-Roels, A. H. Patel, F. L. Cosset, P. Pessaux, M. Doffoel, P. Wolf, F. Stoll-Keller, T. F. Baumert, Viral entry and escape from antibody-mediated neutralization influence hepatitis C virus reinfection in liver transplantation. *J Exp Med* **207** (9), 2019-2031 (2010).

80. L. Y. King, C. Canasto-Chibuque, K. B. Johnson, S. Yip, X. Chen, K. Kojima, M. Deshmukh, A. Venkatesh, P. S. Tan, X. Sun, A. Villanueva, A. Sangiovanni, V. Nair, M. Mahajan, M. Kobayashi, H. Kumada, M. Iavarone, M. Colombo, M. I. Fiel, S. L. Friedman, J. M. Llovet, R. T. Chung, Y. Hoshida, A genomic and clinical prognostic index for hepatitis C-related early-stage cirrhosis that predicts clinical deterioration. *Gut* **64** (8), 1296-1302 (2015).

81. A. Subramanian, P. Tamayo, V. K. Mootha, S. Mukherjee, B. L. Ebert, M. A. Gillette, A. Paulovich, S. L. Pomeroy, T. R. Golub, E. S. Lander, J. P. Mesirov, Gene set enrichment analysis: a knowledge-based approach for interpreting genome-wide expression profiles. *Proc Natl Acad Sci U S A* **102** (43), 15545-15550 (2005).

82. M. Nakatsukasa, S. Kawasaki, K. Yamasaki, H. Fukuoka, A. Matsuda, M. Tsujikawa, H. Tanioka, M. Nagata-Takaoka, J. Hamuro, S. Kinoshita, Tumor-associated calcium signal transducer 2 is required for the proper subcellular localization of claudin 1 and 7: implications in the pathogenesis of gelatinous drop-like corneal dystrophy. *Am J Pathol* **177** (3), 1344-1355 (2010).

83. K. J. Livak, T. D. Schmittgen, Analysis of relative gene expression data using real-time quantitative PCR and the 2(-Delta Delta C(T)) Method. *Methods* **25** (4), 402-408 (2001).

84. J. Lupberger, T. Croonenborghs, A. A. Roca Suarez, N. Van Renne, F. Juhling, M. A. Oudot, A. Virzi, S. Bandiera, C. Jamey, G. Meszaros, D. Brumaru, A. Mukherji, S. C. Durand, L. Heydmann, E. R. Verrier, H. El Saghire, N. Hamdane, R. Bartenschlager, S. Fereshetian, E. Ramberger, R. Sinha, M. Nabian, C. Everaert, M. Jovanovic, P. Mertins, S. A. Carr, K. Chayama, N. Dali-Youcef, R. Ricci, N. M. Bardeesy, N. Fujiwara, O. Gevaert, M. B. Zeisel, Y. Hoshida, N. Pochet, T. F. Baumert, Combined Analysis of Metabolomes, Proteomes, and Transcriptomes of Hepatitis C Virus-Infected Cells and Liver to Identify Pathways Associated With Disease Development. *Gastroenterology* **157** (2), 537-551 e539 (2019).

945 85. O. Bauhofer, A. Ruggieri, B. Schmid, P. Schirmacher, R. Bartenschlager, Persistence of
946 HCV in quiescent hepatic cells under conditions of an interferon-induced antiviral
947 response. *Gastroenterology* **143** (2), 429-438 e428 (2012).

948 86. S. Bandiera, S. Pernot, H. El Saghire, S. C. Durand, C. Thumann, E. Crouchet, T. Ye, I.
949 Fofana, M. A. Oudot, J. Barths, C. Schuster, P. Pessaux, M. H. Heim, T. F. Baumert, M.
950 B. Zeisel, Hepatitis C Virus-Induced Upregulation of MicroRNA miR-146a-5p in
951 Hepatocytes Promotes Viral Infection and Deregulates Metabolic Pathways Associated
952 with Liver Disease Pathogenesis. *J Virol* **90** (14), 6387-6400 (2016).

953 87. E. R. Verrier, C. C. Colpitts, C. Bach, L. Heydmann, A. Weiss, M. Renaud, S. C. Durand,
954 F. Habersetzer, D. Durantel, G. Abou-Jaoude, M. M. Lopez Ledesma, D. J. Felmlee, M.
955 Soumillon, T. Croonenborghs, N. Pochet, M. Nassal, C. Schuster, L. Brino, C. Sureau, M.
956 B. Zeisel, T. F. Baumert, A targeted functional RNA interference screen uncovers glypican
957 5 as an entry factor for hepatitis B and D viruses. *Hepatology* **63** (1), 35-48 (2016).

958 88. V. J. Barbero-Becerra, P. J. Giraudi, N. C. Chavez-Tapia, M. Uribe, C. Tiribelli, N. Rosso,
959 The interplay between hepatic stellate cells and hepatocytes in an in vitro model of NASH.
960 *Toxicol In Vitro* **29** (7), 1753-1758 (2015).

961 89. R. Hilhorst, L. Houkes, M. Mommersteeg, J. Musch, A. van den Berg, R. Ruijtenbeek,
962 Peptide microarrays for profiling of serine/threonine kinase activity of recombinant kinases
963 and lysates of cells and tissue samples. *Methods Mol Biol* **977**, 259-271 (2013).

90. A. Roy, A. Tolone, R. Hilhorst, J. Groten, T. Tomar, F. Paquet-Durand, Kinase activity profiling identifies putative downstream targets of cGMP/PKG signaling in inherited retinal neurodegeneration. *Cell Death Discov* **8** (1), 93 (2022).

91. K. Muller, H. Honcharova-Biletska, C. Koppe, M. Egger, L. K. Chan, A. T. Schneider, L. Kusgens, F. Bohm, Y. Boege, M. E. Healy, J. Schmitt, S. Comtesse, M. Castoldi, C. Preisinger, M. Szydlowska, E. Focaccia, N. T. Gaisa, S. H. Loosen, S. Jors, F. Tacke, C. Roderburg, V. Keitel, J. G. Bode, P. Boor, R. J. Davis, T. Longerich, F. Geisler, M. Heikenwalder, A. Weber, M. Vucur, T. Luedde, JNK signaling prevents biliary cyst formation through a CASPASE-8-dependent function of RIPK1 during aging. *Proc Natl Acad Sci U S A* **118** (12), e2007194118 (2021).

92. H. Wickham, *ggplot2: Elegant Graphics for Data Analysis*. Springer-Verlag New York (2016).

93. Y. Hao, S. Hao, E. Andersen-Nissen, W. M. Mauck, 3rd, S. Zheng, A. Butler, M. J. Lee, A. J. Wilk, C. Darby, M. Zager, P. Hoffman, M. Stoeckius, E. Papalexi, E. P. Mimitou, J. Jain, A. Srivastava, T. Stuart, L. M. Fleming, B. Yeung, A. J. Rogers, J. M. McElrath, C. A. Blish, R. Gottardo, P. Smibert, R. Satija, Integrated analysis of multimodal single-cell data. *Cell* **184** (13), 3573-3587 e3529 (2021).

FIGURE LEGENDS

Figure 1. CLDN1 expression is upregulated in chronic liver disease. A. *CLDN1* upregulation in liver tissues of patients with chronic HCV, HBV infection, or NASH. **B.** *CLDN1* expression in livers of patients with NASH with mild (F0-1) or advanced fibrosis (F3-4) and liver tissues of transplanted HCV-infected patients with stable or progressive fibrotic disease. **C**. *CLDN1* expression in healthy liver at the single-nucleus level. ($p<0.0001$, U-test). **D.** *CLDN1* expression along the cholangiocyte-bipotent progenitor cells-hepatocyte pseudotime trajectory by Slingshot in a combined scRNA-seq and snRNA-seq dataset(*50*). **E.** *CLDN1* expression at the single-cell level in human cirrhotic and healthy liver cells. Differential expression analysis identified *CLDN1* as a marker of mesothelial cells, hepatocytes and cholangiocytes ($p<0.0001$, U-test, respectively). **F.** Enhanced CLDN1 expression in hepatocytes at the stromal-epithelial interface of HCV cirrhotic nodule. Scale bars=1 mm. **G.** RNA ISH showing *CLDN1* expression in a subpopulation of *COL3A1*$^+$ stellate cells in NASH-associated liver cirrhosis. Scale bars=50μm (low resolution) and 20μm (high resolution image). **H.** Staining of CLDN1 with αSMA by immunofluorescence and CK19 and EPCAM by immunohistochemistry showing CLDN1 expression in cholangiocytes, EPCAM$^+$ bile duct cells and stellate cells. Scale bars=50μm. **I.** Upper panel: Computationally predicted structural model of the non-junctional CLDN1/CLDN1 mAb complex. Lower panel: Absent accessibility of the epitope targeted by the CLDN1 mAb in tight junctions. **J.** Expression of total CLDN1 and njCLDN1 in mild (F0-2, n=8) or advanced liver fibrosis (F3-4, n=10) using an antibody targeting the C-terminal domain of CLDN1 (total CLDN1) or mAb ALE.F02 targeting njCLDN1. **K.** Co-staining of CLDN1 and EPCAM in ductular reactions. Scale bars=65μm (F2) and 100μm (F4). **L.** Regulation of njCLDN1 expression by TNF-

α. HLMFs and primary human hepatocytes (PHHs) were treated with TNF-α, IKK-16 or TNF-α + IKK16 and CLDN1 expression analyzed by flow cytometry using anti-CLDN1 mAb H3L3 (*n*=3 independent experiments with 2-4 replicates per condition). ΔMFI is shown as fold change compared to untreated cells. **M.** The *CLDN1* locus with the indicated CUT&Tag and ChIP-seq tracks. Red boxes identify p65-bound sites that coincide with Encode-defined cis-Regulatory Elements (cCREs) both upstream and downstream of *CLDN1* with the density of previously identified ChIP-seq RELA binding sites (peak regions) as listed in ReMAP2022. ****p<0.0001, ***p<0.001, **p<0.01, *p<0.05 U-test (**A-B, J**), U-test with Bonferroni correction (C, E), and Student's t-test (**L**). MFI=Mean fluorescence intensity; MP=mononuclear phagocyte.

Figure 2. Targeting CLDN1 by siRNA or mAbs reduces liver fibrosis in a patient-derived mouse model. A-C *CLDN1* knockdown by GalNAc-siRNA reduces liver fibrosis in humanized liver fibrosis mouse model. **A.** Illustration of the experimental approach. **B.** CLDN1 expression, fibrosis assessment in humanized areas, and tumor nodule count according to the treatment group (siCTRL *n*=6, siCLDN1 *n*=5). **C.** Representative images of human CLDN1 staining, Sirius red, fibronectin-1 (FN1) immunostaining and macroscopy of GalNAc siCLDN1 and siCTRL mice. Scale bar=50µm, 250µm, 50µm respectively. **D-H.** CLDN1 mAb treatment reduced liver fibrosis and HCC. **D.** Study protocol of humanized mouse NASH model treated with CLDN1 mAb. **E-F.** Fibrosis assessment in the total liver tissue and humanized areas, and tumor nodule count of experiment 1 (**E,** Control *n*=3, CLDN1 mAb *n*=4), and experiment 2 (**F**, Control *n*=10, CLDN1 mAb *n*=10) which were performed independently. Sample size in FN1 experiment 2 (Control *n*=8, CLDN1 mAb *n*=7). Control group was treated with i.p. injections of vehicle. **G**. Representative images of FAH, Sirius red, FN1 staining and macroscopic images according to treatment groups (experiment 1). Scale bars=250µm, 250µm, 50µm, respectively. **H.** Gene expression of fibrosis markers *Col1a1* and *Timp1* (experiment 1). Bars show mean ±SEM. *p<0.05, **p<0.01, U-test (**B, E, F**), t-test (**H**), respectively. FAH=fumarylacetoacetate hydrolase; hCLDN1= human CLDN1.

Figure 3. Targeting non-junctional CLDN1 reduces fibrosis and tumor development in mouse models for liver and biliary fibrosis. A. Study protocol of DEN-CDA-HFD NASH fibrosis mouse model and mAb treatment. **B.** Representative images of Sirius Red and fibronectin-1 (FN1) staining in mouse livers. Scale bars=250µm and 50µm, respectively. **C.** Collagen proportional area (CPA) (Control *n*=18, CLDN1 mAb *n*=20) and FN1 quantification (Control *n*=15, CLDN1 mAb *n*=16) in representative areas according to the treatment group. **D.** Gene expression of fibrosis markers *Col1a1* (Control *n*=5, CLDN1 mAb *n*=5) and *Acta2* (Control *n*=4, CLDN1 mAb *n*=5). **E.** Liver fat proportional area and NAFLD activity score according to the assigned treatment (Control *n*=18, CLDN1 mAb *n*=20). **F.** Quantification of liver immunostaining of $CD3^+$ T cells, and $CD68^+$ macrophages (Control *n*=15, CLDN1 mAb *n*=16). **G.** Representative images of macroscopy and $HSP70^+$ areas in mouse livers. Scale bars=500µm. **H.** Macroscopic (left panel) and histological (right panel) assessment of tumor occurrence in mouse livers (Control *n*=18, CLDN1 mAb *n*=20). **I.** Number and size of tumor nodules and proportion of $HSP70^+$ tumors in mice livers (Control *n*=18, CLDN1 mAb *n*=20). **J.** Study protocol of DDC mouse model for biliary fibrosis. K. Sirius red and FN1 staining in CLDN1 mAb- or Control-treated DDC mice. Representative images are shown. **L.** Quantification of CPA and FN1-positive area in all mice. **M.** Ishak score in CLDN1 mAb- or control-treated DDC mice. All control groups were treated with i.p. injections of vehicle. ****p<0.0001, t-test. Bars show mean ±SEM. *p<0.05, **p<0.01, ***p<0.001, ****p<0.0001, U-test, respectively. H&E=Haemotoxylin and Eosin; HSP70=Heat-shock protein 70; SEM=standard error of the mean.

Figure 4. CLDN1-specific mAb effects in patient-derived *ex vivo* models of chronic liver disease. A. Illustration of Organovo ExVive fibrosis model. **B.** Images of Trichromic Masson and H&E staining in Organovo ExVive tissues sections treated with CLDN1 mAb or control mAb (*n*=4 biological and *N*=8 technical replicates per condition). Macrovascular steatosis is indicated by green and microvascular steatosis by red arrows. Scale bars=40µm. **C.** Quantification of collagen proportional area in Organovo ExVive tissue. **D.** Illustration of patient-derived liver spheroids. **E.** Immunostaining of ASPGR1, CD31, CD68 and α-SMA in patient-derived liver spheroids. Staining with anti-mouse secondary antibodies were used as a control. Spheroids were visualized by Celigo imaging cytometer. Scale bar=500µm. **F.** Gene expression of *COL1A1*, *CTGF* (*n*=3 independent experiments with *n*=4 biological replicates per condition) in liver spheroids exposed to a TGF-β, FFA and LPS and treated with either CLDN1 mAb or control mAb. **G.** Total collagen deposition in patient-derived liver spheroids stimulated with FFA, LPS, and TGF-β and treated with CLDN1 mAb, control mAb or resmetirom (*n*=8 different donors with 1-3 replicates per condition). **H.** Modulation of PLS to good (green) or poor (orange) prognosis status (*51*) in precision cut liver slices. Significance (FDR, Kolmogorov-Smirnov test) of induction (red) or suppression (blue) of PLS poor- or good-prognosis genes is shown. Bars show mean ±SEM. *p<0.05, ****p<0.0001, t-test (**C**), U-test (**F, G**). ECs=Endothelial cells; H&E=Haemotoxylin and Eosin; HCs=Hepatocytes; HSCs=Hepatic stellate cells; KCs=Kupffer cells; SEM=standard error of the mean.

Figure 5. Treatment with CLDN1-specific mAb suppresses liver cell circuits mediating inflammation, fibrosis, and carcinogenesis. A. Graphical illustration of methodological approach to assess liver fibrosis associated cell plasticity in bulk RNA-seq data derived from two fibrosis mouse models. **B.** Modulation of gene sets characterizing mature hepatocytes and immature progenitor cells in patients with NASH with mild or advanced fibrosis. **C.** Effect of CLDN1 mAb on liver progenitor and mature hepatocyte marker gene sets in humanized NASH fibrosis mice. **D.** Differential expression of a gene set characterizing scar-associated myofibroblasts(*16*) in NASH patients with mild compared to advanced fibrosis. **E.** Effect of CLDN1 mAb on expression of scar-associated myofibroblast marker genes in the regular NASH fibrosis mouse model. **F.** Modulation of fibrogenic and carcinogenic signaling pathways and human cirrhosis gene modules in NASH patients with NASH with mild or advanced fibrosis, humanized NASH fibrosis mice treated with CLDN1 mAb or control and regular NASH fibrosis mice treated with CLDN1 mAb or control. Heatmaps illustrate NES of altered gene sets (all FDR<0.25 except for induction of fibrogenic, KRas signaling and cirrhosis modules #1, #7, #19, #24 and #23 in humanized mice control tissues and reversal of E2F targets, TGF-β signaling and cirrhosis modules #1, #7 and #24 in CLDN1 mAb treated NASH fibrosis mice, FDR>0.25). **G.** RELA, RELB, and p-P38 positive cells were assessed by immunohistochemistry in DEN-CDAHFD mice treated with CLDN1 mAb (*n*= 16 animals per staining) or control (*n*=15 animals per staining). For the RELB analysis, in case of multiple liver specimen from the same mouse, the maximum value per mouse was considered except in case of >5-fold difference between the minimum and maximum value where the mean value was used (U-Test). Vertical bars show mean ±SEM and single data points. Horizontal bars indicate NES of significantly (FDR<0.25) altered gene sets. *p<0.05, U-test.

Figure 6. Targeting CLDN1 inhibits pro-fibrotic signaling mediating cell-matrix interaction and plasticity in hepatocytes. A. Co-immunoprecipitation followed by mass-spectrometry identified CLDN1 interactants. String analysis with MCL clustering is shown. **B.** Validation of the main CLDN1 interactants in Huh7 cells by Western Blot analysis. Negative control is the hepatocyte marker ASGR1. **C.** CLDN1 mAb treatment decreases EGFR phosphorylation in Huh7 cells (representative results of *n*=3 independent experiments are shown). **D.** CLDN1 mAb inhibits ERK phosphorylation in Huh7 cells (representative results of *n*=4 independent experiments are shown). **E.** CLDN1 decreases SRC recruitment at the membrane in Huh7 cells (representative results of *n*=2 independent experiments with *n*=2 biological replicates are shown). **F.** CLDN1 mAb inhibits SRC phosphorylation in Huh7 spheroids (representative results of *n*=4 independent experiments are shown). **G.** Effect of CLDN1 mAb on phosphokinase signaling in the patient-derived NASH liver spheroid model shown in Fig. 4. **H.** Kinome assay of CLDN1 mAb-treated vs. Control mAb-treated patient-derived spheroids. B-F shows representative results out of 3 independent experiments. Full-length Western blots are shown in fig. S16. ASGR1: Asialoglycoprotein Receptor 1; CTRL=Control; FT=Flowthrough; MCL=Markov clustering.

Figure 7. CLDN1 mAb modulates liver progenitor cell phenotype and inhibits profibrogenic differentiation of activated stellate cells. **A.** Left panel: Representative images of human cirrhosis-derived primary liver organoids after 4 days of treatment with CLDN1 or Control mAb. Scale bars=10μm. Right panel: Size (measured as organoid area) of CLDN1 mAb-treated organoids is shows as fold change compared to mean organoid size in Control mAb-treated organoids (2 independent experiments with *n*=3 and *n*=4 replicates per condition respectively, p=0.03, U-test). **B.** Differentially expressed genes in CLDN1 mAb vs. Control mAb-treated liver organoids. **C**. Enrichment of gene sets related to epithelial development in CLDN1 mAb and enrichment of proliferation associated gene sets versus isotype control mAb treated organoids (all: FDR<0.0001, Kolmogorov-Smirnov test). Shown are the most relevant significantly altered pathways**. D.** Expression of progenitor marker *TACSTD2* in human cirrhosis-derived primary liver organoids treated with CLDN1 mAb or Control mAb (*n*=1 donor and *n*=3 independent experiments with *n*=3-4 replicates per condition) is shown as fold change compared to Control mAb-treated cells (p=0.04, U-test). **E.** Effect of CLDN1 mAb on scar-associated myofibroblast type A and B marker genes (table S11-S12) in patient-derived HLMFs. **F.** Enrichment plot for TNF-α-NFκB signaling (HALLMARK_TNFA_SIGNALING_VIA_NFKB) in HLMFs treated by CLDN1 mAb compared to control mAb. **G.** Representative immunoblots of pS32 Ikbα, IkBα, pS536 p65, p65, H3 histone, and beta tubulin in the cytosolic fraction of HLMFs treated with TNF-α for 2h (*n*=3-4 independent experiments with 1 replicate per condition, respectively). **H.** Representative immunoblots of pS465/467 SMAD2/ pS423/425 SMAD3, SMAD2/3, pThr180/Tyr182 p38, p38, pS473 Akt, Akt, pT202/Y204 ERK1/ pT185/Y187 ERK2, ERK, and Actin in HLMFs treated with TGF-β. **I.** Quantification of immunoblots of pT202/Y204 ERK1/ pT185/Y187 ERK2, ERK (*n*= 6), pS473 Akt, Akt (*n*= 4) and pThr180/Tyr182 p38, p38 (*n*= 6) in

HLMFs treated with TGF-β (p=0.02, p=0.03 and p=0.03, U-test, respectively). **J.** Expression of *ACTA2*, *COL1A1* (*n*=7 different donors and independent experiments with N=2-4 technical replicates per condition), and *FN1* in HLMFs (*n*=3 different donors and independent experiments with N=2-4 technical replicates per condition) treated with CLDN1 mAb or control is shown as fold change compared to untreated cells (p=0.003, p=0.01 and p=0.02, Wilcoxon-matched paired test, respectively). Original Western blots are shown in figs. S18-S19. *p<0.05, **p<0.01.

Figure 8. CLDN1 as therapeutic target in fibrotic kidney and lung diseases. **A.** *CLDN1* gene expression in membranous glomerulonephritis renal tissues(*14*) and fibrotic kidney tissue (*38*) compared to respective healthy kidneys. **B.** *CLDN1* gene expression in pulmonary tissues of patients with IPF(*39*). **C.** Illustration of the UUO and bleomycin mouse models of kidney and lung fibrosis. **D.** Representative images of Sirus-red in kidneys from vehicle and CLDN1 mAb-treated animals. **E**. Quantification of collagen proportional area in UUO mice treated with vehicle control, telmisartan or CLDN1 mAb (*n*=8 mice per group). **F.** Representative images of F4/80 immunostaining in kidney tissues of CLDN1 mAb- or control-treated animals. Arrows show macrophage infiltration. **G.** Representative images of Trichrome masson staining of lung tissue from vehicle and CLDN1 mAb-treated animals. **H.** Evaluation of pulmonary fibrosis by Ashcroft score (*52*) in vehicle- (*n*=14), CLDN1 mAb- (*n*=13) and dexamethasone- (*n*=8) treated animals. **I.** Representative images of CLDN1 mAb binding to CLDN1 on lung fibroblasts. Scale bar=100µm. **J.** Kidney fibroblasts and lung fibroblasts were treated with TNF-α (10 ng/mL), IKK-16 (1 µM), TNF-α + IKK16, or vehicle control and subjected to fluorocytometric analysis of CLDN1 mAb H3L3 binding, respectively (3 independent experiments with *n*=3 biological replicates per condition). ΔMFI is shown as fold change compared to untreated cells. **K.** Modulation of gene sets characterizing lung fibrosis-associated fibroblast differentiation states in CLDN1 mAb- or control mAb-treated IPF patient-derived fibroblasts. **L**. Enrichment plot for TNF-α-NFκB signaling (HALLMARK_TNFA_SIGNALING_VIA_NFKB) in IPF fibroblasts treated by CLDN1 mAb compared to control mAb. Vertical bars show mean ±SEM and single data points. Horizontal bars indicate NES of significantly (FDR<0.25) altered gene sets. *p<0.05, ***p<0.001, **** p<0.0001, t-test (**A, E, G, J**) or U-test (B), respectively. IPF=idiopathic pulmonary fibrosis; MFI=Mean fluorescence intensity; UUO=unilateral ureteral obstruction.

MATERIALS AND METHODS

Reagents and antibodies. The following reagents were used for *in vitro* experiments in this study: DMSO, oleic acid and palmitic acid (#D8418, #O1383 and P0500, Sigma-Aldrich), IL6 (Sigma-Aldrich), TGF-β (R&D Systems), IFNγ (Thermo Fisher Scientific), PMA (Sigma-Aldrich). Humanized CLDN1 specific mAb H3L3 has been described(*10*) and was produced by Evitria, Schlieren. Murinized CLDN1 specific mAb (TAR-Rm) was generated by co-transfecting chinese hamster ovary (CHO) cells with plasmids containing appropriate heavy and light chain variants as described(*10*) by Evitria. For proteomic studies, a fully humanized variant derived from the same original OM-7D3-B3 rat anti-human CLDN1 antibody clone (ALE.F02) was used. Differently form H3L3, the Fc region of the ALE.F02 molecule contains three mutations (L234F, L235E and P331S) that have been introduced to reduce binding to Fc gamma receptors whilst maintaining binding to the neonatal Fc receptor. The isotype control antibodies used were palivizumab IgG4(*53*) (RRID: AB_2910861, Evitria) and motavizumab (RRID: AB_2910856, Evitria).

CLDN1 expression analysis in liver tissue by immunohistochemistry, immunofluorescence, and in-situ-hybridization. Immunohistochemistry (total CLDN1): For colocalization experiments, double immunostainings were performed on serial sections (3 µm thick) using Claudin1 antibody (#E-AB-30939, Elabscience) and each of the following 5 different antibodies: rabbit polyclonal anti-human CK19 (RRID: AB_2281020, #ab52625, Abcam) at a 1:400 dilution, rabbit polyclonal anti-human EPCAM (RRID: AB_10984102, #PA5-19832, Invitrogen) at a 1:250 dilution, mouse monoclonal anti-human CD34 (RRID: AB_2074356,

#343607, DakoCytomation) at a 1:600 dilution and mouse monoclonal anti-human CD68 (RRID: AB_2314148, #M0814, DakoCytomation) at a 1:800 dilution. Briefly, 3 µm serial sections of paraffin-embedded livers were submitted to the appropriate antigen retrieval and incubated with rabbit polyclonal anti-human Claudin1 antibody (#E-AB-30939, Elabscience,) at a 1:250 dilution 1 h at room temperature followed by an anti-rabbit antibody (RRID: AB_10015288, #111-006-045, Jackson Immuno Research) for 30 min (room temperature) and then liquid diaminobenzidine substrate–chromogen system (DakoCytomation,). Sections were then incubated with the corresponding second primary antibody for 1 h at room temperature followed by the appropriate second antibody for 30 min and then by phosphatase alkaline-fast red enzyme system (DakoCytomation). Counterstaining was performed using Mayer hematoxylin. Immunohistochemistry (non-junctional CLDN1): Frozen liver sections were air-dried for at least 45 minutes at room temperature (RT) and fixed in zinc formalin for 2 minutes. After rinsing the sections in Millipore water for at least 3 minutes, endogenous peroxidase activity was blocked in a solution of PBS supplemented with 0.3% H_2O_2 for 20 minutes. The sections were washed in PBS tween for 3 min and then blocked with avidin and then biotin for each 30 minutes. After 3 washes in PBS tween, CLDN1 mAb Ale-F02 targeting njCLDN1 was diluted in antibody diluent (Ventana antibody diluent, #06440002001, Roche) supplemented with 10% human serum, and incubated for 1 hour at room temperature. For co-staining with EPCAM, anti-EPCAM antibody (RRID: AB_10984102, #PA5-19832, Thermo Fisher) was added at 5 µg/mL. After 3 washes the streptavidin complex was applied for 20 minutes at RT. After 3 washes, slices were incubated with DAB for 5 minutes at room temperature and then washed in Millipore water for 2 minutes. Counterstaining was performed with hematoxylin (dilution 1/16) for 15 seconds. Slides were thoroughly washed in running tap water for at least 2 minutes. The sections were dehydrated and

all slides were mounted. Immunofluorescence: Multicolor immunofluorescent staining was performed on formalin-fixed paraffin-embedded sections cut at a thickness of 3 µm. First, slides were dewaxed and antigen retrieval was performed in Tris-EDTA buffer (pH8) for 30 minutes at 99°C followed by bleaching to remove autofluorescence. Slides were incubated with primary antibody mixture of anti-alpha-SMA antibody (RRID: AB_2223500, #M0851, Dako, 1/200), anti-CLDN1 antibody targeting total CLDN1 (E-AB-30939, 1/600, Elabscience) and anti-CD68 (RRID: AB_2616797, # 916104, Biolegend, 1/150) for 4 hours, followed by incubation with fluorescence-labelled secondary antibody mixture for 30 minutes. Slides were mounted with mounting medium containing DAPI and images were taken using the Zeiss Axioscan.Z1 slide scanner. In-situ hybridization: RNAscope duplex ISH was performed on the Leica Biosystems BOND RX platform, 4.5 µm sections were baked and deparaffinized on the instrument, followed by target retrieval (30 min at 95°C using Leica Epitope Retrieval Buffer 2) and 5 min protease treatment (Advanced Cell Diagnostics (ACD)). RNAScope probes (ACD) directed against human CLDN1 and human COL3A1 were hybridized for 2 h at 42°C using RNAscope 2.5 LS Duplex Reagent Kit (ACD) followed by RNAscope amplification. Fast red chromogenic detection for detection of COL3A1 was performed first, followed by green chromogenic detection (ACD) for detection of CLDN1. Dihydrodipicolinate reductase (dapB), a bacterial gene, was used as a negative control probe. Sections were counterstained with haematoxylin. Images were acquired using Olympus UC90 camera and Olympus cellSense Entry 2.3 imaging software. Staining quantification was performed using QuPath version 0.3.2(*54*).

Modeling of the claudin-1/antibody complex. Generation of a CLDN1 structural model**:** To date the structure of CLDN1 has not been solved and no structure is available in the protein data bank (PDB)(*55*). We therefore generated an atomistic model by homology modeling. Sequence analysis revealed that claudin-19 (CLDN19) has a sequence similarity of 57% with CLDN1 and was therefore selected as a template. A structural model of CLDN1 was generated and optimized using PRIME, a dedicated pipeline implemented in the Schrodinger suite for molecular modeling(*56, 57*). *Generation of the antibody model:* The structure of the antibody was generated using the antibody modelling pipeline implemented in the Schrodinger suite for molecular modeling(*58-60*)**.** *Molecular dynamics simulations:* To explore conformational variability and dynamics of CLDN1, we performed extensive molecular dynamics simulations. An atomistic model of CLDN1 in a membrane was build using the OPM webserver(*61*). In particular CLDN1 was immersed in a POPC lipid bilayer with a concentration of 0.15M NaCl. Furthermore, the TIP3P model(*62*) was used to describe the water molecules whereas all other parts of the system were described by the OPLS3e force field(*63*). The full system was then equilibrated using the following protocol: 1. Brownian Dynamics was run for 100 ps in an NVT ensemble (T=10 K) applying harmonic restraints on solute heavy atoms (force constant 50 kcal/mol/Å^2); 2. NVT (T=10K) MD simulation of 12 ps in NVT ensemble conserving the same restraints applied in 1.; 3. NPT (T=300K and P=1atm) MD simulation (12 ps) conserving the same restraints applied in 1.; 4. NPT (T=300K and P=1atm) MD simulation (24 ps) without restraints. Pressure and the temperature were fixed at 300 K and 1 atm by the Martyna-Tobias-Klein barostat(*64*) and the Nose-Hoover chain thermostat(*65*), respectively. Three independent production runs of 1 μs were performed. The DESMOND software in its GPU implementation was used as simulations engine(*66*). Last, a cluster analysis was run to extract the most relevant conformations from the

MD trajectories. This analysis was carried out with the ttclust program(*67*). The CLDN1 backbone atoms were considered for both alignment and clustering, the optimal number of clusters was automatically determined using the "elbow" method with kmeans(*68*). *Modeling of CLDN1/antibody complex:* Cluster analysis identified six different clusters. However, only two included more than 20% of the conformations sampled during molecular dynamics. The centers of these two clusters were, therefore, used for the modelling of the structure of the Claudin-1/antibody complex. CLDN1/antibody docking was simulated using the Haddock v2.4 webserver(*69, 70*) as described by and the definition of the epitope given in(*9*). Two complex structures, one for each representative CLDN1 structure, were selected for further investigation. Next, to optimize the CLDN1/antibody interface and account for induced-fit effects on the proteins, two complexes were simulated by MD for 500ns using the same set-up described before, and the trajectories analyzed by cluster analysis. Last, the interaction free energy (ΔG) for the most representative structure from the two largest clusters were computed using the PRODIGY software(*72*) and the model with the best (more negative) ΔG was selected as the final model of the Claudin-1/Antibody complex.

Retrogenix study. Retrogenix's cell microarray technology was performed as described(*73*). Briefly, 5484 expression vectors, encoding both ZsGreen1 and a full-length human plasma membrane protein or a cell-surface tethered human secreted protein were arrayed in duplicate across 16 microarray slides ('slide-sets') for a primary screen. An expression vector (pIRES-hEGFR-IRES-ZsGreen1) was spotted in quadruplicate on every slide and was used to ensure that a minimal threshold of transfection efficiency had been achieved or exceeded on every slide. Human HEK293 cells (RRID: CVCL_0045) were used for reverse transfection/expression.

The test antibody was added to each slide after cell fixation, giving a final concentration of 2 µg/mL. Detection of binding was performed by using AlexaFluor 647 labelled anti-human IgG Fc detection antibody (RRID: AB_2563330, #409320, BioLegend). Fluorescent images were analyzed and quantitated (for transfection) using ImageQuant software. A protein 'hit' was defined as a duplicate spot showing a raised signal compared to background. Hits were classified as 'strong, medium, weak, or very weak', depending on the intensity of the duplicate spots. To confirm the hits and assess specificity, vectors encoding all hits identified in the primary screens, plus vectors encoding CD20 and EGFR, were arrayed and expressed in HEK293 cells (RRID: CVCL_0045) on new slides. Confirmation/specificity screens and analyses were carried out as for primary screening except that identical slides were treated, after cell fixation, with the test antibody individually at the same concentration as before (2 µg/mL), 1 µg/mL Rituximab biosimilar, or no test antibody/secondary only (n=2 slides per treatment).

Isolation of primary liver cells. Mouse: Primary Mouse Hepatocytes (PMH) were isolated from fresh non-diseased mouse liver tissue, as described(*74*). Human: Isolation of PHH and non-parenchymal cells from patients' liver tissue (table S12) was performed as previously described(*75*). Briefly, human liver tissue samples from surgical interventions were digested using a two-step EGTA/collagenase perfusion technique. PHH were depleted by initial centrifugation at 50xg and nonparenchymal cells were further purified by serial centrifugation at different speed and density gradient centrifugation. Fast attachment of Kupffer cells to culture plates as well as magnetic separation of endothelial cells using CD31 microbeads (CD31 MicroBead Kit, human, Miltenyi) further allowed separation and cultivation of HSCs(*75*).

Binding studies of murinized and humanized CLDN1 specific mAbs by flow cytometry. Binding of murinized and humanized CLDN1 mAb to cells was analyzed by flow cytometry with ~$1x10^5$ cells in triplicate per condition. PHH and PMH (primary antibody staining): Isolated PHH and PMH were incubated with increasing concentrations of humanized CLDN1 mAb H3L3 or murinized mAb CLDN1 TAR-Rm (0.01-100 µg/mL), respectively. 293-T cells (primary antibody staining): 293-T cells (RRID: CVCL_4U22) were transfected with plasmids encoding for human or mouse CLDN1 fused with cerulean fluorescent protein or empty plasmid fused with cerulean fluorescent protein (kindly provided by M. Evans, Mount Sinai Hospital, New York). Transfected cells were incubated with increasing concentrations of humanized CLDN1 mAb H3L3, murinized CLDN1 mAb TAR-Rm or the respective isotype control antibodies. Activated hepatic stellate cells (primary antibody staining): Isolated HSCs were differentiated into activated HSCs (aHSCs) within 10 days of culture on plastic (*76*). Phenotypic identity was subsequently confirmed by α-SMA-positive staining using immunofluorescence (see below). For flowcytometric analysis of CLDN1 mAb binding under conditions of inflammation, transdifferentiated aHSCs were treated with TNF-α (10 ng/mL), IKK-16 (1 µM) or TNF-α (10 ng/mL) + IKK-16 (1 µM) for 24 h before incubation with humanized CLDN1 mAb H3L3 or isotype control mAb at 10 µg/mL. Secondary antibody staining (all cell types): After incubation with the respective mAbs concentrations for 1h, all cells were washed and incubated with phycoerythrin (PE)-conjugated species-specific (human or mouse) secondary antibodies (RRID: AB_2337676, #109-116-088 or RRID: AB_2338629, #115-116-146, Jackson Immuno Research) at 4 °C for 45 min to allow detection of binding. Cells were subsequently washed and fixed with 2% paraformaldehyde (PFA). Data were acquired using Cytoflex B2R2V0 (Beckman Coulter) and analyzed using CytExpert 2.1 and FlowJo v10 (Beckman Coulter). All experiments were repeated in at least 3 independent experiments in

triplicate. In case of studies with patients' material, independent experiments with cells derived from at least 3 different donors were performed in triplicate. CLDN1 expression was calculated as the difference of the mean fluorescence intensities of cells stained with CLDN1 mAb and cells stained with the isotype control mAbs. The kinetics of the interaction between humanized or murinized mAb against human or mouse CLDN1, respectively, were determined by gating in cerulean-positive cells using FlowJo and the Michaelis-Menten mathematical model using R 3.5.1 (http://www.R-project.org/).

Liver fibrosis mouse models. All experiments were performed at the animal facility of Inserm U1110 according to local laws and ethics committee approval (institutional protocol approval number APAFiS #3559, #7216 and #32429). The mice were housed in individually ventilated cages with 12h/12h light/dark cycles and *ad libitum* access to food and water. *Pharmacokinetics studies.* Three C3H male mice (RRID:MGI:6197584, 6-8 weeks old) were i.p. injected with 500 µg of murinized CLDN1 specific mAb TAR-R-mIgG. At day 1, 3, 8, and 15 after injection, 100 µL blood was harvested under general anesthesia (isoflurane 3%) by retro-orbital puncture with dry capillaries. Serum concentrations of the murinized CLDN1 specific mAb were quantified by flow cytometry as described(*77*). Briefly, $3x10^4$ CLDN1-overexpressing Huh7.5.1 cells were incubated for 30 min at 4 °C with 20 µL of 1/50-diluted serum or serial concentrations (0, 0.1, 0.3, 1, 3, 10, and 30 µg/mL) of CLDN1-specific mAb TAR-R-mIgG in 1:50-diluted serum from an untreated C3H mouse. After extensive washing, cells were labelled with PE-conjugated goat-anti-mouse Abs (RRID: AB_2338629, #115-116-146, Jackson ImmunoResearch Laboratories) and fixed with 2% paraformaldehyde. Cells were analyzed on a BD LSRII FACS. To determine the mAb concentration at each time point, the PE mean

fluorescence intensity (MFI) of all viable cells in experimental samples were compared with that of the titration curve. The mAb serum concentrations were then plotted against time and the half-life was calculated for each mouse using its regression curve. *DEN-CDA-HFD model:* Forty 7-week old male C57BL/6J mice (RRID: IMSR_JAX:000664, Charles River Laboratories) received a single i.p. injection of DEN (100 mg/kg, Sigma-Aldrich) and were subsequently fed with the CDA-HFD (A06071302, Research Diet) after 3 weeks. After 6 weeks of diet, the mice were randomized in 2 groups, receiving weekly i.p. injections of 500 µg of either CLDN1 specific mAb or vehicle control for 16 weeks. After 16 weeks of treatment, all mice were sacrificed, the blood was sampled and the liver as well as other major organs (brain, heart, lung, kidney, stomach, intestine, spleen, bladder and skin) were harvested and underwent macroscopic and microscopic examination (fig. S8**)**. *Humanized liver NASH mouse model: Fah$^{-/-}$/Rag2$^{-/-}$/Il2rg $^{-/-}$ (FRG) – NOD* (RRID: IMSR_JAX:018454) breeding mice were kept at the Inserm Unit 1110 SPF animal facility and maintained with 16 mg/L of 2-(2-nitro-4-trifluoro-methyl-benzoyl)-1,3 cyclohexanedione (NTBC; Swedish Orphan Biovitrum) in drinking water. Six-week-old mice were intravenously injected with 1.5 x 10^9 plaque forming units (pfu) of an adenoviral vector encoding the secreted form of the human urokinase-like plasminogen activator (Ad-uPA)(*21*). Forty-eight hours later, 10^6 PHH were injected intrasplenically via a 27-gauge needle. For the procedure, the mice were kept under gaseous isoflurane anesthesia and received a subcutaneous injection of buprenorphine at the dose of 0.1 mg/kg. After transplantation, NTBC administration was gradually decreased and completely withdrawn in 7 d. Transplant success was evaluated 2 months after the procedure by dosing human albumin in mouse serum as previously described(*77*). The mice successfully transplanted were fed with CDA-HFD for 16 weeks and then treated with humanized CLDN1-specific mAb 500 µg or vehicle for additional 8 weeks. For the *GalNAc*

siRNA *in vivo* knockdown study, mice successfully transplanted with PHH were fed with CDA-HFD for 12 weeks followed by subsequent subcutaneous injections of *in vitro* validated siRNA targeting the human *CLDN1* or siCTRL (3 mg/kg/week) for 8 weeks. DDC (3,5-Diethoxycarbonyl-1,4-Dihydrocollidine) mouse model: Seven-week-old C57BL/6J male mice (RRID: IMSR_JAX:000664, Charles River Laboratories) were fed a 0.1% DDC-supplemented diet (R03-25, Safe). One week after beginning the 0.1% DDC diet, the mice were randomly assigned to either the treatment group (IP injection of 25 mg/kg/week of H3L3 anti-CLDN1 mAb) or control group (PBS) for three weeks. Mice were sacrificed after 4 weeks of 0.1% DDC diet and plasma and livers were harvested for subsequent analyses. *ELISAs on mouse serum.* CRP was measured in collected plasma of the humanized mice using Human C-Reactive Protein/CRP Quantikine ELISA Kit (#DCRP00, R&D Systems) according to the manufacturer's instructions.

Mouse liver tissue staining analysis

Histological analysis. All organs were immediately fixed in a 10% formalin solution after harvesting and subsequently included in paraffin. Liver slices stained with hematoxylin & eosin (H&E) and Sirius Red were obtained for all mice. For immunohistochemistry staining, the following antibodies were used: CD11c (RRID: AB_2800282, #97585, Cell Signaling), CD3 (RRID: AB_1956722, #MA1-90582, Invitrogen), CD4 (RRID: AB_2573008, #14-9766-82, eBioscience), CD8a (RRID: AB_2572861, #14-0808-82, Invitrogen), CLEC4F (RRID: AB_2081339, #AF2784, R&D Systems), Fibronectin-1 (RRID: AB_732380, #ab45688, Abcam), LY6C (RRID: AB_302004, #ab15627, Abcam), MHC II (RRID: AB_10006678, #NBP1-43312, Novus Biologicals), MPO (RRID: AB_307322, #ab9535, Abcam), REL A (RRID: AB_535932, #NB 100-2176, Novus Biologicals), REL B (RRID: AB_632341, #sc-226, Santa Cruz), pP38

(RRID: AB_2139682, #4511, Cell Signaling), HSP70 (RRID: AB_1150514, #IMG-80181, IMGENEX), FAH (RRID: AB_2678806, #HPA044093, Sigma), α-SMA (RRID: AB_476701, #A2547, Sigma). Staining quantification was performed on entire histological slide or on 5 to 10 consecutive images at 10x or 20x magnification per staining Images were analyzed using ImageJ software v1.51j8 (Rasband W, National Institutes of Health, USA) or QuPath version 0.3.2(*54*).

For the collagen proportional area quantification in humanized areas, two consecutive liver cuts were stained with FAH and Sirius Red. The corresponding FAH-positive area in the Sirius Red histological slide was selected as region of interest and then the collagen proportional area quantified using ImageJ software(*78*). For quantification of other immunostaining in representative humanized area, the humanized areas were selected from the hematoxylin staining based on the phenotype of human hepatocytes showing a brighter cytoplasm and different nucleus and cytoplasm size compared to mouse ones(*21*). All the available tissue slides were analyzed with two exceptions: for α-SMA staining in the DEN-CDAHFD model samples were selected on fibrosis phenotype, for fibronectin-1 analyses of CLDN1 mAb-treated humanized NASH mice of experiment 2, outliers were excluded according to the Rosner test.

In situ hybridization of mouse liver tissues: RNAscope ISH was performed on the Leica BOND III platform, 5 µm sections were baked and deparaffinized on the instrument, followed by target retrieval (30 min at 95°C using EDTA Buffer) and 15 min protease treatment. RNAScope probes (ACD) directed against mouse and *Ccl2*, *Ccl20*, *Cxcl10* were hybridized for 2 h at 42°C. Staining was performed using BOND RNAscope Brown Detection (DS981) and slides were counterstained with haematoxylin. Staining quantification was performed using QuPath version 0.3.2(*54*).

Kidney fibrosis (unilateral ureteral obstruction model, UUO) mouse model: The experiment was conducted by SMC laboratories (Japan) according to local laws and following ethics committee approval (SLMC053-1906-8 (UUO): U015). Seven-week-old female C57BL/6J mice (RRID: IMSR_JAX:000664) were obtained from Japan SLC, Inc. and housed and cared for in accordance with the Japanese Pharmacological Society Guidelines for Animal Use at SMC laboratories, Japan. Animals were housed and fed with a normal diet (CE-2; CLEA Japan) under controlled conditions. On day 0, UUO surgery was performed under mixed anesthetic agents (medetomidine, midazolam, butorphanol). Mice were randomized to receive CLDN1 mAb (500 µg in 100 µL/mouse, *n*=8) or vehicle (100 µL, *n*=8) which were administered intraperitoneally of twice weekly for 14 days. Telmisartan (30 mg/kg, *n=8*) was administered orally once daily for 14 days. The animals were sacrificed by exsanguination through direct cardiac puncture under isoflurane anesthesia (Pfizer Inc.) at day 14. For plasma biochemistry, non-fasting blood was collected in polypropylene tubes with anticoagulant (Novo-Heparin, Mochida Pharmaceutical Co. Ltd.) and centrifuged at 1,000xg for 15 min. at 4 °C. The supernatant was collected and stored at -80 °C until use. Plasma urea nitrogen was measured by FUJI DRI-CHEM 7000 (Fujifilm). *Histological and image analysis.* To visualize collagen deposition, kidney sections were stained using picro-Sirius red solution (Waldeck). For quantification of interstitial fibrosis area, bright field images in the corticomedullary region were captured using a digital camera (DFC295) at 200-fold magnification, and the positive areas in 5 fields/section were measured using ImageJ software. For immunohistochemistry, sections were cut from paraffin blocks and deparaffinized and rehydrated. Endogenous peroxidase activity was blocked using 0.3% H2O2 for 5 min., followed by incubation with Block Ace (Dainippon Sumitomo Pharma Co. Ltd.) for 10 min. The sections were incubated with a 100-fold dilution of anti-F4/80 antibody

(RRID: AB_1227368, #T-2006, BMA Biomedicals) at room temperature for 1 hour. After incubation with secondary antibody (#31470, HRP-Goat anti-rat antibody, Invitrogen), enzyme-substrate reactions were performed using 3, 3'diaminobenzidine/H2O2 solution (Nichirei Bioscience Inc., Japan). For quantitative analysis of inflammation areas, bright field images of F4/80-immunostained sections were captured using a digital camera (DFC295) at 200- and 400-fold magnifications.

Lung fibrosis (Bleomycin-induced) mouse model. The experiment was conducted by SMC laboratories (Japan) according to local laws and following ethics committee approval (SLMP052-1906-7 (IPF): B048). Six-week-old female C57BL/6J mice (RRID: IMSR_JAX:000664) were obtained from Japan SLC, Inc. and housed and cared in accordance with the Japanese Pharmacological Society Guidelines for Animal Use at SMC laboratories. Animals were housed and fed with normal diet (CE-2; CLEA Japan) under controlled conditions. On day 0, mice were anesthetized with a mixture of medetomidine (Nippon Zenyaku Kogyo), midazolam (Sandoz K.K.) and butorphanol (Meiji Seika Pharma) anesthesia and intratracheally administered BLM (Nippon Kayaku) in saline at a dose of 3 mg/kg, in a volume of 50 µL per animal using a Microsprayer (Penn-Century). Mice were randomized to receive CLDN1 mAb (500 µg/mouse and 5 mL/kg, *n*=9) or vehicle (5 mL/kg, *n*=9) which were administered intraperitoneally twice weekly from day 0 to 20. Dexamethasone (0.25 mg/kg, *n*=9) was administered orally once daily from day 0 to 20. The animals were sacrificed at day 21 by exsanguination through the abdominal aorta under a mixture of medetomidine, midazolam and butorphanol anesthesia. *Histological and image analysis.* Right lung tissues prefixed in 10% neutral buffered formalin were embedded in paraffin and sectioned at 4 µm. For Masson's

Trichrome staining, the sections were stained with Masson's Trichrome staining Kit (Sigma) according to the manufacturer's instructions. The degree of pulmonary fibrosis was evaluated using the Ashcroft score(*52*).

Non-human primate study. The experiment was performed by Charles River Laboratories from February to April 2020 according to local laws and following ethics committee approval under study number CRL 20229915. The animals were housed in the Charles River Laboratories France Safety Assessment SAS test facility (France). This dose-ascending study was performed with the fully humanized variant Ale-F02. Five groups of cynomolgus monkey aged from 29 to 33 month were included in the study. Groups 1 to 3 included 1 animal while groups 4 and 5 two animals per group. Animals in group 1 were treated with an intravenous CLDN1-specific mAb injection at 0.3 mg/kg, in group 2 at 3 mg/kg, in group 3 at 15 mg/kg, in group 4 at 60 mg/kg, in group 5 at 150 mg/kg. The groups 1 to 3 received a single administration, while groups 4 and 5, a weekly injection for a total of 4 doses (Day 1, 8, 15 and 22). The animals were observed for 6 weeks. Parameters monitored included morbidity/mortality, clinical signs, injection site observations, body weights, food consumption and clinical pathology parameters (hematology, coagulation, clinical chemistry and urinalysis). All animals were sampled for toxicokinetic on Day 1, before and at various time points after dosing and on Days 7, 14, 21 and 29 as well as Day 42 for animal 1 to 3 only.

Pharmacokinetic modeling was performed by LYO-X (Allschwil); in brief, for parameter estimation and diagnostic plots, Monolix Suite 2019R2, and for the human PK-binding simulations, Simulx (Monolix Suite 2019R2), mlxR 4.1.0 (Lavielle 2019) and R 3.6.0 (R Development Core Team 2008) were used.

Functional assessment of the murinized CLDN1-specific mAb. Mouse CLDN1-transfected 293-T cells were pre-incubated with murinized CLDN1 mAb or its corresponding murinized isotype control mAb (100 µg/mL) for 1 h at 37 °C and subsequently exposed to HCV pseudoparticles (HCVpp) for 4 h at 37 °C, as described(*79*). HCVpp entry was analyzed by measuring intracellular luciferase activity after 72 h (relative light units, RLU). Inhibition was expressed as a percentage relative to cells treated with the corresponding murinized isotype control mAb as described(*77*).

RNA extraction from human and murine liver tissue. Liver cells were lysed in TRI-reagent (Molecular Research Center) using GentleMACS Octo Dissociator, and RNA was purified using Direct-zol RNA MiniPrep (Zymo Research) according to the manufacturer's instructions. RNA quantity and quality were assessed using NanoDrop (ThermoScientific). Gene expression profiling was performed using 250-500 ng total RNA.

***Prognostic liver signature expression analyses*.** Profiling of the prognostic liver signature (PLS) was performed using Nanostring nCounter assay as described(*80*). Induction or suppression of the PLS in gene expression data was determined as previously reported using the Gene Set Enrichment Analysis (GSEA)(*81*), implemented in GenePattern genomic analysis toolkits. False discovery rate (FDR) <0.25 was regarded as statistically significant(*81*). PLS was always determined by using control cells, control animals, or control patient-derived tissues as references. Results are presented as simplified heatmaps showing the classification of PLS global status as poor or good prognosis and the significance of induction/suppression of PLS genes (log10 of FDR

values). Global status corresponds to the difference between low-risk and high-risk gene enrichments.

ChIPseq and CUT&TAG assay. LX2 cells (RRID: CVCL_5792) were incubated 24h with or without 100 ng/mL TNF-α (Peprotech, #300-01A) and scraped. The CUT&Tag assay against H3K27ac (RRID: AB_2561016, #39133, Active motif) or NF-κB p65 subunit (RRID: AB_10828935, #6956, Cell Signaling Technology) were performed following the manufacturer's instructions (Active motif CUT&Tag-IT Assay Kit, #53165, #53160). Briefly, $1x10^6$ cells per conditions were used. The cells were washed 2 times before binding on Concavalin A beads and then incubated overnight with primary antibody at the recommended dilution (1:50) or no primary antibody (negative control). The next day the corresponding secondary antibody, guinea pig anti-rabbit antibody or rabbit anti-mouse antibody (RRID: AB_11024108, NBP1-72763, Novus Biologicals or AB_228419, #31188, Thermo Fisher) were used at 1:100 dilution in digitonin buffer and incubated at room temperature for 1 hour. The CUT&Tag-IT Assembled pA-Tn5 Transposomes were incubated for 1 hour at room temperature before tagmentation. Cells were resuspended in tagmentation buffer and incubated at 37°C for 1 hour, then the tagmentation process was stopped by addition of EDTA and SDS. Protein digestion was performed by the addition of 80 µg/mL of proteinase K and incubated at 55°C for 60 minutes. DNA was retrieved using DNA purification columns following the manufacturer's instruction. Library preparation and PCR amplification were done using the Kit primers and purified by 2 successive washes with SPRI beads (1.1 µL/sample volume). Samples were subjected to paired-end sequencing by the GenomEast platform on Illumina HiSeq 4000 instrument. The reads were mapped to the HG38 genome by BWA and peak-calling was performed by MACS2. For H3K27ac 48741 and 61571

peaks were detected in absence and presence of TNF-α, respectively, whereas for p65, 16391 and 50160 peaks were detected in absence and presence of TNF-α, respectively. RSAT analyses (http://rsat.sb-roscoff.fr/peak-motifs_form.cgi) of the 100 bp surrounding the top p65 1000 peaks in absence and presence of TNF-α confirmed a strong enrichment of the RelA/NF-kB recognition motifs in the TNF-α-treated sample.

Organovo ExVivo Human Liver Tissue NASH fibrosis model. The study was conducted by Organovo. PHHs and nonparenchymal cell populations (LECs, HSCs and Kupffer cells) cultured in conditioned medium (sugars, free fatty acids and inflammatory inducers) were bioprinted in 3D using the NovoGen Bioprinter platform as described(*28*). Four NASH induced ExVivo Human Liver Tissues with Kupffer cells per condition were exposed to Vehicle, CLDN1 mAb H3L3 or isotype control mAb at 10 or 100 µg/mL daily for 21 days. After 21 days, tissues were stained with hematoxylin and eosin and Trichromic Masson. Eight sections of each tissue replicate underwent histological quantification. One image per each of the eight sections for the four tissue replicates stained with Trichromic Masson underwent fibrosis quantification (total 32 images). Samples treated with isotype and CLDN1 mAbs (10 µg/mL) were selected for comparative quantitive analyses. Image analysis was performed using ImageJ software.

Patient-derived liver spheroids and tumorspheres. Liver tissues from patients with or without chronic liver disease (table S7) were gently digested using a two-step digestion method as described(*25, 75*). The sample was then washed with PBS 1x and loaded on a 70 µm cell strainer. Digested tissue was gently smashed, and the cell strainer washed with up to 10 mL PBS 1x.

Collected cell clusters were further filtered through a 0.45 µm filter and centrifuged for 5 min at 800xg. The cell pellet containing all liver cell types was then re-suspended in Mammocult basal medium (StemCell), supplemented with human proliferation supplement (3.4%), hydrocortisone (0.056%) and heparin (0.011%) and cultured in 96-well ultra-low attachment plates (Corning, Sigma Aldrich). Cell characterization in spheroids by immunofluorescence: Spheroids were fixed with formaldehyde (4% for 2 hours), permeabilized with Triton 0,5%, blocked with 5% FBS, and incubated with ASGPR1- PE (REA608, Miltenyi, 1:50), αSMA (RRID: AB_2223021, #ab5694, Abcam, 1:50), CD68 (RRID: AB_1089059, #333801, Biolegend, 1:50) or CD31-FITC (RRID: AB_2160882, #3528, Cell signaling, 1:50) overnight. Respective species-specific secondary antibodies (RRID: AB_2338078, #111-605-144 or AB_2338840, #115-545-003, Jackson Immuno Research) were added for 1h, followed by washing steps. Spheroids were visualized by Celigo imaging cytometer. Spheroid fibrosis model: 150.000-200.000 cells per well were suspended in Mammocult complete medium (STEMCELL Technologies) supplemented with 20% donor-derived serum (or 20% FBS if donor-derived serum was not available) and seeded on a 96-well low-attachment plate (Corning), then spun at 300g for 5 minutes and incubated overnight. The day after, spheroids were treated with Mammocult complete medium plus 20% serum supplemented with a 2-fold concentrated mixture of oleic acid, palmitic acid, TGF-β, LPS, and either CLDN1 monoclonal antibody or isotype control antibody to reach the final concentrations of 800 µM, 400 µM, 10 ng/mL, 100 ng/mL, and 10 µg/mL, respectively. Vehicle-treated spheroids served as control. Seventy-two hours later, spheroids were lysed, and RNA was extracted using Arcturus PicoPure RNA Isolation Kit (Applied Biosystems). Subsequently, total RNA was reverse transcribed (H Minus First Strand cDNA synthesis Mix, ThermoScientific) on a Thermocycler

(Bio-Rad T100, Bio-Rad, Hercules). Quantitative PCR was performed on the CFX96 Touch Real-Time PCR Detection system with 10 µL reaction volumes containing 5 µL SYBR Green 2x mix (Bio-Rad), 2 µL of RNAse-free water and 250 nM gene specific sense and antisense primers. For qPCR analyses Prime PCR SYBR Green Assays for *COL1A1*, *COL3A1 and COL4A1* (Biorad) were applied according to the manufacturer's instructions. qPCR for *CTGF* and *TACSTD2* was analysed with the following primer sequences: *CTGF*: Fw: 5'-ACC GAC TGG AAG ACA CGT TTG, Rv: 5'-CCA GGT CAG CTT CGC AAG G; *TACSTD2*: Fw: 5'-CCT GAA CGC AGT TTG GAT GTC-3', Rv: 5'-GTA AGG GCA AGC TGA AGA ATA AAT AGA (*82*). Gene expression were normalized to the housekeeping gene *HPRT1* (Fw: 5'-CTG GAA AGA ATG TCT TGA TTG TGG, Rv: 5'-TTT GGA TTA TAC TGC CTG ACC AAG) using the ΔΔCt method (*83*). Assessment of collagen deposition in spheroids: Healthy liver tissue (**table S7**) was processed into multicellular spheroids, stimulated with FFA (100 ng/ml), LPS (100 ng/mL), and TGF-β (10 ng/mL) and then treated with resmetirom (10 µM), isotype control antibody (10 µg/mL), or CLDN1 mAb (10 µg/mL) for 4 days. Total collagen deposition was quantified using Total Collagen Assay Kit perchlorate-free (Abcam), according to the manufacturer's instructions.

Patient-derived liver organoids: Organoid establishment and expansion: Organoids were established from non-tumorous cirrhotic liver tissue from a patient undergoing liver resection for HCC as described(*36*). Briefly, liver tissue was dissociated using Tumor dissociation kit, human (#130-095-929, Miltenyi Biotec) and the gentleMACS Octo Dissociator (Miltenyi) according to the manufacturer's instructions. Total cell population was passed through a 75 µm cell filter and washed 2 times with PBS and centrifuged at 500g, 5 min, 4°C. 10 x 10^3 cells were then re-

suspended in 50 µL Corning Matrigel Growth Factor Reduced Basement Membrane Matrix (#354230, Corning) and seeded as domes onto 24 well plates. Following incubation for 15 min at 37°C, 500 µL prewarmed initiation medium was added to each well. Once formation of organoids was microscopically detected, initiation medium was refreshed by pre-warmed expansion medium and medium was replaced every 2-3 days. Organoids were passaged every 1-2 weeks and cells of passage 4 were used for perturbation studies. Organoid perturbation study (3 independent experiments): Organoids from passage 3 were harvested and washed. Pre-washed organoid cell pellet was pre-incubated with 10 µg/ml CLDN1 mAb or isotype control mAb in PBS for 1h at room temperature. The cell pellet was then washed once with PBS and resuspended in Matrigel and seeded as 25 µL domes onto 48-well plates. After solidification of Matrigel for 15 minutes at 37°C, 500 µL prewarmed initiation medium supplemented by 10 µg/ml CLDN1 mAb or isotype control was added to each well. The experiment was performed with 3-4 replicates per condition. Organoids were incubated for 4 days at 37°C, representative microscopic images were collected and organoids were harvested for RNA extraction using Qiagen RNeasy Mini extraction kit (#4106, Qiagen) according to the manufacturer's instructions. Organoid size diameter was measured in representative microscopic images at 50-100x magnification using ImageJ.

Precision cut ex vivo liver slice culture. Liver tissue slices (200-500 µm-thick) were prepared from surgically resected non-tumorous liver tissues from patients with NASH who underwent liver resection for HCC (**Fig. 4H-I**) (table S7**)** and from patients without liver disease undergoing liver resection for metastasis of colorectal cancer (fig. S12D) (table S8**).** The slices derived from adjacent non-tumorous tissue were cultured with CLDN1 specific mAb or isotype

control mAb (10 µg/mL) for 24 h and harvested for gene expression analysis, as described above. Gene expression data from non-diseased liver tissues (University Strasbourg NASH cohort, table S1) were used as reference controls to verify the induction of the PLS in the studied NASH patients. For non-diseased tissues, the PCLS were cultured in William's E complete medium supplemented with 20% patient serum and were subjected to LPS treatment (100 ng/mL) to induce inflammation and to treatment with control (palivizumab IgG4(*53*)) or CLDN1 mAb (50 µg/mL). After 3 days, the tissues were harvested and proteins extracted to assess effect of the treatment on EGFR and SRC phosphorylation.

Genome wide RNA-seq analyses. RNA-Seq libraries were generated from 300 ng of total RNA using TruSeq Stranded mRNA Sample Preparation Kit (Illumina, Part Number RS-122-2101). Briefly, following purification with poly-T oligo attached magnetic beads, the mRNA was fragmented using divalent cations at 94 °C for 2 min. The cleaved RNA fragments were copied into first strand cDNA using reverse transcriptase and random primers. Strand specificity was achieved by replacing dTTP with dUTP during second strand cDNA synthesis using DNA Polymerase I and RNase H. Following addition of a single 'A' base and subsequent ligation of the adapter on double stranded cDNA fragments, the products were purified and enriched with PCR (30 sec at 98 °C; [10 sec at 98 °C, 30 sec at 60 °C, 30 sec at 72°C] x 12 cycles; 5 min at 72°C) to create the cDNA library. Surplus PCR primers were further removed by purification using AMPure XP beads (Beckman Coulter) and the final cDNA libraries were checked for quality and quantified using 2100 Bioanalyzer (Agilent). Libraries were sequenced on the Illumina HiSeq 4000 as Single-Read 50 base reads following Illumina's instructions. Image analysis and base calling were performed using RTA v2.7.3 and bcl2fastq v2.17.1.14.

In vitro perturbation studies on human activated stellate cells (aHSCs). Isolated human hepatic stellate cells (HSCs) (*75*) were seeded at a density of 5 x 10^4 cells/cm^2 in DMEM with 10% FBS on collagen-coated 12-well plates. After 10 days of cultivation on plastic, all cells showed a myofibroblast-like phenotype consistent with an activated stage (*76*). At this stage (10d of culture), identity and purity of aHSCs were validated by expression of α-SMA (RRID: AB_2223021, Abcam), as assessed by immunofluorescence (see below). For analysis of CLDN1 mAb effects on aHSCs activation markers, primary aHSCs were seeded at 5 x 10^4 cells/cm^2 in 12-well plates and treated with CLDN1 mAb (50 µg/mL) or vehicle control for 3 days. aHSCs were derived from n=7 different donors (table S12**)** and experiments were performed in triplicate per condition and donor.

Immunofluorescence on isolated cells. Cells were seeded onto 8-chamber cover glasses (Lab-Tek II #1.5, Sigma-Aldrich). The next day, cells were washed twice with PBS and fixed with 4% PFA for 15 min at room temperature, followed by permeabilization with 0.1% Triton-X for 10 min. After two washing steps, cells were blocked for 30 min with 10% FBS. Primary antibody staining with anti-α-SMA Ab (RRID: AB_2223021, #ab5694, Abcam, 1:100) or anti-CD68 (#CSB-PA282654, CUSABIO, 1:100) and CLDN1 mAb H3L3 or control mAb (10 µg/mL, respectively) was performed overnight at 4 °C. Cells were washed with PBS and incubated with goat anti-human Alexa Fluor 488 and/or goat anti-rabbit Alexa Fluor 647 secondary antibodies (RRID: AB_2337831, #109-515-003 or AB_2338078, #111-605-144, Jackson Immuno Research) at a dilution of 1:200. Nuclear staining was done using DAPI (1 µg/mL) and cells were visualized

using epi-fluorescence and confocal microscopy. Results were confirmed in at least 3 independent experiments.

Gene expression analyses in 2D cell culture experiments. Total RNA extraction from 2D cell cultures was performed using RNAeasy Mini Kit (Quiagen) according to the manufacturer's instructions. Subsequently, 100-500 ng RNA was reverse-transcribed (H Minus First Strand cDNA synthesis Mix, ThermoScientific) on a Thermocycler (Bio-Rad T100, Bio-Rad, Hercules). Quantitative PCR was performed on the CFX96 Touch Real-Time PCR Detection system with 20 µL reaction volumes containing 10 µL SYBR Green 2x mix (Bio-Rad), 4 µL of RNAse-free water and 250 nM gene specific sense and antisense primers. The primer sequences were as follows: *ACTA2* Fw: 5'-TGA AGA GCA TCC CAC CCT, Rv: 5'-ACG AAG GAA TAG CCA CGC; *COL1A1:* Fw: 5'-CCT CAA GGG CTC CAA CGA G, Rv: 5'-TCA ATC ACT GTC TTG CCC CA; *TNFA:* Fw: 5'-GAG GCC AAG CCC TGG TAT G, Rv: 5'-CGG GCC GAT TGA TCT CAG C; *IL6:* Fw: 5'-ACT CAC CTC TTC AGA ACG AAT TG, Rv: 5'-CCA TCT TTG GAA GGT TCA GGT TG; *TIMP1:* Fw: 5'-GCC CAG AGA GAC ACC AGA GAA C, Rv: 5'-CTA TCA GCC ACA GCA ACA AC AGG. All gene abundances were normalized to housekeeping genes *HPRT1* (Fw: 5'-CTG GAA AGA ATG TCT TGA TTG TGG, Rv: 5'-TTT GGA TTA TAC TGC CTG ACC AAG in HLMFs) and *GAPDH* (Fw: 5'-GTC TCC TCT GAC TTC AAC AGC G, Rv: 5'-ACC ACC CTG TTG CTG TAG CCA A) using the ΔΔCt method(*83*).

Western blot analyses of signaling in 2D culture. TNF-α signaling: $1x10^6$ aHSCs were treated with CLDN1 mAb (10 µg/mL) or control mAb (10 µg/mL) for 3 days in serum free media. At day 3 post-treatment, aHSCs were treated again with CLDN1 mAb (10 µg/mL) or control mAb

(10 µg/mL) for an additional 6h, followed by TNF-α stimulation (10 ng/mL) for 2 hours. Cytoplasmic and nuclear cell fractions were then isolated using the Cell Fractionation Kit (Abcam, ab109719) according to the manufacturer's instructions. Briefly, cells were collected, resuspended in buffer A and permeabilized with detergent I. Following incubation for 7 minutes on a rotator at RT and centrifugation at 10,000 x g for 1 min, the resultant supernatant fraction was collected and considered the cytosol fraction. Following resuspension in buffer A and solubilization with detergent II, the cytosol-depleted pellet was centrifuged at 10,000 x g for 1 minutes. Supernatant was discarded and cell pellet was resuspended in buffer A and considered the nuclear fraction. Protein expression in each fraction was assessed by immunoblotting, with histone H3 (RRID: AB_302613, #ab1791, Abcam) and tubulin (RRID: AB_1952434, #GTX101279, GeneTex) antibodies being used as markers for nuclear and cytoplasmic fraction, respectively. For immunoblotting, the following primary antibodies were used: p65 (RRID: AB_628017, #sc-8008, Santa Cruz Biotechnology), P-p65 (RRID: AB_331284, #3033, Cell Signaling technology), IkB (RRID: AB_390781, #4814, Cell Signaling technology), and P-IkB alpha (RRID: AB_561111, #2859, Cell Signaling technology). TGF-β signaling: $1x10^5$ aHSCs were treated with CLDN1 mAb (10 µg/mL) or control mAb (10 µg/mL) for 3 days in serum free media. At day 3 post-treatment, aHSCs were stimulated with TGF-β (10 ng/mL) for 1 hour to assess SMAD2/3, p38 and ERK pathways, or 2 hours to assess Akt pathway. RepSox (2 µM, ab142139, Abcam), SML0543 (10 µM, Sigma Aldrich), U0126 (10 µM, Sigma Aldrich) or Wortmannin (10 µM, W3144, Sigma Aldrich) were used as inhibitors of SMAD2/3, p38, ERK and Akt signaling, respectively. The following primary antibodies were used: SMAD 2/3 (RRID: AB_10889933, #8685, Cell Signaling technology), P-SMAD 2/3 (RRID: AB_2631089, #8828, Cell Signaling technology), p38 (RRID: AB_330713, #9212, Cell Signaling technology), P-p38 (RRID: AB_2139682, #4511, Cell

Signaling technology), ERK1/ERK2 (RRID: AB_2140121, #MAB1576, R&D Systems), P-ERK1/ERK2 (RRID: AB_354539, #AF1018, R&D Systems), Akt (RRID: AB_915783, #4691, Cell Signaling technology) and P-Akt (RRID: AB_2315049, #4060, Cell Signaling technology). EGFR signaling: $1x10^5$ Huh7 were treated with CLDN1 mAb (10 µg/mL) or control mAb (10 µg/mL) for 2 days. Medium was then changed to a serum free one, and cultures were treated for 1 additional day with CLDN1 mAb (10 µg/mL) or control mAb (10 µg/mL). Huh7 were stimulated with EGF (10 ng/mL) for 6 hours. Erlotinib (50 nM) was used as inhibitor of EGFR signaling. The following primary antibodies were used: EGFR (RRID: AB_331707, #2232, Cell Signaling technology) and p-EGFR (RRID: AB_2096270, #3777, Cell Signaling technology). SRC (RRID: AB_2106059, #2109, Cell signaling technology), P-SRC (Tyr416) Antibody (RRID: AB_331697, #2101, Cell Signaling technology). Secondary antibodies used were peroxidase AffiniPure goat anti-rabbit IgG (H+L) mAb (RRID: AB_2307391, #111-035-144, Jackson ImmunoResearch) or ECL mouse IgG, HRP-linked whole Ab (RRID: AB_772210, #NA931, Amersham). Protein immunodetection of the membranes was performed with Clarity ECL Western Blot Substrate (Biorad) in a ChemiDoc MP Imaging System (Biorad).

Cell-based models for chronic liver disease. Huh7.5.1 (RRID: CVCL_E049) and LX2 stellate cells (RRID: CVCL_5792) were cultured in Dulbecco's Modified Eagle Medium (DMEM) containing 10% fetal bovine serum (FBS) and 1% DMSO for differentiation ($Huh7.5.1^{dif}$ cells) as described(*84-86*). NTCP-overexpressing HepG2 (HepG2-NTCP, RRID: CVCL_JY40) cells were selected using puromycin and cultured in DMEM with 10% FBS as previously described(*87*). HCV*:* DMSO-differentiated $Huh7.5.1^{dif}$ cells were plated in 6-well plates and infected with HCVcc Jc1 (genotype 2a/2a) as described (*86*). HCV infection was assessed at day 10 by qRT-

PCR of intracellular RNA as described (*86*). CLDN1 mAb or control mAb (palivizumab IgG4(*53*)) (10 µg/mL, respectively) were added for 3 days after HCV infection. HBV*:* HepG2-NTCP cells (RRID: CVCL_JY40) were plated in 12-well plates and infected with HBV purified from patient serum(*87*) in presence of CLDN1 mAb or control mAb (10 µg/mL, respectively). HBV infection was assessed at day 7 post-infection by qRT-PCR quantification of HBV pre-genomic RNA (pgRNA)(*87*). FFA-NASH model: DMSO-differentiated Huh7.5.1^{dif} cells co-cultured with LX2 cells (20%) were plated in 12-well plates and exposed to FFA (800 µM oleic acid and 400 µM palmitic acid) for 48 hours as described(*88*). CLDN1 mAb or control mAb (10 µg/mL, respectively) were added for 3 days after FFA treatment. Ethanol-ALD model*:* DMSO-differentiated Huh7.5.1^{dif} cells were plated in 6-well plates and exposed to ethanol (40 mM) in presence of CLDN1 mAb or control mAb (10 µg/mL, respectively) for 10 days. Fresh medium containing ethanol and mAbs was replenished daily. Each cell culture model was assessed in at least three independent experiments, performed in triplicate.

Analysis of phosphokinase phosphorylation. Phosphokinase phosphorylation was assessed in cell lysates derived from the NASH *in vitro* model using the Proteome Profiler Human Phosphokinase Array Kit (R&D Systems Inc.), according to the manufacturer's instructions. Phosphokinases were assessed using biotinylated detection antibodies followed by chemiluminescence detection.

Pamgene kinase activity profiling in patient-derived spheroids. Protein tyrosine kinase (PTK) and serine-threonine kinase (STK) activities in the patient-derived 3D model of fibrosis were assessed by PamGene Assay (PamGene International BV). Patient-derived spheroids were

established and treated with a profibrogenic cocktail as described above. After the 72h treatment, 4 spheroids were pooled in each biological quadruplicate and proteins were extracted using M-PER Mammalian Protein Extraction Reagent (ThermoFisher Scientific). Samples were then spun at 16000g for 15 minutes to remove debris. One µg protein were applied on PamChip4 arrays containing 196 (PTK) or 144 (PTK) peptides harboring kinase targets/substrates. Fluorescence-labelled antibodies against phosphoresidues were used to measure kinase activity in the samples. Phosphosites were selected for subsequent analyses if their signals were statistically significantly different between conditions (by t-test or ANOVA). The signal per phosphosite is the result of the net phosphorylation attributed to the activity of one or more kinases (*89*, *90*)**.** Instrument operation and imaging were controlled by the EVOLVE 2.0 software and quantified using BioNavigator 6.3 (BN6; PamGene International BV). Signal intensities at multiple exposure times were integrated by linear regression (S100), Log2-transformed, and normalized using a Combat correction model for batch correction where the scaling parameters (mean and sd) were estimated using an empirical Bayesian approach. By interpreting kinase activity at multiple phosphosites, an Upstream Kinase Analysis (UKA) was performed. Exploiting knowledge on specific kinase-to-substrate relationships from publicly available databases, UKA algorithm predicts differential kinase activity in the test condition compared to the control. Kinase statistic represents the change in kinase activity, indicating inhibition if <0 and activation if >0. Mean specificity score represents the specificity of the change in kinase activity, higher scores highlighting a lower chance of observations descending from random set of peptides(*91*)**.** The hits of our PamGene assay were then ordered by Median Final Score, a synthetic measure of both target robustness and significance. The 20 top hits were plotted in a heatmap comparing Mean Kinase Statistics of our

model vs those of a recently published liver kinome atlas, established with the same technique (*34*).

CLDN1 knockout using CRISPR-Cas9 technology. Huh7.5.1 stably expressing Cas-9 endonuclease (Huh7.5.1-Cas9) were DMSO-differentiated for 7 days (Huh7.5.1-Cas9^{diff}), and then either co-cultured with LX-2 stellate cells (RRID: CVCL_5792, 20%) and treated with free fatty acids (FFA; 800 µM oleic acid and 400 µM palmitic acid) or infected using HCV Jc1. After 3 (FFA treatment) or 7 days (HCV Jc1 infection), cells were transduced with lentiviruses expressing control single guide RNA (sgRNA) or sgRNA targeting *CLDN1* gene expression (sgCLDN1). Expression plasmids were provided by Dr. David Root (Broad Institute of Harvard and MIT, Cambridge, USA). Transduced cells were selected under hygromycin treatment (500 µg/mL) for 3 days and lysed using iScript RT-qPCR sample preparation reagent. The HCV- or FFA-induced PLS was analyzed using nCounter Nanostring technology in cell lysates. In parallel, cells were used to analyze CLDN1 abundance by flow cytometry using a CLDN1-specific mAb (H3L3, 10 µg/mL).

CLDN1 knockdown using GalNAc technology. The following siRNA sequences were designed to target human *CLDN1* or used as non-targeting siRNA (CTRL): *siRNA CLDN1:* 5'-UAACAUUAGGACCUUAGAAUU-3' *siRNA CTRL:* 5'-UAAGGCUAUGAAGAGAUAC-3'. siRNA were then coupled to GalNac group (Creative Biogene Inc.) for *in vivo* delivery. To validate the efficacy of GalNac siRNA, Huh7 cells were transfected with 12 pmol of regular siRNA or GalNac siRNA and the corresponding CTRLs by using lipofectamine RNAi Max (Invitrogen,

Cat#13778-150) following the manufacturer's instructions. Knock-down was validated by detecting CLDN1 at the cell surface by flow cytometry (see above).

CLDN1 co-immunoprecipitation. For co-immunoprecipitation (co-IP), 5.10^8 Huh7 cells (RRID: CVCL-0336) were harvested by scraping in cold $PBS^{-/-}$ and plasma membranes were extracted by using "Plasma Membrane Protein Extraction Kit (Abcam ab65400) according to manufacturers' instructions. Approximatively 100 µg of plasma membranes were resuspended in 250 µL of co-IP buffer (10 mM Tris HCl pH 7.4, .15 M NaCl, 1 mM EDTA, 1 mM EGTA pH 8, 0.1 % NP40, glycerol 10 % in H20 milliQ water supplemented with protease inhibitors). For WB analysis, 50 µL of the total plasma membrane proteins were conserved and used as "Input" control. In parallel, 50 µL of magnetic Dynabeads (ThermoFisher) were coupled to 2 µg of CLDN1 antibody targeting the C-terminus part of the protein to capture membrane interactants (rabbit anti-human CLDN1 antibody, ab211737, Abcam) or CTRL antibody (Recombinant Rabbit IgG, monoclonal Isotype Control, RRID: AB_2687931, ab172730, Abcam) 10 min at RT. Dynabeads were then mixed with 150 µL of co-IP buffer and 100 µL of plasma membranes and incubated at 4°C on an orbital shaker. Lasst, Dynabeads were harvested using a magnet (the "Flow-through" was conserved for WB analysis) and washed 3 times with cold $PBS^{-/-}$. CLDN1 interactants were eluted in 1X Laemmli buffer by heating the beads 5 min at 95°C. CLDN1 IP was validated by WB analysis before analyzing the interactants by mass-spectrometry (IGBMC proteomic platform, Illkirch-Graffenstaden).

Single-cell and single nucleus RNAseq analyses. Single-cell (sc) RNAseq data: Based on the clustering and data normalization of the whole human liver cell atlas (GSE124395)(*15*), we

analyzed *CLDN1* expression in different cell types. Thereby, we used RaceID methods to draw expression t-SNE maps and ggplot2(*92*) to draw corresponding boxplots of normalized expression values. Based on the clustering and provided data of the fibrotic liver cell atlas (GSE136103), we analyzed CLDN1 expression in different cell types. We used Seurat(*93*) to generate expression UMAPs and violin plots, and ggplot2(*92*) to generate correlation figures. Single nucleus (sn) RNAseq data: Based on the clustering of the whole snRNA-seq data set as published in(*21*), we analyzed *CLDN1* expression using Seurat(*93*). We extracted all epithelial cell clusters (hepatocytes, cholangiocytes and bipotent progenitor cells) and performed a pseudotime analysis applying slingshot(*50*). Cell types were annotated based on specific marker gene expression including *ALB* (hepatocytes), *EPCAM* (bipotent progenitor cells), and *CK19* (cholangiocytes). An expression plot overlayed with the resulting pseudotime trajectories was generated using ggplot2(*92*).

SUPPLEMENTARY FIGURES

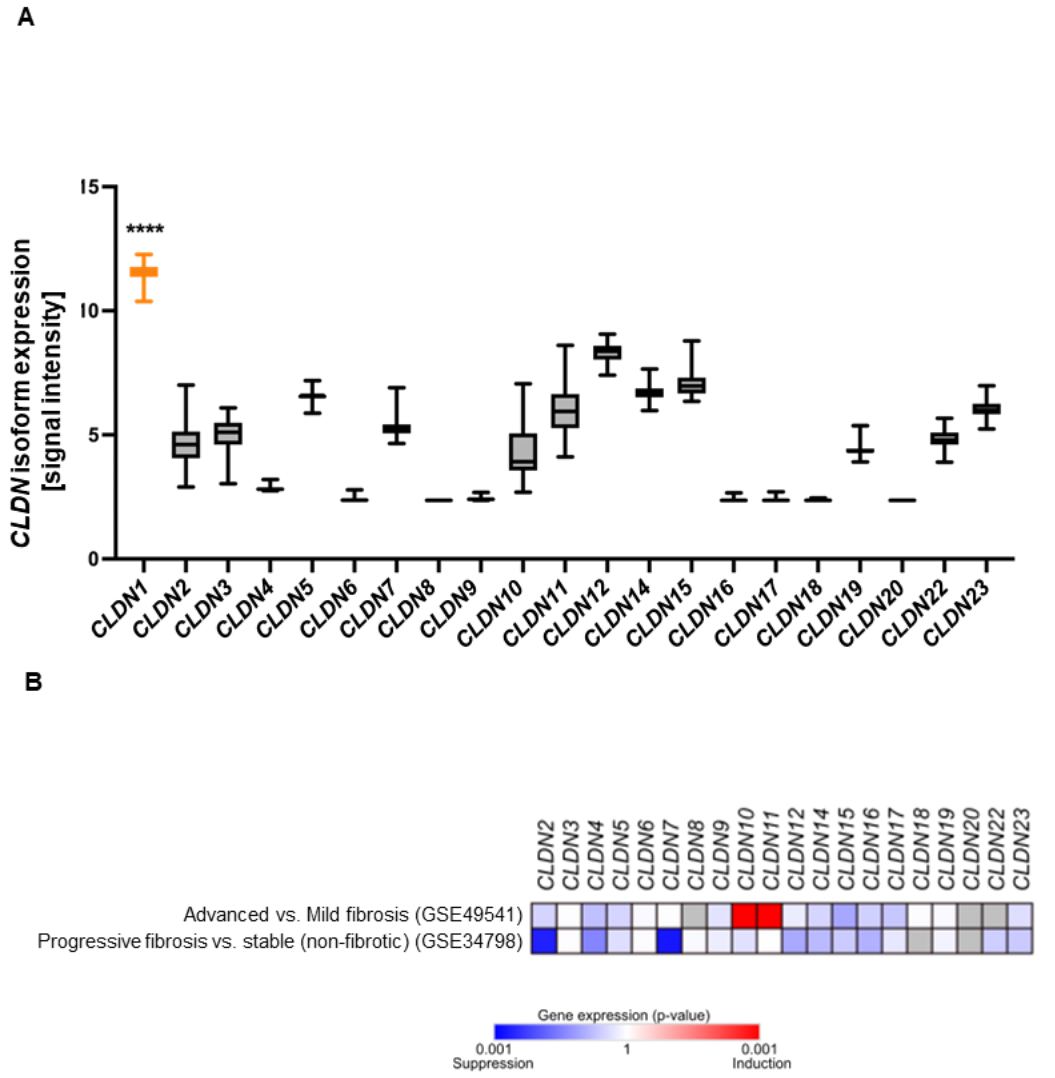

Figure S1, related to Fig. 1. Expression of different *CLDN* isoforms in the diseased liver. A. Expression in NASH fibrotic liver (GSE49541) is shown for all *CLDN* isoforms. **B.** Expression of Claudins in livers of patients with NASH with mild (F0-1) or advanced fibrosis (F3-4) (GSE49541, left panel) and liver tissues of HCV-infected patients after liver transplantation with stable or

progressive fibrotic disease (GSE34798, right panel). Heatmaps indicate significance of induction (red) or suppression (blue) compared to control tissue samples of the indicated cohorts. Grey boxes indicates that the gene is not covered in the data provided. ****p<0.0001, Kruskall-wallis test. Abbreviations: *CLDN*= Claudin.

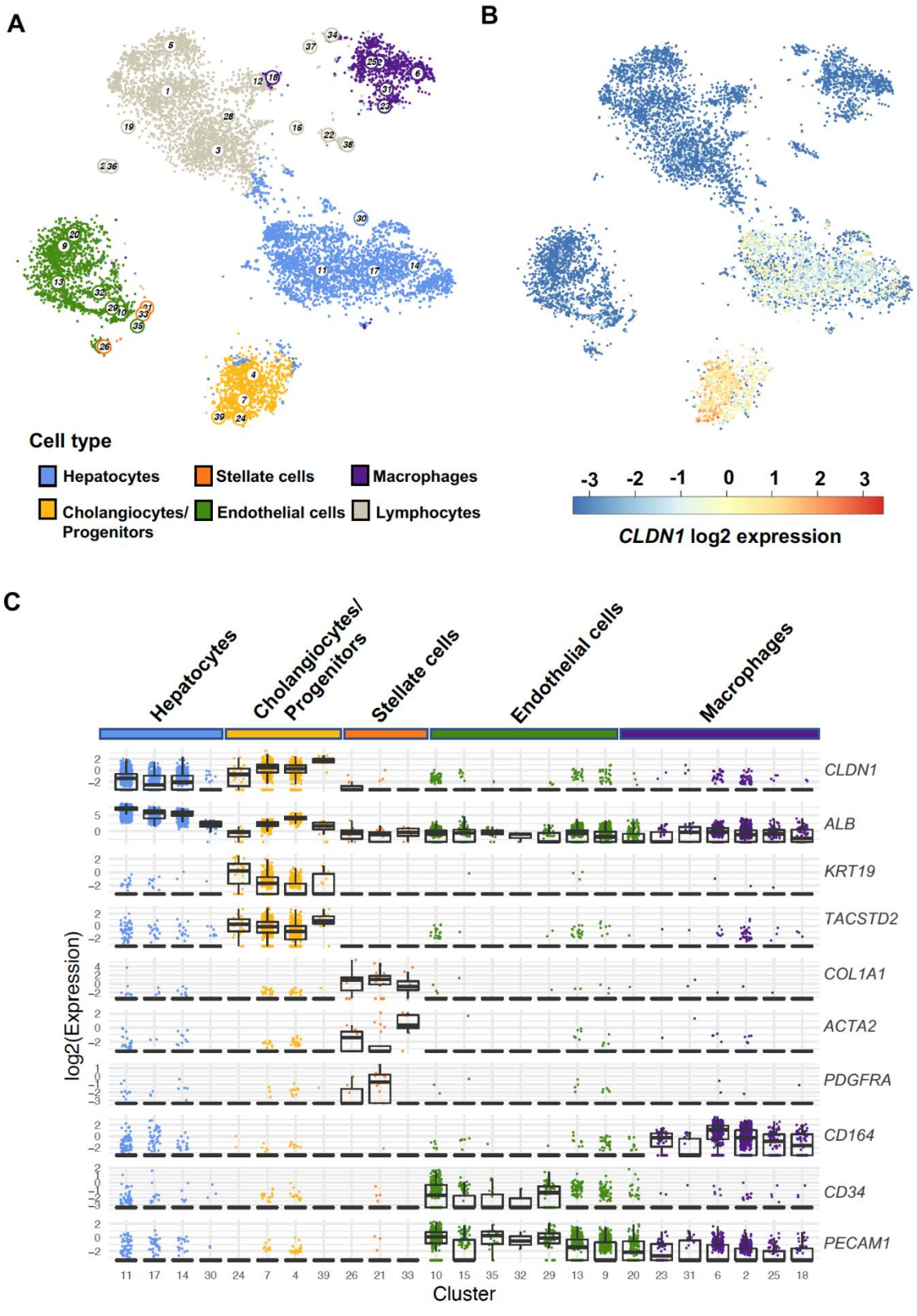
A
B
Cell type
Hepatocytes
Stellate cells
Macrophages
Cholangiocytes/ Progenitors
Endothelial cells
Lymphocytes
-3 -2 -1 0 1 2 3
CLDN1 log2 expression
C
Hepatocytes
Cholangiocytes/ Progenitors
Stellate cells
Endothelial cells
Macrophages
CLDN1
ALB
KRT19
TACSTD2
COL1A1
ACTA2
PDGFRA
CD164
CD34
PECAM1
log2(Expression)
11 17 14 30 24 7 4 39 26 21 33 10 15 35 32 29 13 9 20 23 31 6 2 25 18
Cluster

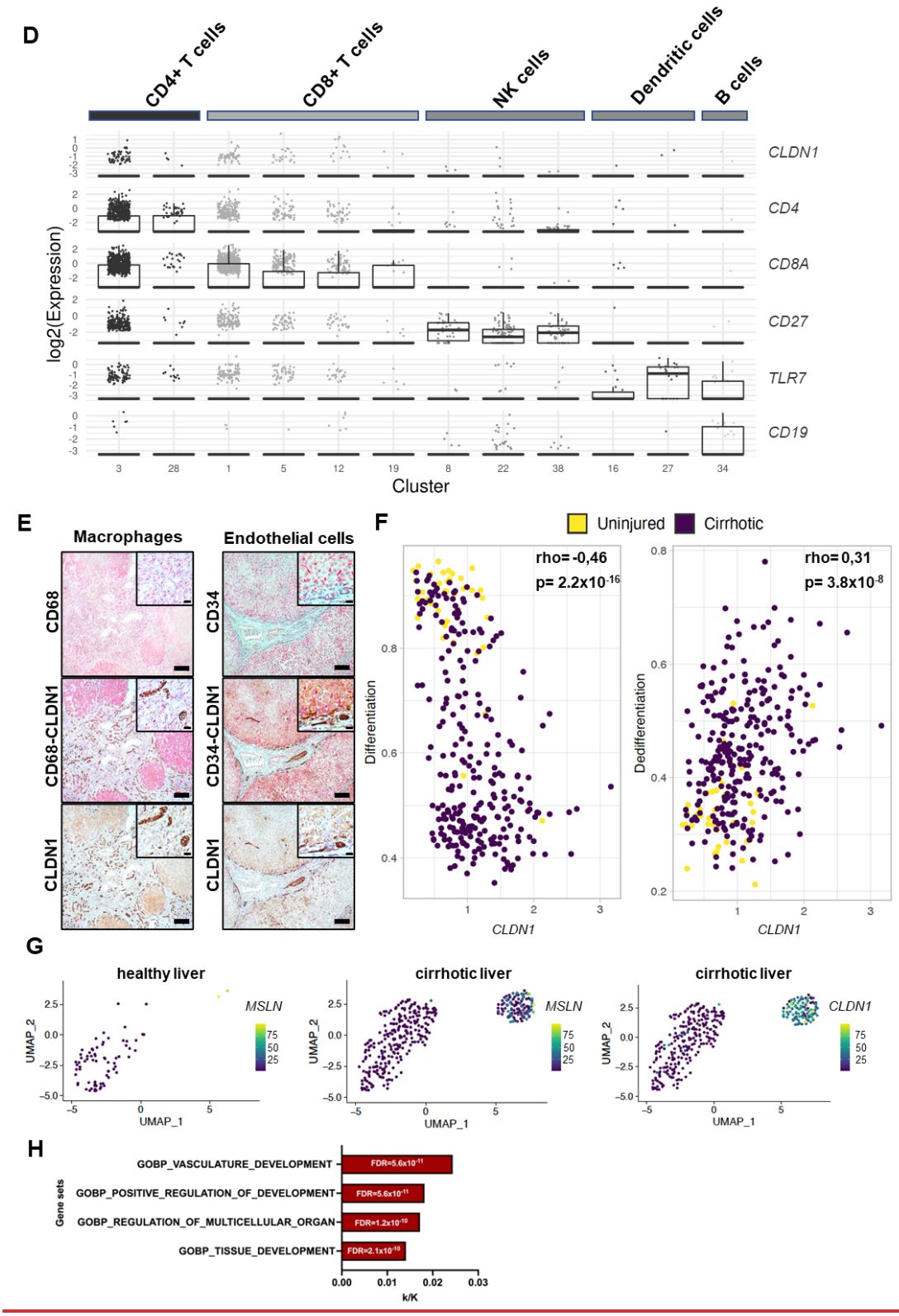
D
CD4+ T cells
CD8+ T cells
NK cells
Dendritic cells
B cells
CLDN1
CD4
CD8A
CD27
TLR7
CD19
log2(Expression)
3
28
1
5
12
19
8
22
38
16
27
34
Cluster
E
Macrophages
Endothelial cells
CD68
CD68-CLDN1
CLDN1
CD34
CD34-CLDN1
CLDN1
F
Uninjured
Cirrhotic
rho= -0,46
p= 2.2x10-16
Differentiation
CLDN1
rho= 0,31
p= 3.8x10-8
Dedifferentiation
CLDN1
G
healthy liver
cirrhotic liver
cirrhotic liver
MSLN
MSLN
CLDN1
UMAP_2
UMAP_1
H
GOBP_VASCULATURE_DEVELOPMENT
GOBP_POSITIVE_REGULATION_OF_DEVELOPMENT
GOBP_REGULATION_OF_MULTICELLULAR_ORGAN
GOBP_TISSUE_DEVELOPMENT
FDR=5.6x10-11
FDR=5.6x10-11
FDR=1.2x10-10
FDR=2.1x10-10
Gene sets
k/K

1852

Figure S2, related to Fig. 1. *CLDN1* expression in different liver cell types analyzed by scRNAseq. A. t-SNE map of the human liver cell atlas (GSE124395). **B.** *CLDN1* expression in the human liver cell atlas (GSE124395). **C.** *CLDN1* and marker gene expression in specific parenchymal and non-parenchymal cell types of the human liver (GSE124395). **D.** *CLDN1* and marker gene expression in lymphoid cells of the human liver (GSE124395). **E.** Double staining of CLDN1 and CD68 (left panel) or CD34 (right panel) by immunohistochemistry indicates absent expression of CLDN1 in endothelial cells and macrophages. Scale bars indicate 200 µm (large image) and 100 µm (small image), respectively. **F.** Negative or positive correlation of *CLDN1* expression with grade of differentiation (r= -0,46, $p<2.2 \times 10^{-16}$, gene set "AIZARANI_LIVER_C14_HEPATOCYTES_2", left panel) or de-differentiation (r= 0.31, $p=3.75 \times 10^{-8}$, gene set "AIZARANI_LIVER_C39_EPCAM_POS_BILE_DUCT_CELLS_4", right panel). The grade of differentiation or de-differentiation corresponds to the extent of enrichment of gene sets related to mature hepatocytes or *EPCAM*$^{+}$ bile duct cells(*15*) as published in MSigDB(*49*). Only cells with *CLDN1* expression covered were included. **G.** UMAPs of *Mesothelin* (*MSLN*) and *CLDN1* expression in healthy or fibrotic liver (GSE136103(*16*)) is shown. **H.** Overlap of CLDN1 co-expressed genes in human fibroblasts (E-MTAB-10324) with gene sets related to tissue development and differentiation is shown. Abbreviations: *ACTA2*= alpha smooth muscle actin; *ALB*=Albumin; CD= cluster of differentiation; *COL1A1*= Collagen 1A1; *CLDN1*= Claudin 1; *KRT19*= Keratin 19; *MSLN*= Mesothelin; NK cells= Natural Killer cells; *PDGFRA*= platelet derived growth factor receptor alpha; *TLR7*= Toll-like receptor 7.

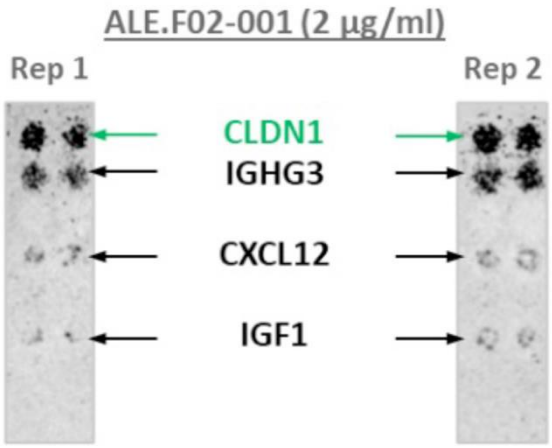

Gene Id	ALE.F02-001 interaction detected?
CLDN1	Yes
CLDN2	No
CLDN3	No
CLDN4	No
CLDN5	No
CLDN6	No
CLDN7	No
CLDN8	No
CLDN9	No
CLDN10	No
CLDN11	No
CLDN12	No
CLDN14	No
CLDN15	No
CLDN16	No
CLDN17	No
CLDN18	No
CLDN19	No
CLDN20	No
CLDN22	No
CLDN23	No
CLDN24	No
CLDN25	No
CLDN34	No

Figure S3, related to Fig. 1. CLDN1 mAbs are highly specific for human CLDN1. Interaction of CLDN1 mAbs (representatively shown for ALE.F02) with human plasma membrane and secreted proteins, as assessed by Retrogenix assay is shown. A strong positive signal was only detected for hCLDN1 and the IgG heavy chain. No cross-reactivity was found for >5000 other proteins tested. Minor non-specific interactions were found for CXCL12 and IGF1. Abbreviations: CLDN=Claudin; CXCL12=C-X-C Motif Chemokine Ligand 12; IGHG3=Immunoglobulin Heavy Constant Gamma 3; IGF=Insulin like growth factor 1; Rep=Replicate.

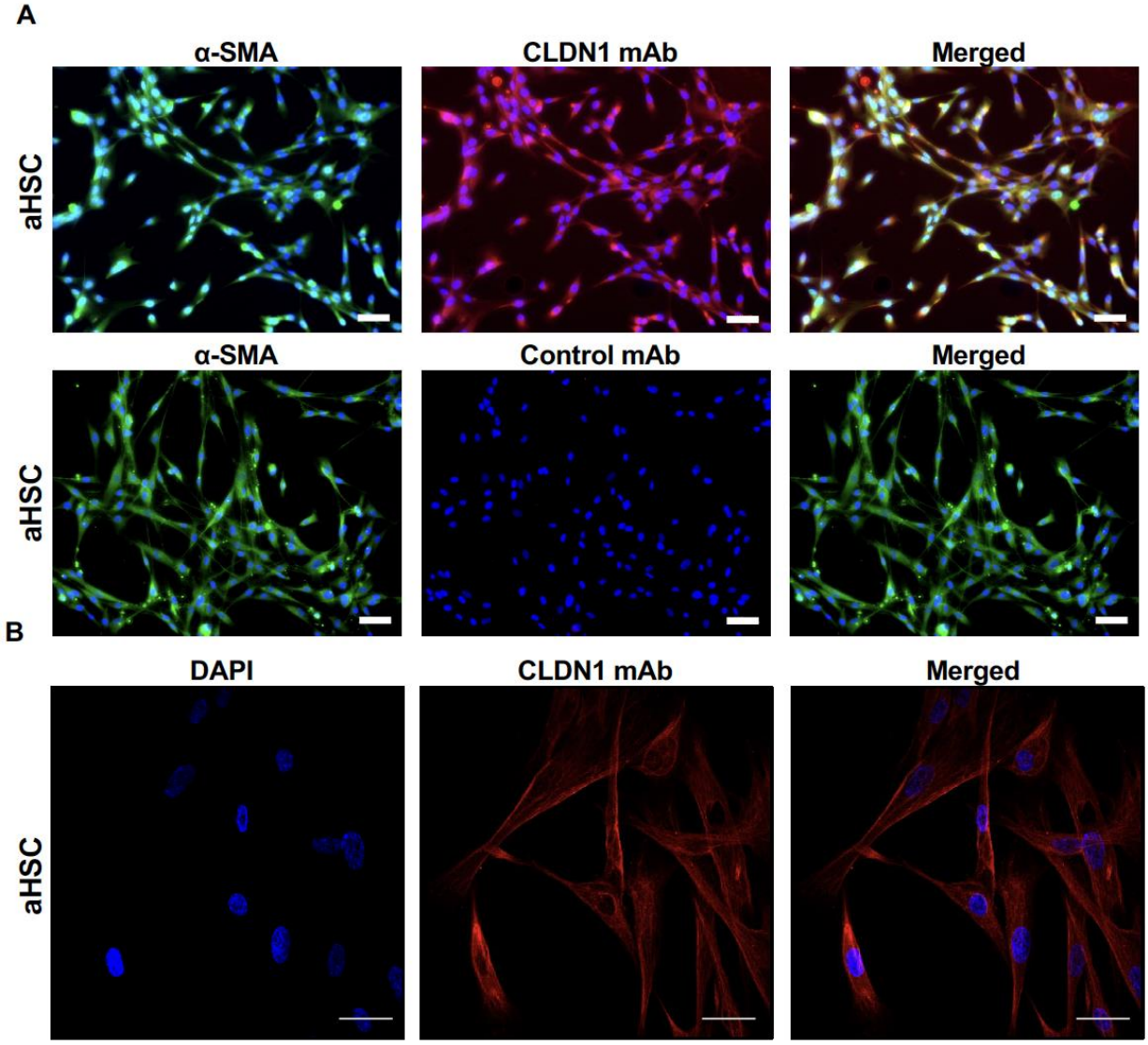

Figure S4, related to Fig. 1. Non-junctional CLDN1 expression in activated stellate cells. A. Representative images of CLDN1 mAb H3L3 binding to patient derived HLMFs, as assessed by immunofluorescence. Scale bars indicate 100 μm. **B.** Representative confocal microscopic images CLDN1 mAb H3L3 binding to patient derived HLMFs. Scale bars indicate 100 μm. Abbreviations: α-SMA= alpha smooth muscle actin; CLDN1= Claudin 1; aHSC= activated Hepatic stellate cells.

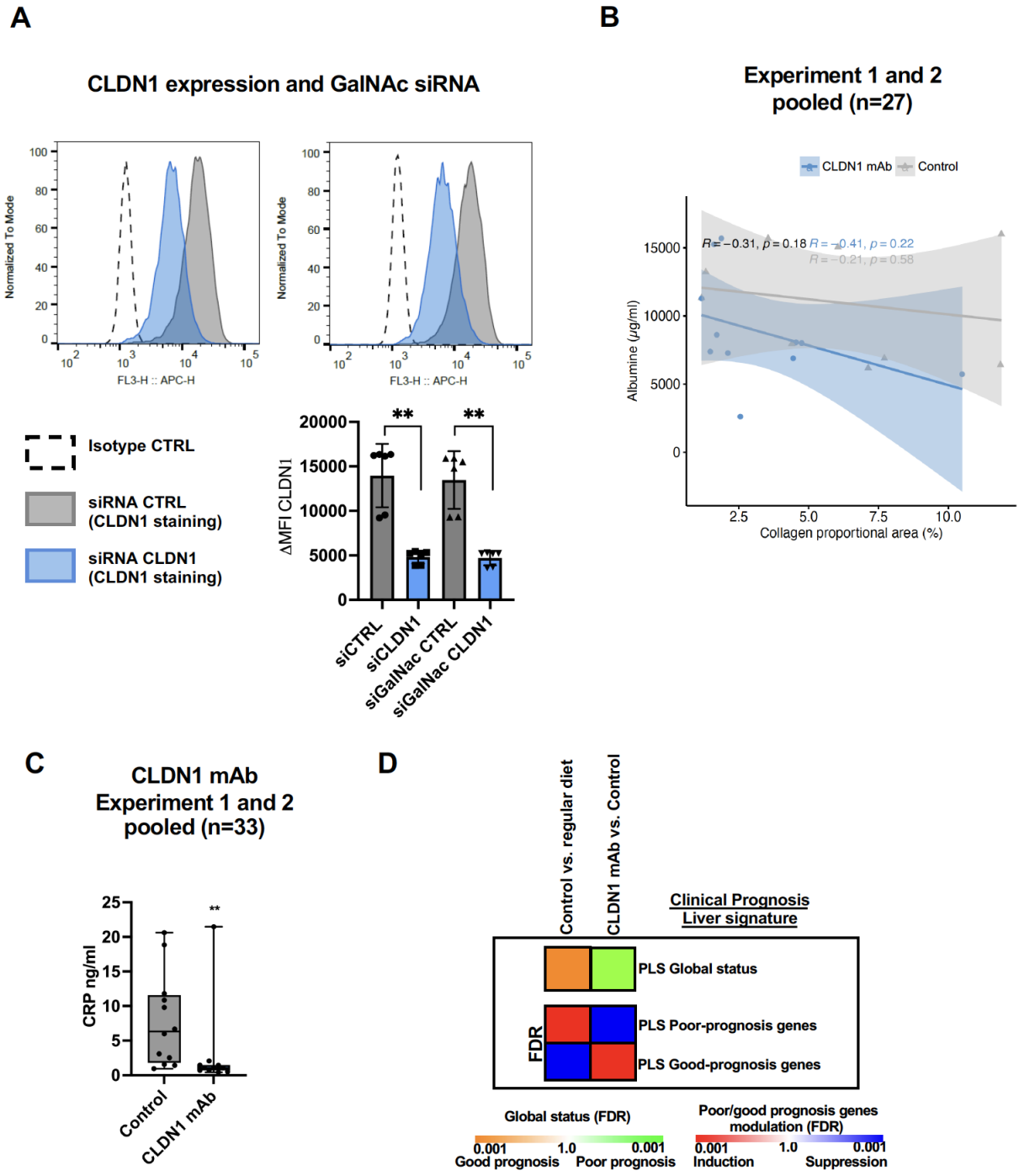

Figure S5 related to Fig. 2. Validation of cell surface CLDN1 knockdown by GalNAc siRNA in Huh7 liver cells. A. Effect of GalNAc siRNA mediated suppression of CLDN1 expression and validation in Huh7 cells. CLDN1 protein expression following siCLDN1 or

GalNAc-siCLDN1 mediated knockdown in Huh7 cells was assessed by flow cytometry (n=2 independent experiments with n=3 biological replicates per condition). Graphs shows ΔMFI of CLDN1 mAb compared to Control mAb binding to the respective cells. ** p<0.01, U-test. **B.** Humanization and fibrosis in humanized liver fibrosis mice. Similar baseline levels of human albumin in both treatment groups and absent correlation of humanization with observed antifibrotic effects (total collagen proportional area) is shown. **C.** Effect of CLDN1 mAb treatment on serum C-reactive protein. Significant reduction of plasma CRP levels in CLDN1 mAb treated mice compared to control. Pooled data of experiments 1 and 2 are shown, control *n*=12, CLDN1 mAb *n*=11. ** p<0.01, KW test. **D.** Modulation of PLS to good (green) or poor (orange) prognosis status(*25*)in liver tissues of humanized NASH fibrosis mice treated with CLDN1 mAb or control. The significance (FDR, Kolmogorov-Smirnov test) of induction (red) or suppression (blue) of PLS poor- or good-prognosis genes is illustrated below. Abbreviations: CLDN1= Claudin 1; CRP= C-reactive protein; FDR= False discovery rate; PLS= prognostic liver signature.

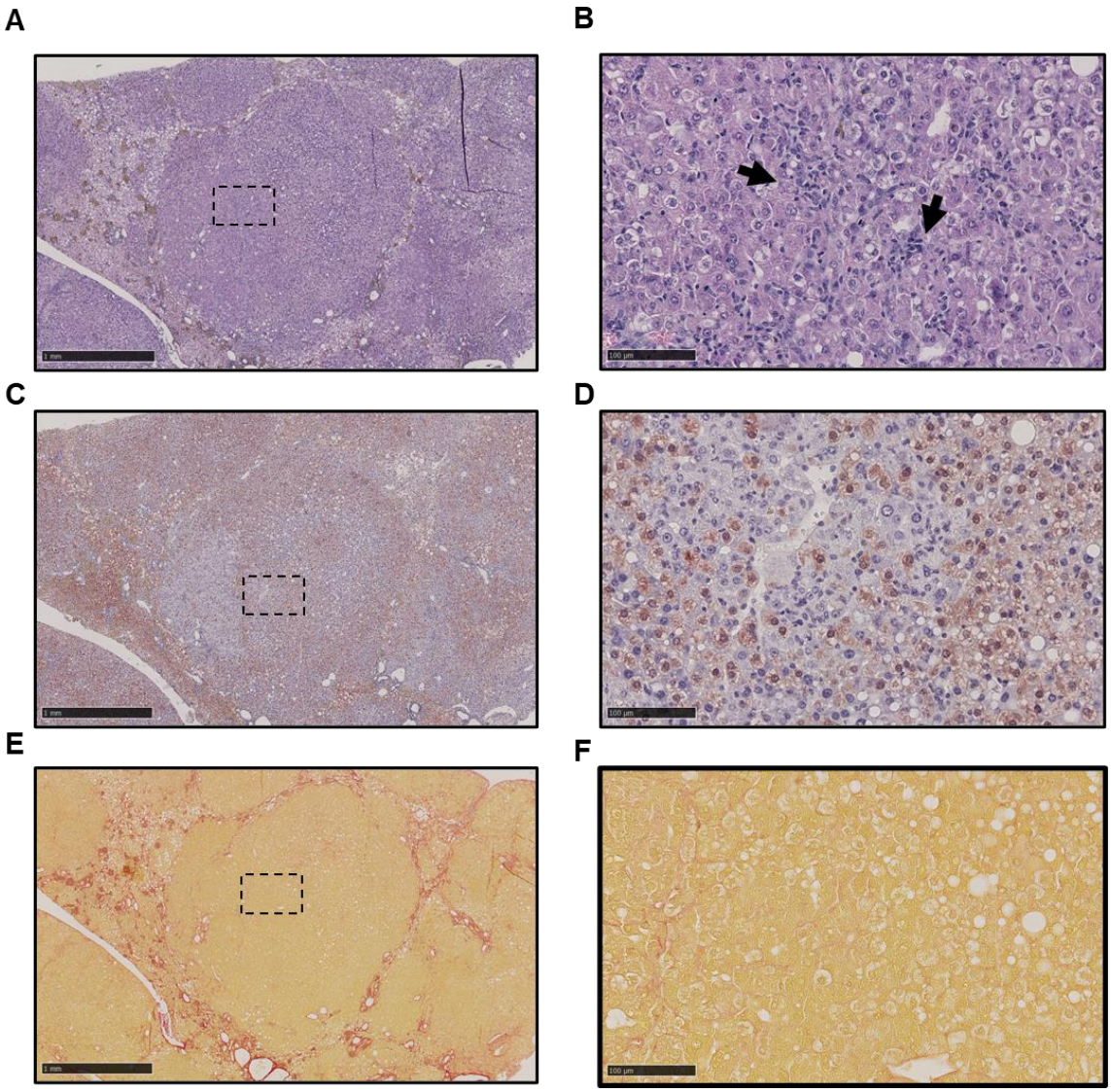

Figure S6, related to Fig. 2. Human liver chimeric mice fed with CDA-HFD diet show expansive regenerative nodules of hepatocytes with reactive ductules consisting of mouse and human hepatocytes. A-B. H&E staining at low (A) and high (B) magnification showing an expansive nodule consisting of nodular growing mouse hepatocytes (negative for FAH see C and D), reactive ductules (arrow) and human hepatocytes (positive for FAH see C and D). **C-D.** Human hepatocytes identified by FAH staining in the chimeric liver are shown at low (A) and high (B)

magnification. **E-F.** Sirius Red staining at low (A) and high (B) magnification showing less fibrosis in the nodule suggesting a higher proliferation rate of cells in nodules compared to the surrounding liver. Scale bar in A, C and E =1 mm. Scale bar in B, D and F=100 µm. Rectangles in the left panels correspond to the area illustrated in the right panels. Abbreviations: CDA-HFD = choline-deficient, L-amino acid-defined, high fat diet.

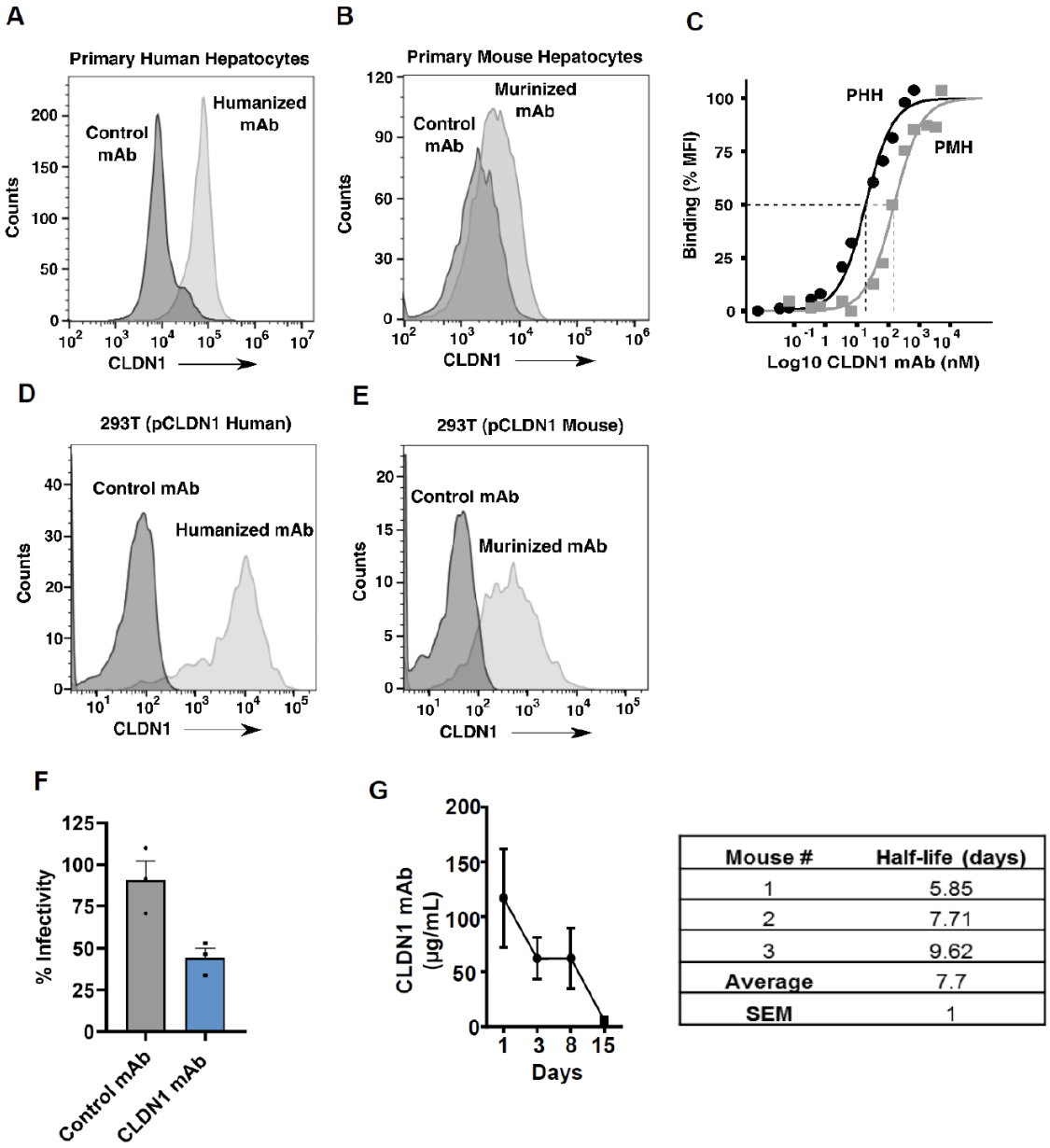

Mouse #	Half-life (days)
1	5.85
2	7.71
3	9.62
Average	7.7
SEM	1

Figure S7, related to Fig. 3. Functional assessment and pharmacokinetics of the murinized and humanized anti-human CLDN1-specific mAb. A-B. Binding of humanized anti-CLDN1 mAb H3L3 or murinized CLDN1 mAb to CLDN1 expressed on primary human (PHH) (A) or mouse hepatocytes (PMH) (B) as assessed by flow cytometry is shown **C.** The binding kinetics of the interaction between humanized or murinized mAb against human or mouse

CLDN1 expressed on PHH and PMH were determined by applying the Michaelis-Menten mathematical model (PHH: black, apparent Kd of ≈ 19 nM; PMH: grey, apparent Kd of ≈ 154 nM), respectively. **D-E.** The humanized and murinized CLDN1 mAb show robust binding to 293T cells, engineered to express human or murine CLDN1 (mCLDN1), respectively. **F.** mCLDN1 expressing 293T cells were incubated with a murinized CLDN1 mAb (100 µg/mL) for 1 h at 37 °C prior to incubation with HCV pseudoparticles bearing glycoproteins JHF1 genotype 2a of HCV. HCVpp entry into 293T cells was assessed by measuring luciferase activity after 72 h and is shown as percentage relative to entry into untreated cells. *$p<0.05$, Student's t-test. **G.** Left panel: Serum concentrations of the murinized CLDN1 mAb were determined at the indicated time points after a single i.p. injection of 500 µg (25 mg/kg) of murinized mAb into three C3H mice. Right panel: The half-life of the murinized CLDN1-specific is shown, as determined using regression curve analyses. Results in A-E are representative for at least 3 independent experiments with biological duplicates per condition. Abbreviations: SEM=standard error of the mean; PHH=primary human hepatocytes; PMH=primary mouse hepatocytes.

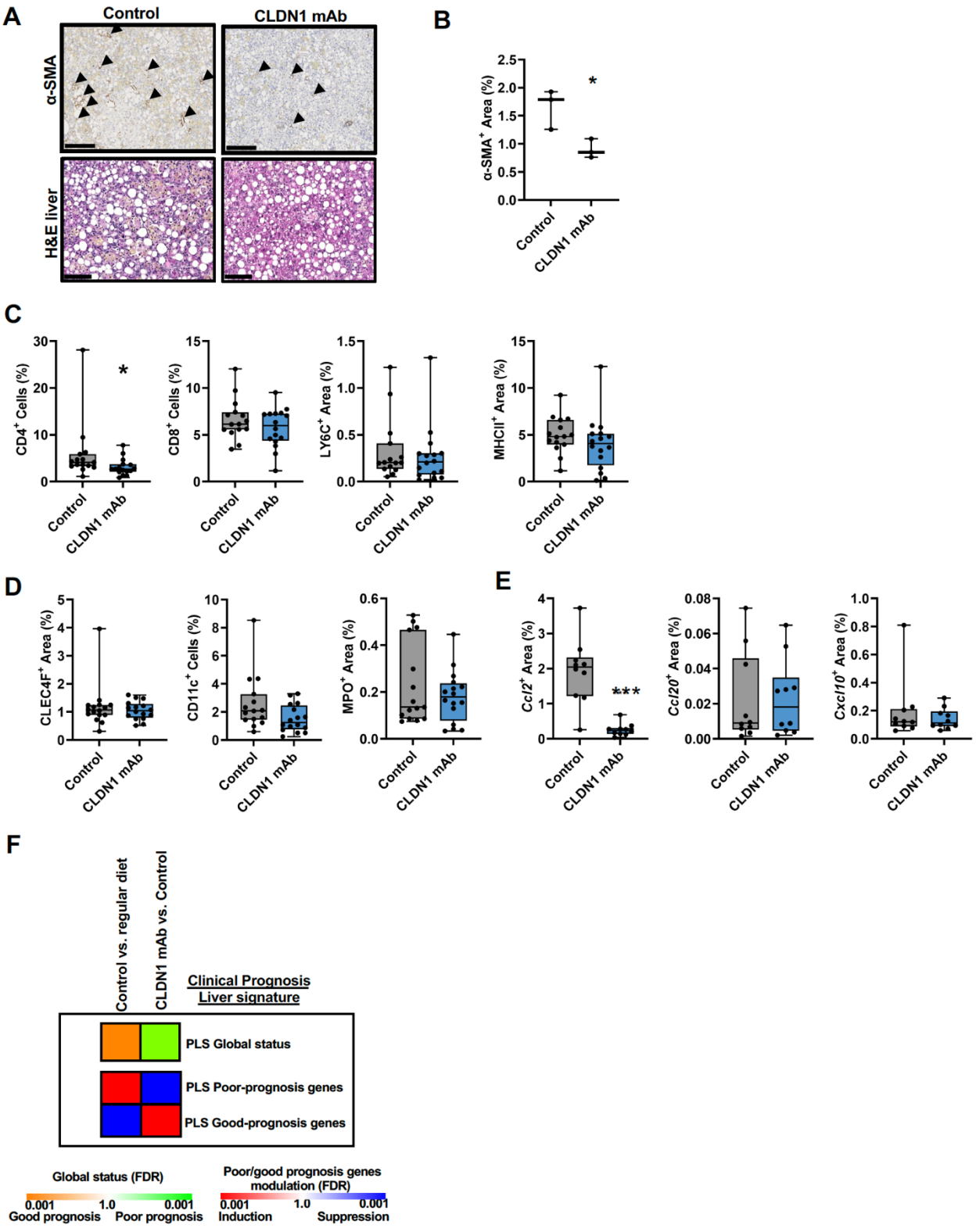
A
Control
CLDN1 mAb
α-SMA
H&E liver
B
α-SMA+ Area (%)
Control
CLDN1 mAb
C
CD4+ Cells (%)
CD8+ Cells (%)
LY6C+ Area (%)
MHCII+ Area (%)
D
CLEC4F+ Area (%)
CD11c+ Cells (%)
MPO+ Area (%)
E
Ccl2+ Area (%)
Ccl20+ Area (%)
Cxcl10+ Area (%)
F
Control vs. regular diet
CLDN1 mAb vs. Control
Clinical Prognosis
Liver signature
PLS Global status
PLS Poor-prognosis genes
PLS Good-prognosis genes
Global status (FDR)
Good prognosis
Poor prognosis
Poor/good prognosis genes modulation (FDR)
Induction
Suppression

1953

Figure S8, related to Fig. 3. Analyses of liver inflammatory changes and effects on the prognostic liver signature (PLS) following CLDN1 mAb treatment in DEN-CDAHFD mice. A. Representative histological images of myofibroblast activation (upper panel) and steatosis (bottom panel) in mouse livers. **B.** Quantitative assessment of α-SMA proportional areas in treatment groups. **C.** Immunostaining shows significant suppression of CD4+ T cell infiltration in murine livers of mice treated with CLDN1 mAb (p=0.02, U-test, left panel). No effect was observed on presence of CD8+ T cells, $LY6C^+$ macrophages and $MHCII^+$ antigen presenting cells. **D.** Immunostaining did not reveal any significant changes in the quantity of $CLEC4F^+$ Kupffer cells, $CD11c^+$ dendritic cells and MPO^+ neutrophils in CLDN1 mAb versus control treated mice. **E.** Cytokine in situ hybridization reveals significant suppression of *Ccl2* expression in CLDN1 mAb treated DEN-CDAHFD mice (p=0.0003, U-test, left panel), but no effect of *Ccl20* and *Cxcl10*. **F.** Modulation of PLS to good (green) or poor (orange) prognosis status(*25*) in liver tissues of DEN-CDAHFD mice treated with CLDN1 mAb or control. The significance (FDR, Kolmogorov-Smirnov test) of induction (red) or suppression (blue) of PLS poor- or good-prognosis genes is illustrated below. Abbreviations: α-SMA= alpha smooth muscle actin; *Ccl2*= chemokine ligand 2; *Ccl20*= chemokine ligand 20; CD= Cluster of differentiation; CLDN1= Claudin 1; *Cxcl10*= C-X-C motif chemokine 10; CLEC4F= C-Type Lectin Domain Family 4 Member F; FDR= False discovery rate; H&E= Hematoxylin and eosin; LY6C= lymphocyte antigen 6 complex, locus C; MHCII= major histocompatibility complex II; PLS= Prognostic liver signature.

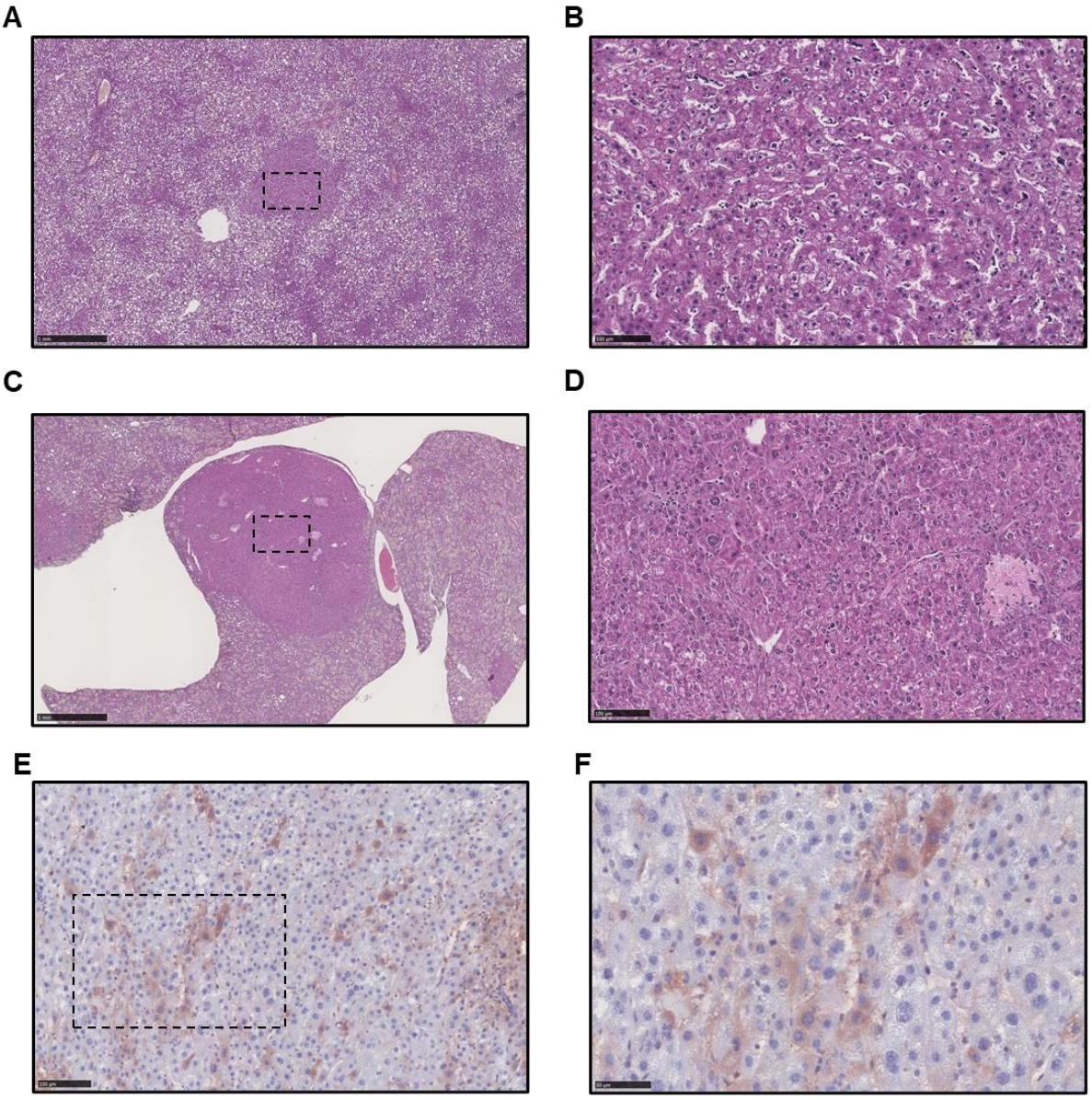

Figure S9, related to Fig. 3. DEN-CDAHFD mice develop nodules consisting of HCC and preneoplastic lesions. A-B. Example of a preneoplastic lesion at low (A) and high (B) magnification. H&E staining shows an irregular nodule with more compact growth pattern and conserved 1-cell thick liver cell plates. Portal tracts are missing in the nodule. **C-D**. Example of HCC nodule at low (A) and high (B) magnification. H&E staining shows an expansive nodule

with compact growth pattern with thickened liver cell plates, anisokaryosis of hepatocytes and the absence of portal tracts. **E-F.** Example of HCC nodule positive for HSP70 by immunohistochemistry at low (E) and high magnification (F). Scale bar in A and C=1 mm. Scale bar in B, D and E=100 µm. Scale bar in F=50 µm. Rectangles in the left panels correspond to the area illustrated in the right panels.

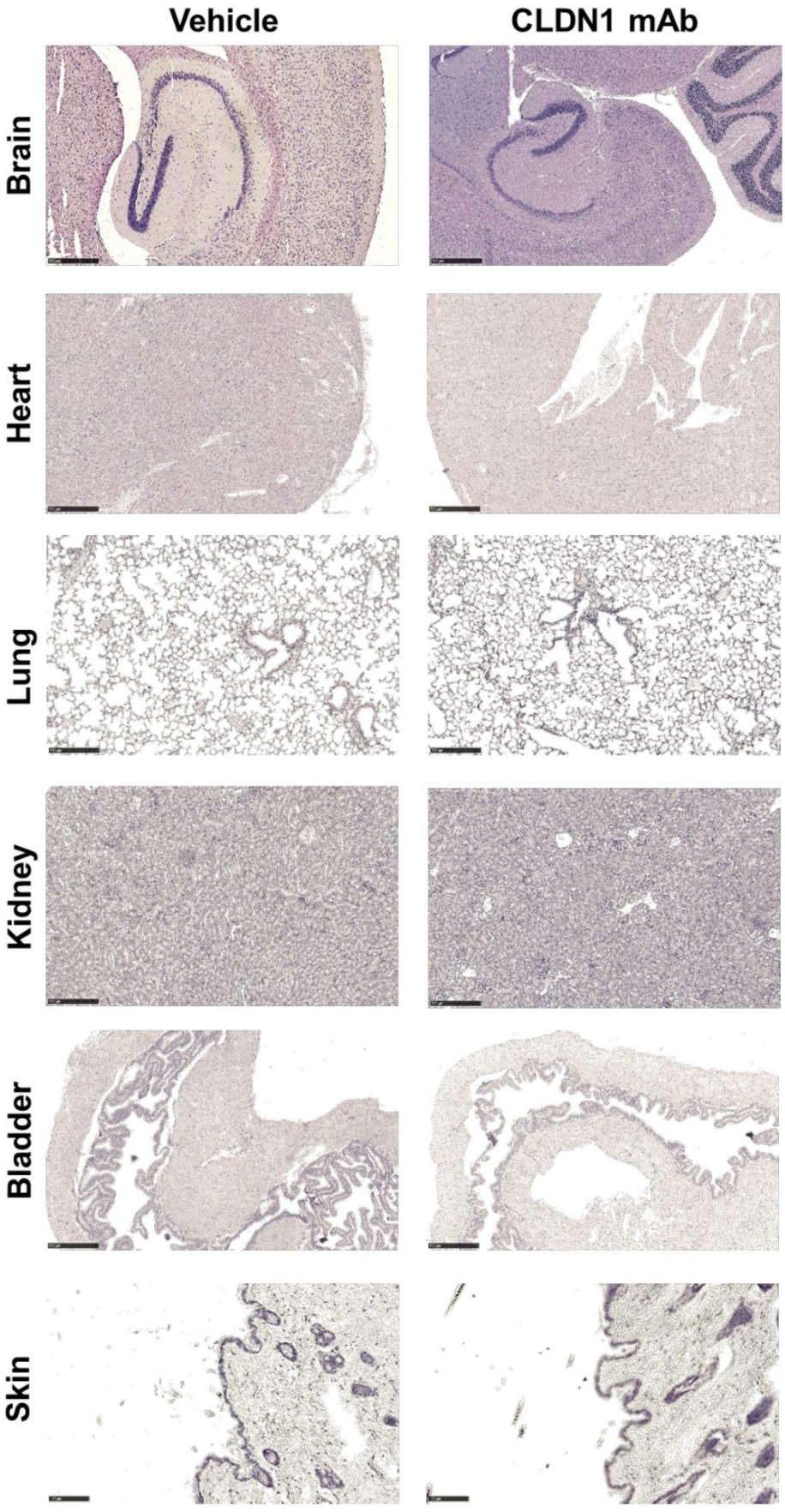
Vehicle
CLDN1 mAb
Brain
Heart
Lung
Kidney
Bladder
Skin

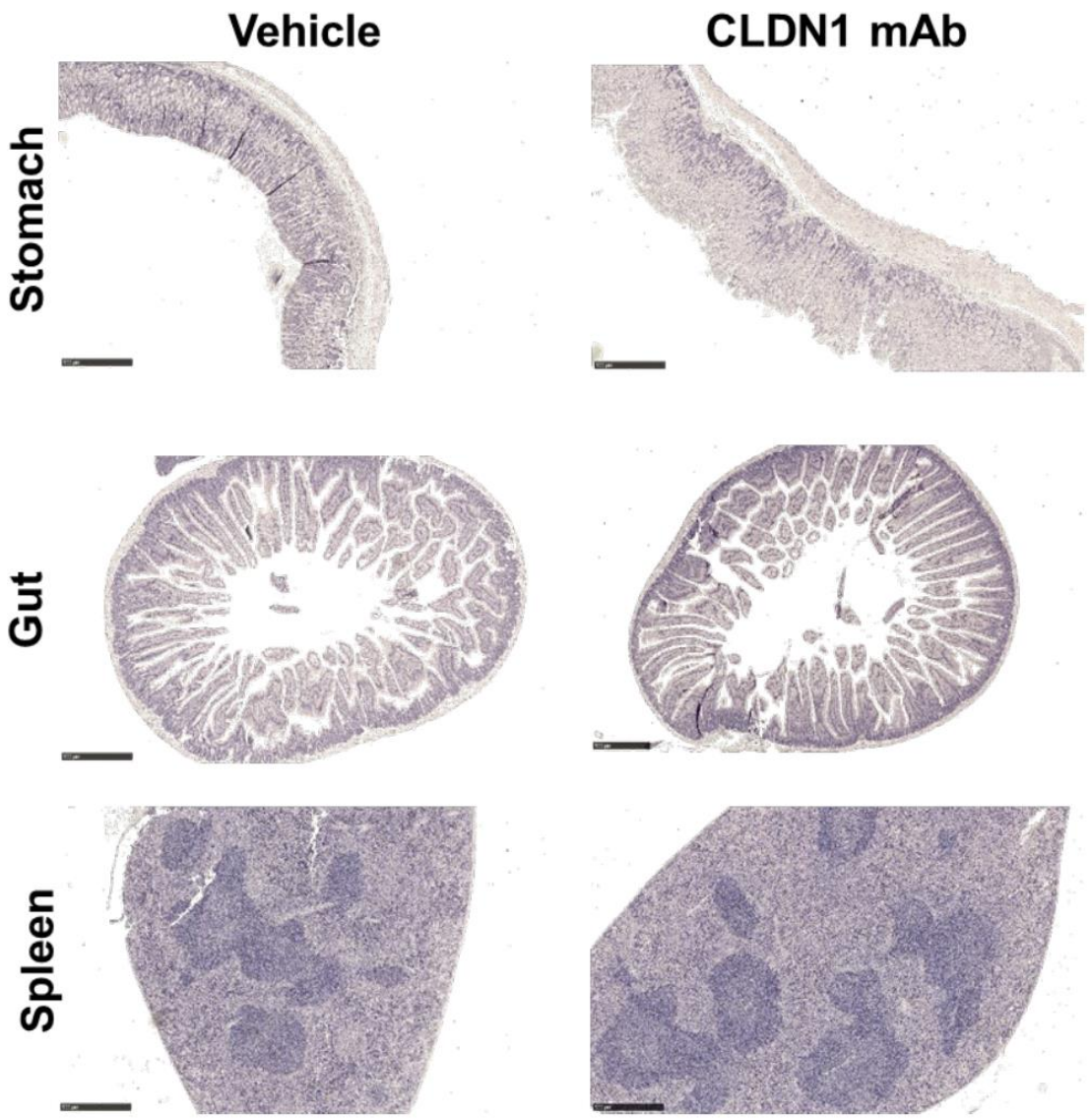

Figure S10, related to Fig 3. Histopathology of organs in DEN-CDA-HFD mouse model treated with CLDN1-specific mAb or vehicle control for 16 weeks. All the organs were fixed in formalin, embedded in paraffin, stained by hematoxylin and eosin and analyzed by an expert veterinary pathologist from Phemonin-ICS, Illkirch, France. One-hundred-twenty-eight

histological slides were analyzed. Eosin was weak on some sections (as shown in the brain image of the vehicle control group) without affecting the quality of the analysis.

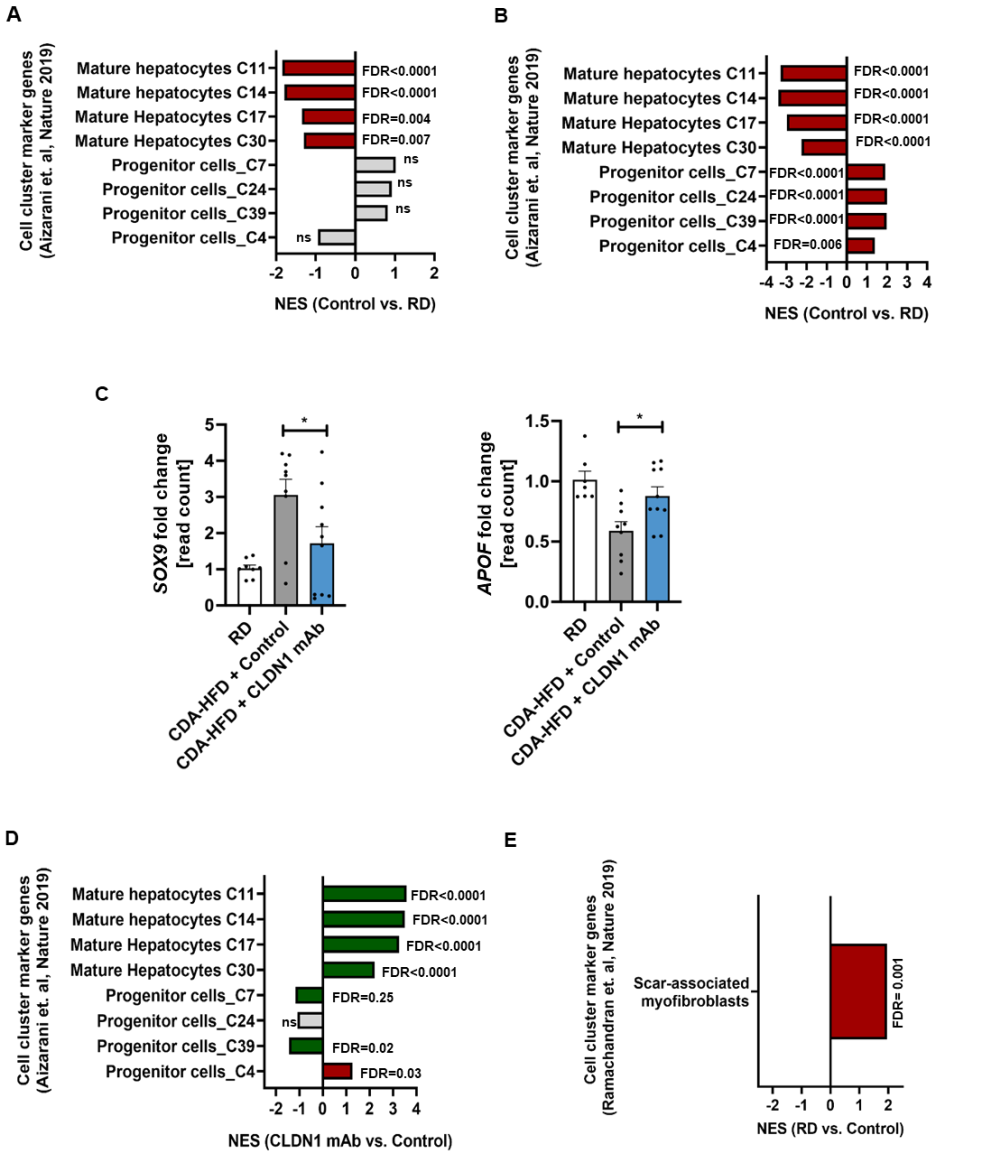

Figure S11, related to Fig. 5. CLDN1 mAb affects cell plasticity *in vivo* and in cell-based model systems. A-B. Differential expression of gene sets characterizing mature hepatocytes ((*15*) and MSigDB: AIZARANI_LIVER_C11/C14/C17C30_HEPATOCYTES) and immature progenitor cells ((*15*) and

MSigDB:AIZARANI_LIVER_C4/C7/C24/C39_EPCAM_POS_BILE_DUCT_CELLS) in healthy (RD) versus fibrotic livers in the humanized (**A**) and classical NASH fibrosis mouse model (**B**) is shown. **C.** Effect of CLDN1 mAb on progenitor/stem cell marker *SOX9* or *Sox9* and mature hepatocyte marker *APOF* or *Apof* in humanized and DEN-CDA-HFD mice respectively (pooled data, humanized mice: RD, n=3; CDA-HFD+Control, n=3, CDA-HFD+ CLDN1 mAb, n=4; DEN-CDA-HFD mice: RD, n=5, CDA-HFD+Control, n=6, CDA-HFD+ CLDN1 mAb, n=6, p=0.05 and p=0.04, U-test, respectively). **D.** Effect of CLDN1 mAb on hepatocyte de-differentiation in NASH fibrosis mice. **E.** Modulation of gene sets characterizing scar-associated myofibroblasts (**table S9**) in healthy (RD) versus fibrotic livers in the classical NASH fibrosis mouse model. Colored horizontal bars indicate NES of significantly (FDR<0.25, Kolmogorov-Smirnov test, respectively) altered gene sets**.** Vertical bars show mean ± SEM. *p<0.05, t-test, respectively. Abbreviations: CLDN1= Claudin 1; FDR= False discovery rate; NASH= Non-alcoholic steatohepatitis; RD= Regular diet; NES= Normalized enrichment score.

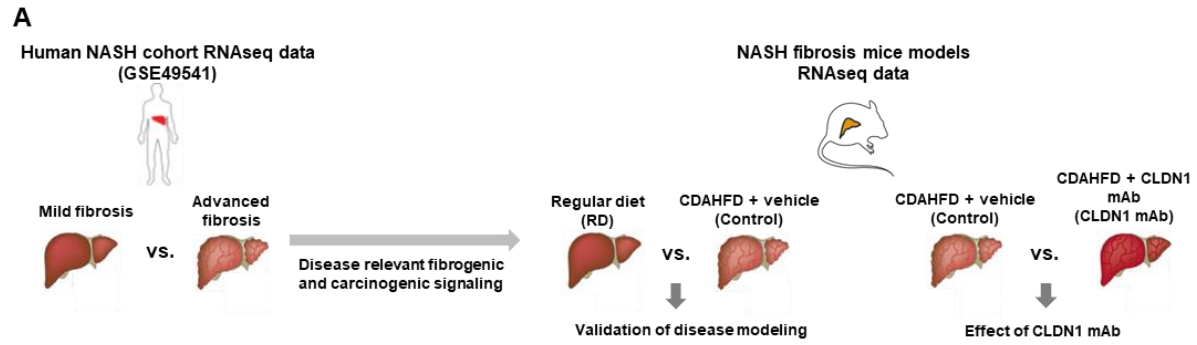
A
Human NASH cohort RNAseq data
(GSE49541)
Mild fibrosis
vs.
Advanced fibrosis
Disease relevant fibrogenic
and carcinogenic signaling
NASH fibrosis mice models
RNAseq data
Regular diet
(RD)
vs.
CDAHFD + vehicle
(Control)
Validation of disease modeling
CDAHFD + vehicle
(Control)
vs.
CDAHFD + CLDN1
mAb
(CLDN1 mAb)
Effect of CLDN1 mAb

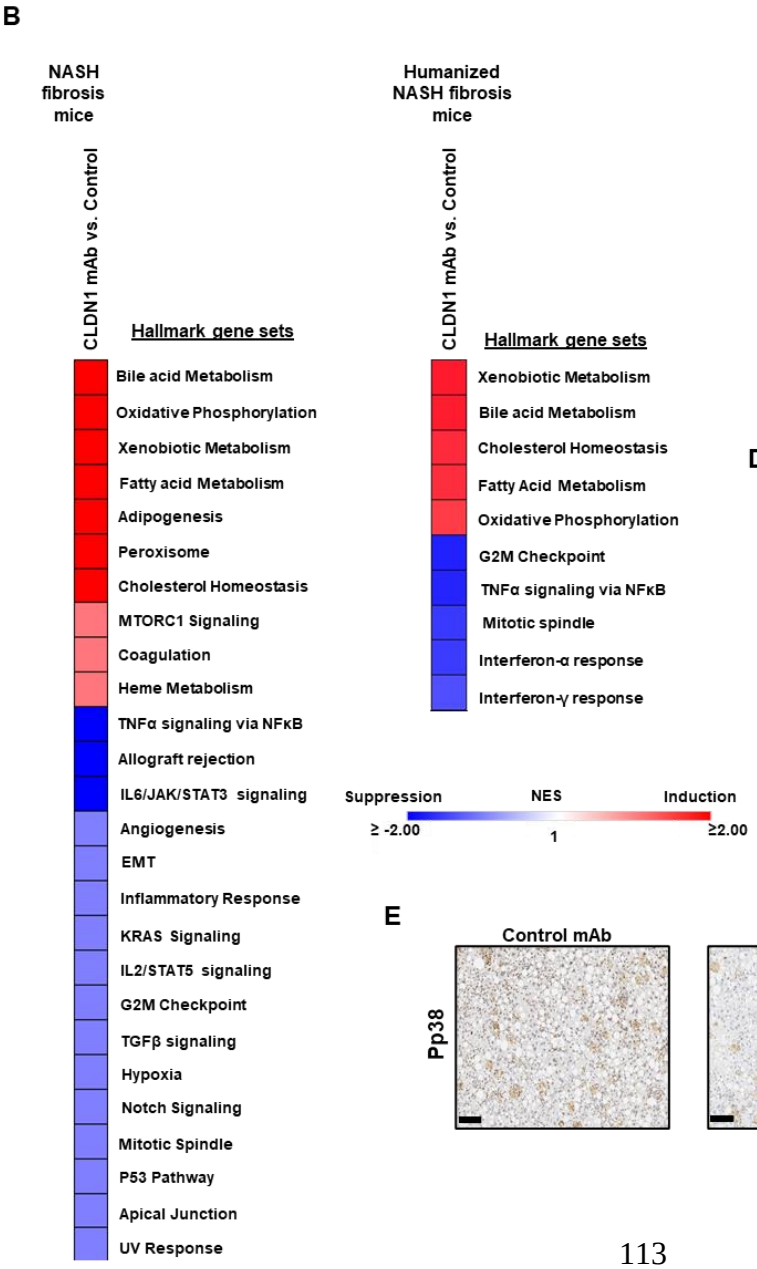
B
NASH
fibrosis
mice
CLDN1 mAb vs. Control
Hallmark gene sets
Bile acid Metabolism
Oxidative Phosphorylation
Xenobiotic Metabolism
Fatty acid Metabolism
Adipogenesis
Peroxisome
Cholesterol Homeostasis
MTORC1 Signaling
Coagulation
Heme Metabolism
TNFα signaling via NFκB
Allograft rejection
IL6/JAK/STAT3 signaling
Angiogenesis
EMT
Inflammatory Response
KRAS Signaling
IL2/STAT5 signaling
G2M Checkpoint
TGFβ signaling
Hypoxia
Notch Signaling
Mitotic Spindle
P53 Pathway
Apical Junction
UV Response
Humanized
NASH fibrosis
mice
CLDN1 mAb vs. Control
Hallmark gene sets
Xenobiotic Metabolism
Bile acid Metabolism
Cholesterol Homeostasis
Fatty Acid Metabolism
Oxidative Phosphorylation
G2M Checkpoint
TNFα signaling via NFκB
Mitotic spindle
Interferon-α response
Interferon-γ response
Suppression
NES
Induction
≥ -2.00
1
≥2.00

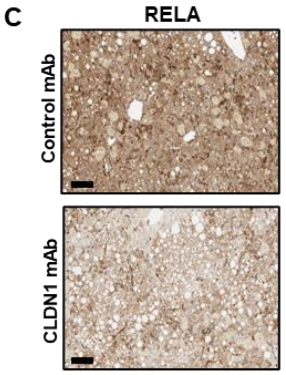
C
RELA
Control mAb
CLDN1 mAb

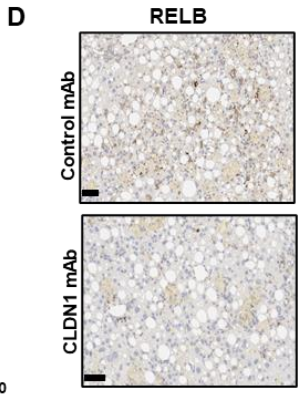
D
RELB
Control mAb
CLDN1 mAb

E
Control mAb
CLDN1 mAb
Pp38

Figure S12, related to Fig. 5. CLDN1 mAb affects cell signaling *in vivo*. A. Graphical illustration of methodological approach to assess fibrosis associated signaling in NASH mouse models. **B.** Unbiased assessment of Hallmark gene sets by GSEA in two NASH fibrosis mouse models. Heatmaps indicate NES of significantly (FDR <0.05) altered gene sets. **C-E.** Representative immunohistochemistry of RELA, RELB and phospho-p38 in CLDN1 or Control mAb treated NASH fibrosis mice.

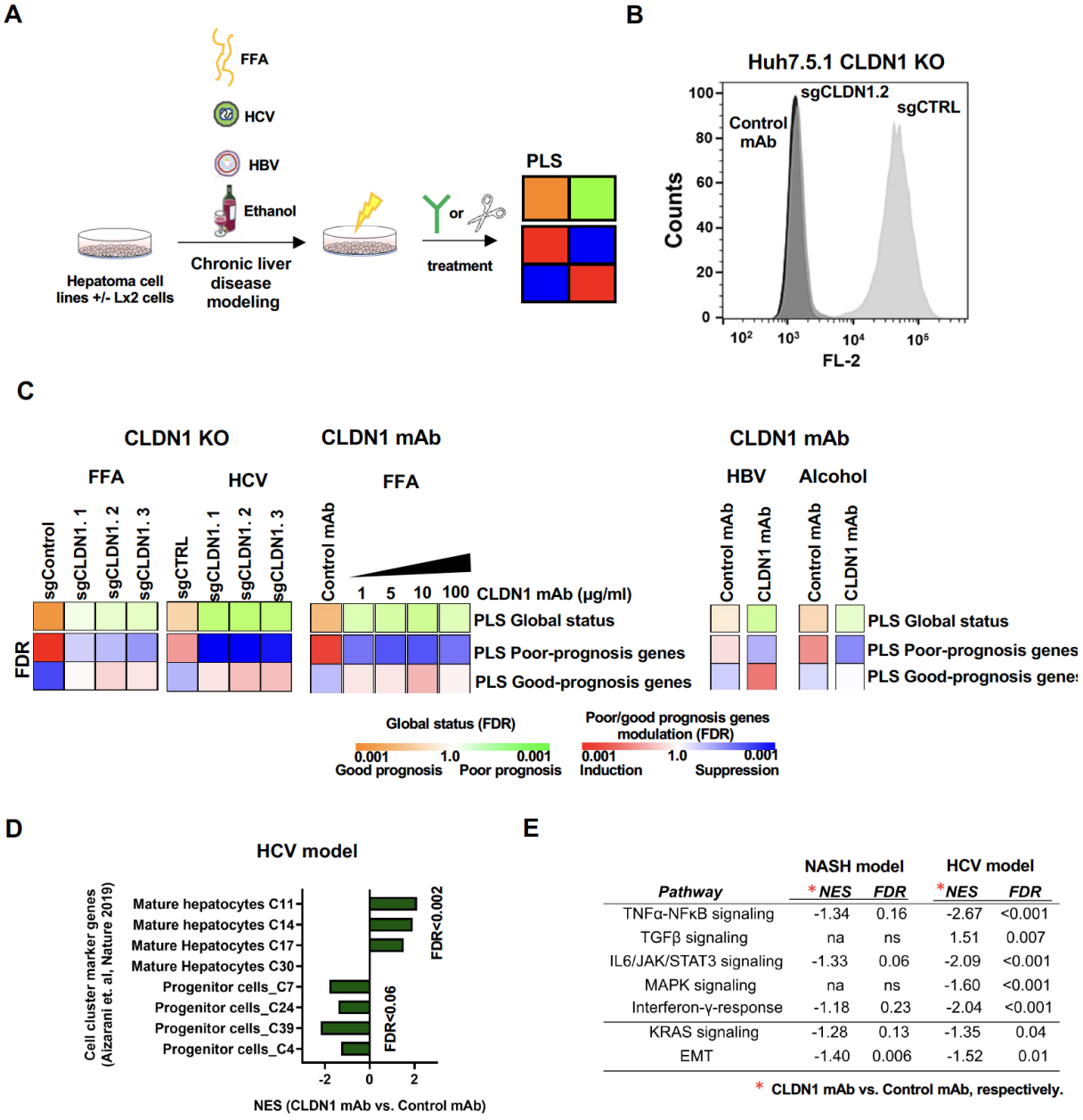

Figure S13, related to Fig. 5. CLDN1 mAb affects cell circuits relevant for patient prognosis in cell-based model systems. A. Graphical illustration of PLS assessment in *in vitro* models of all major etiologies of chronic liver disease. **B.** Absent binding of humanized CLDN1

mAb to *Huh7.5.1-Cas9 cells* expressing single guide RNAs (sgRNAs), assessed by flow cytometry is shown. **C.** Modulation of PLS to good (green) or poor (orange) prognosis status in sgCLDN1 or sgCTRL transfected- as well as CLDN1 mAb or control mAb-treated *in vitro* models of NASH, alcoholic liver disease, HBV and HCV infection compared to Mock cells. The significance (FDR, Kolmogorov-Smirnov test) of induction (red) or suppression (blue) of PLS poor- or good-prognosis genes is illustrated below. **D.** Modulation of liver progenitor and mature hepatocyte related gene sets in Huh7.5.1^{dif} infected with HCV and treated with CLDN1 mAb or control mAb. **E.** Modulation of fibrosis- and carcinogenesis-associated signaling pathways by CLDN1 mAb in the HCV and NASH *in vitro* model. Abbreviations: HBV= Hepatitis B Virus; HCV= Hepatitis C virus; EMT= epithelial-mesenchymal transition; FDR= False discovery rate; FFA= Free fatty acids; KO= Knockout; NES= Normalized enrichment score; PLS= Prognostic Liver Signature; SEM= Standard error of the mean; sg= single guides.

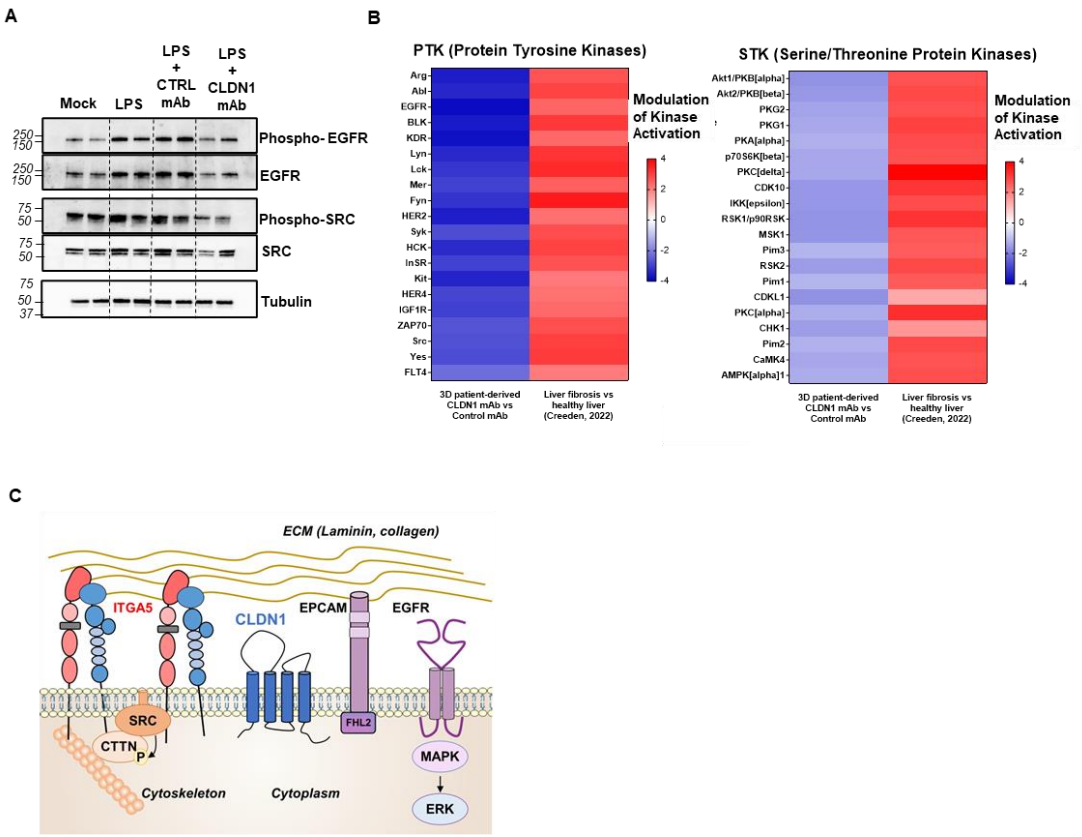

Figure S14, related to Fig. 5-6. CLDN1 mAb modulates membrane receptor signaling in precision cut liver slices and spheroids. A. CLDN1 mAb suppresses ERK and Src phosphorylation in precision cut liver slices. One representative experiment out of two is shown. **B.** Heatmap showing the 20 most strongly modulated Protein Tyrosine kinases (PTK) and Serin/Threonin Protein Kinases (STK) in CLDN1 mAb vs. Control mAb treated spheroids (left panels). The modulation of the activities of the same kinases in fibrotic vs. healthy liver as described in a recently published kinome atlas of the fibrotic liver(*34*) is shown in the right panels. **C.** Model of CLDN1 receptor membrane biology. CLDN1 interacts with EGFR, ITGA5 and EPCAM mediating SRC and EGFR/ERK signaling. Abbreviations: CLDN1 = Claudin 1; EGFR= Epithelial growth factor receptor; LPS= Lipopolysaccharide, PTK= Protein Tyrosine Kinase; STK= Serin/threonine Protein Kinase.

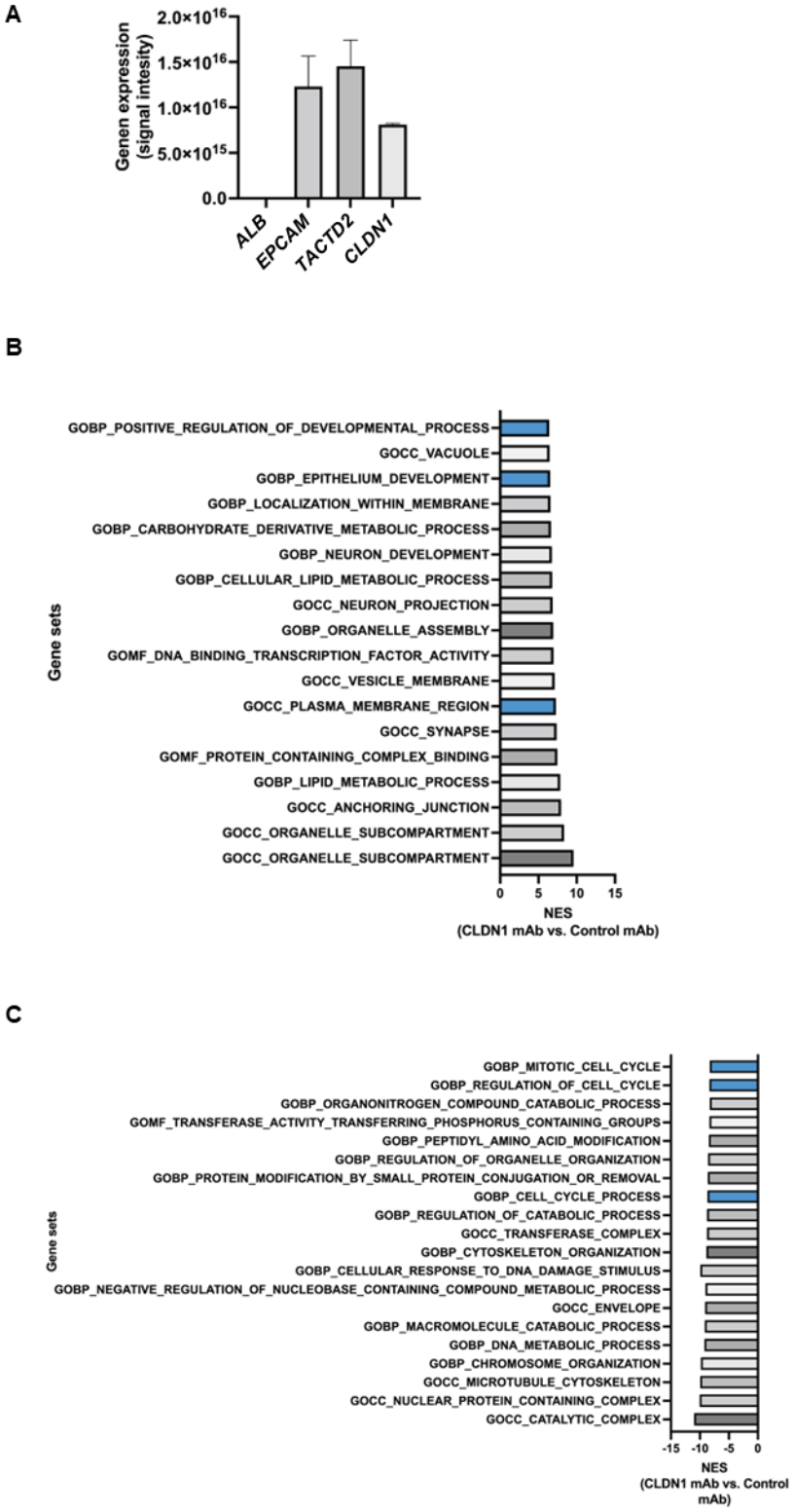
A
Genen expression (signal intesity)
2.0×10^16
1.5×10^16
1.0×10^16
5.0×10^15
0.0
ALB
EPCAM
TACTD2
CLDN1
B
Gene sets
GOBP_POSITIVE_REGULATION_OF_DEVELOPMENTAL_PROCESS
GOCC_VACUOLE
GOBP_EPITHELIUM_DEVELOPMENT
GOBP_LOCALIZATION_WITHIN_MEMBRANE
GOBP_CARBOHYDRATE_DERIVATIVE_METABOLIC_PROCESS
GOBP_NEURON_DEVELOPMENT
GOBP_CELLULAR_LIPID_METABOLIC_PROCESS
GOCC_NEURON_PROJECTION
GOBP_ORGANELLE_ASSEMBLY
GOMF_DNA_BINDING_TRANSCRIPTION_FACTOR_ACTIVITY
GOCC_VESICLE_MEMBRANE
GOCC_PLASMA_MEMBRANE_REGION
GOCC_SYNAPSE
GOMF_PROTEIN_CONTAINING_COMPLEX_BINDING
GOBP_LIPID_METABOLIC_PROCESS
GOCC_ANCHORING_JUNCTION
GOCC_ORGANELLE_SUBCOMPARTMENT
GOCC_ORGANELLE_SUBCOMPARTMENT
0 5 10 15
NES
(CLDN1 mAb vs. Control mAb)
C
Gene sets
GOBP_MITOTIC_CELL_CYCLE
GOBP_REGULATION_OF_CELL_CYCLE
GOBP_ORGANONITROGEN_COMPOUND_CATABOLIC_PROCESS
GOMF_TRANSFERASE_ACTIVITY_TRANSFERRING_PHOSPHORUS_CONTAINING_GROUPS
GOBP_PEPTIDYL_AMINO_ACID_MODIFICATION
GOBP_REGULATION_OF_ORGANELLE_ORGANIZATION
GOBP_PROTEIN_MODIFICATION_BY_SMALL_PROTEIN_CONJUGATION_OR_REMOVAL
GOBP_CELL_CYCLE_PROCESS
GOBP_REGULATION_OF_CATABOLIC_PROCESS
GOCC_TRANSFERASE_COMPLEX
GOBP_CYTOSKELETON_ORGANIZATION
GOBP_CELLULAR_RESPONSE_TO_DNA_DAMAGE_STIMULUS
GOBP_NEGATIVE_REGULATION_OF_NUCLEOBASE_CONTAINING_COMPOUND_METABOLIC_PROCESS
GOCC_ENVELOPE
GOBP_MACROMOLECULE_CATABOLIC_PROCESS
GOBP_DNA_METABOLIC_PROCESS
GOBP_CHROMOSOME_ORGANIZATION
GOCC_MICROTUBULE_CYTOSKELETON
GOCC_NUCLEAR_PROTEIN_CONTAINING_COMPLEX
GOCC_CATALYTIC_COMPLEX
-15 -10 -5 0
NES
(CLDN1 mAb vs. Control mAb)

Figure S15, related to Fig. 5. CLDN1mAb modulates gene expression related to cell proliferation and epithelial cell development in cirrhotic liver derived organoids. A. Gene expression of *ALB*, *EPCAM*, *TACSTD2* and *CLDN1* by RNAseq in cirrhosis-derived liver organoids. **B-C**. RNAseq data of CLDN1 mAb or control mAb-treated cirrhotic liver derived organoids were assessed by GSEA. Bars indicate normalized enrichment score of all significantly (FDR< 0.05, Kolmogorov-Smirnov test) enriched gene ontology pathways in CLDN1 mAb (A) or control mAb-(B) treated organoids. Blue color highlight most relevant pathways in liver organoids shown in Fig. 7D. Abbreviations: CLDN1= Claudin 1.

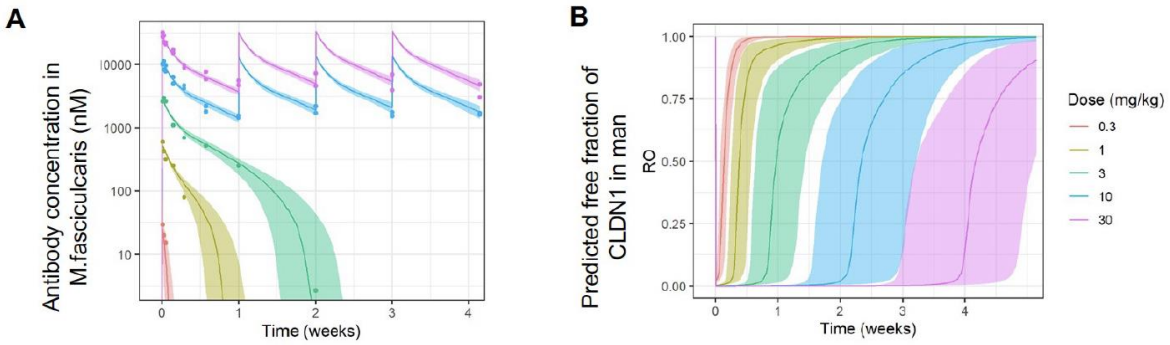

Figure S16. Anti-CLDN1 mAb pharmacokinetics in non-human primates. A. Predicted exposure of the anti-CLDN1 antibody ALE.F02 in macaques (median, 5th and 95th percentiles from 200 simulated profiles). Dots are the observed serum concentrations. All data in nmol/L, color correspond to the dose levels. **B.** Predicted receptor occupancy in human, indicating the total systemic free accessible CLDN1 not occupied by the administered antibody as a function of time. Shown are median, 5^{th} and 95^{th} percentiles from 100 simulated PK/PD profiles.

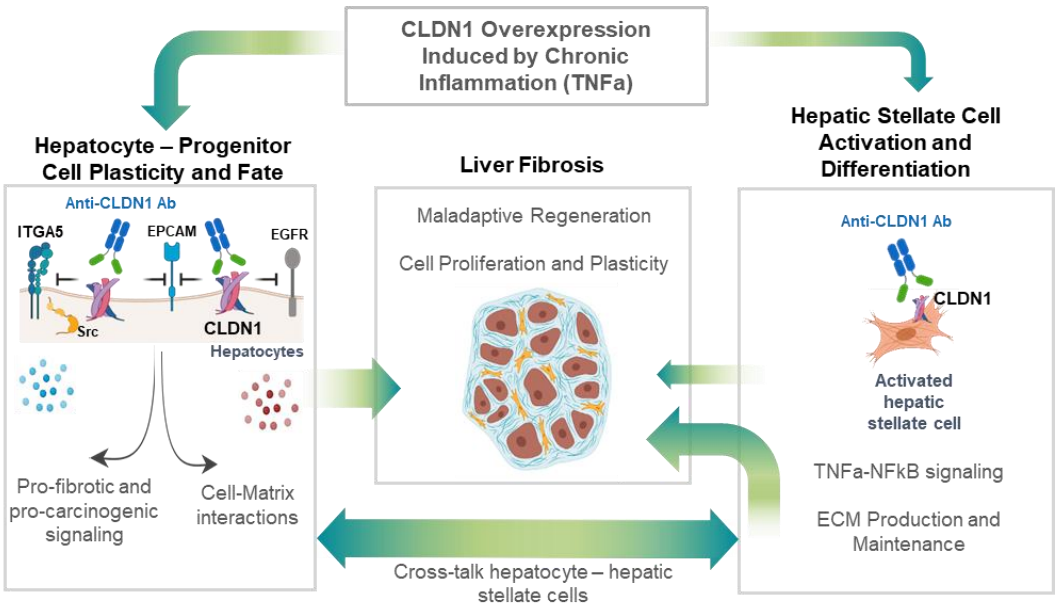

Figure S17. Mechanistic model of the anti-fibrotic effect of CLDN1 mAb in the liver. CLDN1 expression is regulated by the TNF-α-NFkB pathway and upregulated upon chronic inflammation. Liver epithelial cells including hepatocytes and its progenitors are the primary target cells of CLDN1 mAb mediating its anti-fibrotic effect. CLDN1 binds to EPCAM, EGFR and ITGA5 in the epithelial cell membrane and perturbation of these interactions by CLDN1 mAb inhibits downstream SRC and MAPK pathway, playing a key role in cell plasticity, cell-matrix interactions as well as fibrogenesis and carcinogenesis. The second cell type mediating the anti-fibrotic properties of the mAb are hepatic stellate cells/myofibroblasts. CLDN1 mAb inhibits TNF-α-NFkB signaling resulting in robust inhibition of myofibroblast activation and differentiation. Cross-talk between hepatocyte epithelial cells and fibroblasts ultimately results in suppression of maladaptive regeneration, cell proliferation and plasticity leading to ECM accumulation and fibrosis.

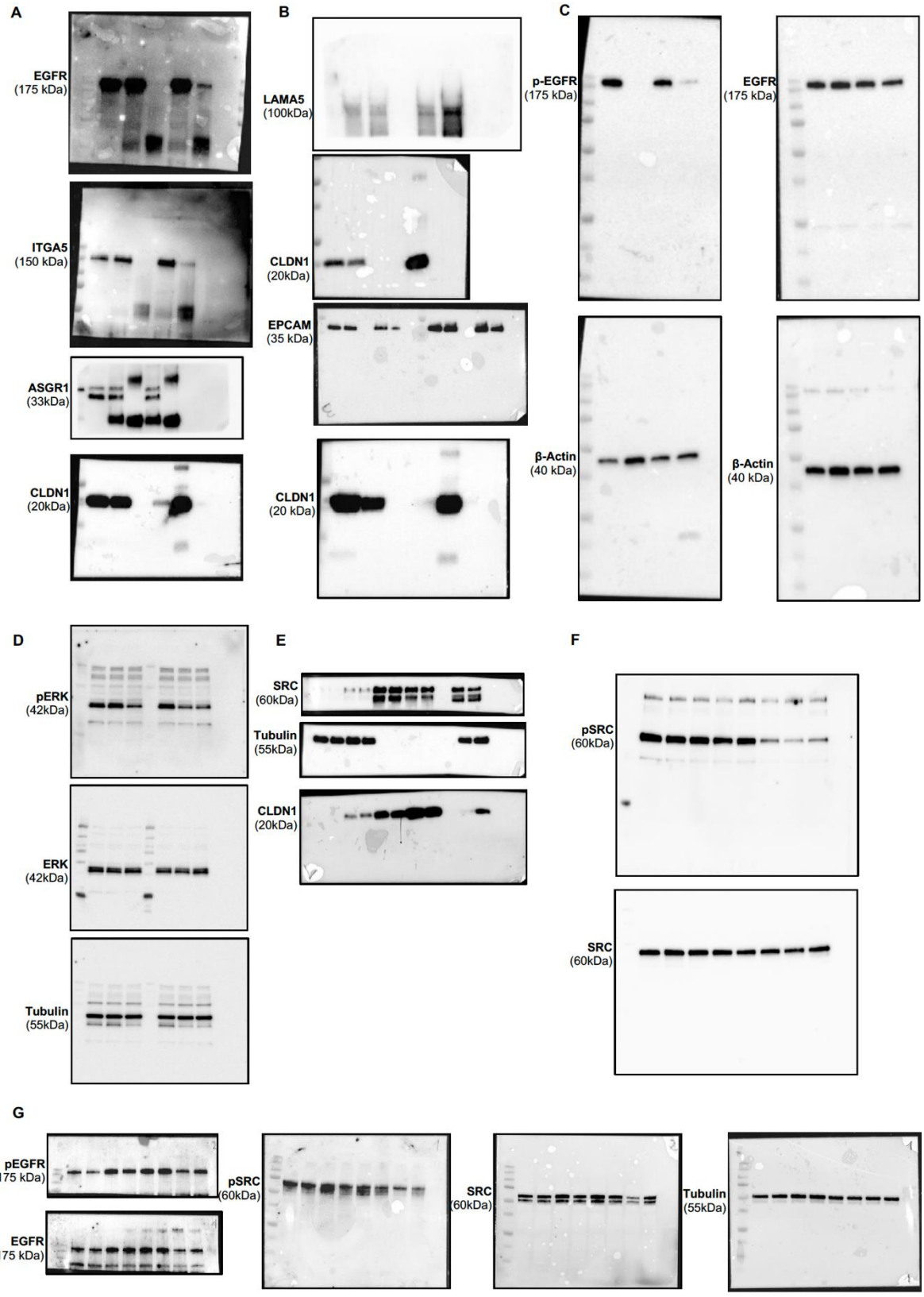

Figure S18. Original blots shown in Figure 6 and figure S14.

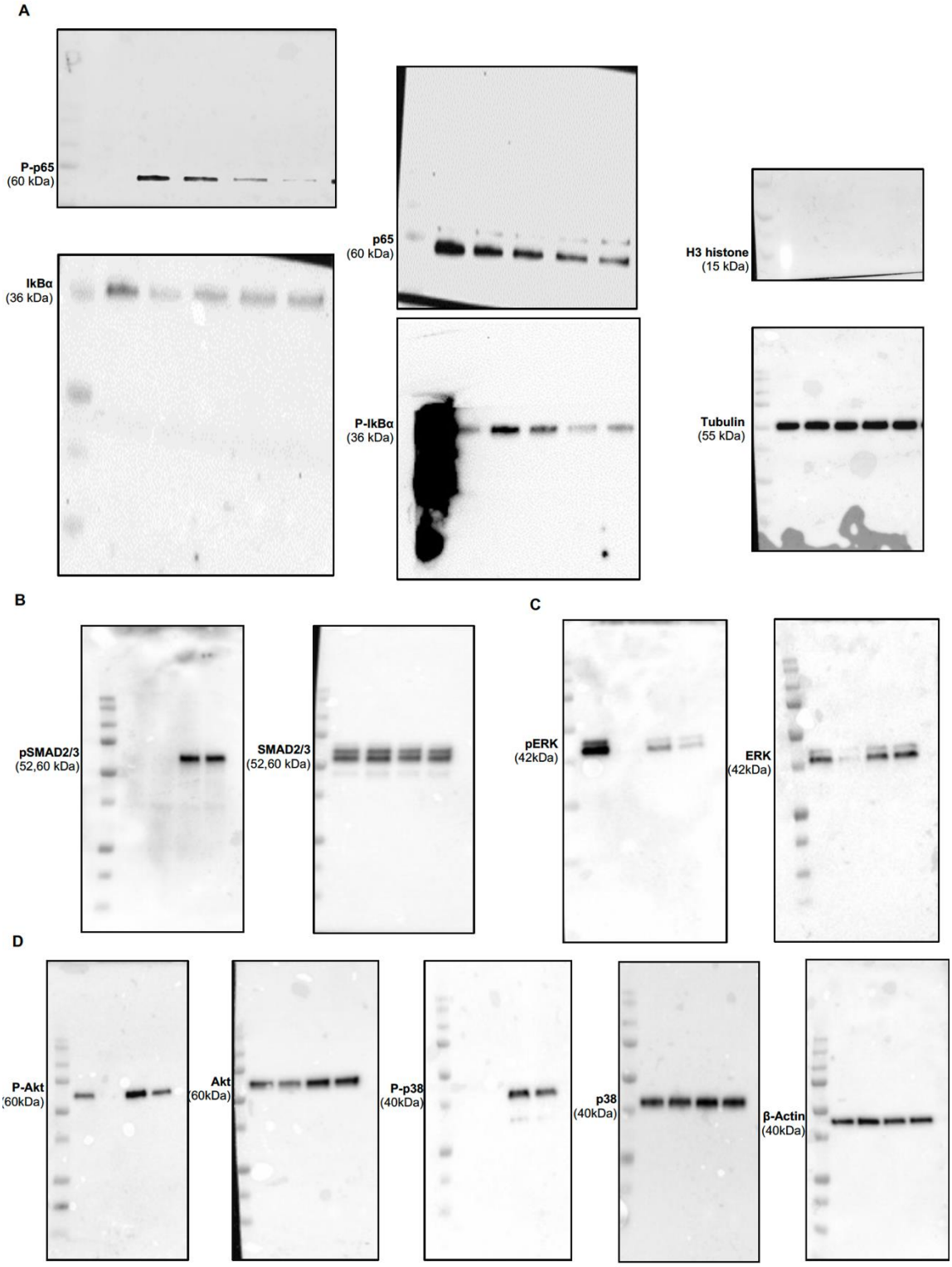

Figure S19. Original blots shown in Figure 7.

SUPPLEMENTARY TABLES

Table S1, related to Fig. 1A. Demographic and clinical characteristics of the University of Strasbourg NASH cohort.

	Control (n=10)	NASH (n=10)
Age (years)	43 (23-73)	39 (25-54)
Female (%)	18 (90)	4 (40)
Waist circumference (cm)	98.5 (75-149)	136 (100-170)
BMI (kg/m2)	31.9 (22.4-50.0)	46.9 (40.5-60.5)
Blood fasting glucose (mg/dL)	84 (66-130)	114 (83-162)
Insulin (µUI/mL)	6.1 (1.7-29.5)	9.2 (4.8-83.5)
HOMA-IR index	1.14 (0.33-5.90)	3.31 (0.99-33.40)
Total cholesterol (mg/dL)	166 (113-288)	151 (93-181)
Triglycerides (mg/dL)	122 (60-209)	194 (93-273)
FFA (mg/dL)	26 (8-36)	24 (13-35)
LDL cholesterol (mg/dL)	106 (59-217)	81 (46-101)
HDL cholesterol (mg/dL)	41 (31-67)	31 (18-42)
AST (UI/L)	21.5 (12-85)	48.5 (20-176)
ALT (UI/L)	18 (5-122)	56.5 (27-229)
ALP (UI/L)	60 (36-122)	54.5 (35-97)
GGT (UI/L)	20.5 (5-221)	35.5 (19-114)
Total bilirubin (mg/dL)	0.6 (0.3-1.01)	0.6 (0.3-0.9)
Iron (µg/dL)	76 (30-197)	66 (30-146)
Ferritin (ng/mL)	70.5 (14-399)	155 (10-2380)
Transferrin saturation %	27.5 (9-81)	23.5 (10-49)
CRP (mg/L)	2.84 (0.18-9.59)	6.27 (1.39-19.40)

Continuous variables are indicated as median and range. Abbreviations: ALP=alkaline phosphate, ALT=alanine aminotransferase, AST=aspartate aminotransferase, BMI=Body Mass Index, CRP=C-reactive protein, FFA=free fatty acid, GGT=gamma-glutamyl transferase, HDL=high density lipoprotein, HOMA-IR=homeostasic model assessment of insulin resistance, LDL=low density lipoprotein, NAFL=non-alcoholic fatty liver, NASH=non-alcoholic steatohepatitis.

Table S2, related to Fig. 2. Individual data of the main efficacy endpoints of the humanized NASH mice treated GalNAc siCLDN1 and siCTRL.

Group	Mouse ID	Fibrosis in humanized area %	Tumor Number
siCTRL	1512	4.874	83
	1513	3.738	31
	1515	3.782	25
	1528	3.819	28
	1555	5.94	25
	1558	4.33	45
Median		**4.07**	**29.5**
Mean		**4.41**	**39.5**
s.e.m.		0.35	9.2
siCLDN1	1505	2.743	23
	1506	0.596	6
	1509	3.295	17
	1511	4.79	4
	1722	2.633	34
Median		**2.74**	**17.0**
Mean		**2.81**	**16.8**
s.e.m.		0.67	5.5
Test		KW	KW
***p*-value**		**0.045**	**0.044**

Abbreviations: KW= Kruskal-Wallis test, s.e.m.= standard error of the mean.

Table S3, related to Fig. 2. Individual data of the main efficacy endpoints of the humanized NASH mice treated with vehicle control or humanized CLDN1 mAb.

Experiment #1

Group	Mouse ID	Total fibrosis %	Fibrosis in humanized area %	Tumor Number
Vehicle	4409	10.495	6.30	24
	4411	6.589	4.66	30
	4412	6.261	3.35	17
Median		**6.59**	**4.66**	**24.00**
Mean		**7.78**	**4.77**	**23.67**
s.e.m.		1.36	0.86	3.76
CLDN1 mAb	4405	1.101	0.51	17
	4407	5.843	1.80	5
	4408	3.168	1.51	12
	4424	1.516	0.68	11
Median		**2.34**	**1.09**	**11.50**
Mean		**2.91**	**1.12**	**11.25**
s.e.m.		1.08	0.31	2.46
Test		MW	MW	MW
***p*-value**		**0.0339**	**0.0339**	**0.0498**

Abbreviations: MW= Mann Whitney U test, s.e.m.= standard error of the mean.

Experiment #2

Group	Mouse ID	Total fibrosis %	Fibrosis in humanized area %	Tumor Number
Vehicle	1005	7.708	7.708	9
	1006	11.862	12.531	10
	4472	11.8925	11.8925	NA
	4477	6.048	4.438	22
	4478	1.167	0.886	13
	4479	10.4915	9.34	14
	4490	4.751	4.046	7
	4491	1.881	2.017	7
	4492	7.13	7.13	7
	4493	4.401	6.152	5
Median		**6.59**	**6.64**	**9.00**
Mean		**6.73**	**6.61**	**10.44**
s.e.m.		1.21	0.84	1.75
CLDN1 mAb	1001	2.11	2.667	5
	1002	4.55	5.352	5
	1008	1.48	1.48	4
	1009	4.446	4.5225	4
	1010	1.716	1.716	4
	4470	1.618	1.864	2
	4471	1.1705	1.5995	4
	4483	2.556	2.308	5
	4484	3.552	0.96	13
	4485	1.322	0.583	10
Median		**1.91**	**1.79**	**4.50**
Mean		**2.45**	**2.31**	**5.60**
s.e.m.		0.41	0.48	1.05
Test		MW	MW	MW
***p*-value**		**0.013**	**0.013**	**0.0093**

Abbreviations: MW= Mann Whitney U test, s.e.m.= standard error of the mean.

Table S4, related to Fig. 3. Individual data of the main efficacy endpoints of DEN-CDA-HFD mice treated with vehicle control or CLDN1 mAb.

Group	Mouse ID	Fibrosis %	Tumor macroscopy (Y=1/N=0)	Tumor N at histology	Max tumor size (mm)	Tumor HSP70+ (Y=1/N=0)
Vehicle	621	11.25	1	9	5.8	1
	622	8.59	1	7	2.2	1
	623	14.19	1	8	7.0	1
	624	9.95	1	3	1.5	0
	625	11.07	1	1	1.2	0
	631	9.53	0	0	NA	0
	632	18.69	1	3	1.5	0
	633	6.83	1	2	0.9	0
	634	7.69	1	1	2.1	0
	635	11.46	1	2	1.6	0
	641	8.28	1	11	1.2	1
	642	11.89	1	4	0.6	0
	643	8.24	1	3	1.0	0
	644	8.01	1	13	1.6	0
	645	8.79	1	10	8.1	1
	652	9.52	1	11	9.3	1
	653	6.67	1	17	13.0	1
	654	9.26	1	4	1.6	1
Median		**9.39**	**NA**	**4.00**	**1.62**	**NA**
Mean		**10.00**	**0.94**	**6.06**	**3.55**	**0.44**
s.e.m.		0.68	0.06	1.15	0.89	0.12
CLDN1 mAb	626	9.92	0	1	1.4	0
	627	11.76	1	7	6.0	1
	628	8.29	0	0	NA	0
	629	8.93	0	0	NA	0
	630	8.81	0	1	0.9	0
	636	5.16	0	2	0.5	0
	637	4.64	0	3	0.8	0
	638	6.57	1	2	1.3	0
	639	4.76	1	2	1.3	0
	640	6.87	0	1	1.1	0
	646	6.05	0	0	NA	0
	647	6.29	0	1	0.7	0
	648	13.55	1	2	1.1	0
	649	4.33	0	1	0.6	0

	650	6.06	0	1	0.6	0
	656	4.39	1	6	1.5	0
	657	7.91	0	0	NA	0
	658	8.60	0	2	0.4	0
	659	4.94	0	2	0.8	0
	660	7.97	1	3	1.1	0
Median		**6.72**	**N/A**	**1.50**	**1.00**	**N/A**
Mean		**7.29**	**0.30**	**1.85**	**1.25**	**0.05**
s.e.m.		0.56	0.11	0.41	0.33	0.05
Test		**MW**	**FT**	**MW**	**MW**	**FT**
***p*-value**		**Per mouse 0.003 Per image <0.001**	**<0.001**	**0.001**	**0.001**	**0.007**

Abbreviations: FT= Fisher test, HSP70= heat shock protein 70, MW= Mann Whitney U test, N/A= not applicable., s.e.m.= Standard error of the mean.

Table S5, related to Fig. 3. Metabolic parameters and CLDN1 mAb concentrations in DEN-CDA-HFD mice treated with vehicle control or murinized CLDN1 mAb.

	Vehicle (mean ± s.e.m.)	CLDN1 mAb (mean ± s.e.m.)	*p*-value (MW test)
ALT (UI/L)	244 ± 12	217 ± 14	**0.033**
AST (UI/L)	276 ± 16	271 ± 20	0.664
ALP (UI/L)	129 ± 30.2	103.1 ± 3.3	0.584
Total bilirubin (µmol/L)	3.89 ± 0.40	4.57 ± 0.62	0.511
Total proteins (g/L)	46.2 ± 0.8	49.1 ± 0.4	**0.013**
Albumin (g/L)	22.4 ± 0.7	23.8 ± 0.5	0.275
Creatinine (µmol/L)	8.79 ± 0.50	7.98 ± 0.39	0.316
Urea (mmol/L)	9.01 ± 0.18	8.75 ± 0.39	0.371
Sodium (mmol/L)	145.0 ± 1.7	147.7 ± 0.7	0.059
Potassium (mmol/L)	5.33 ± 0.14	5.04 ± 0.13	0.152
Calcium (mmol/L)	2.05 ± 0.04	2.09 ± 0.02	0.602
Glucose (mmol/L)*	8.25 ± 0.51	9.12 ± 0.31	0.179
Total cholesterol (mmol/L)*	1.08 ± 0.06	1.12 ± 0.05	0.784
CLDN1 mAb (µg/mL)	--	125.8 ± 8.5	--

*Mice not fasted.

Abbreviations: ALT= alanine aminotransferase, AST= aspartate aminotransferase, ALP= alkaline phosphatases, MW= Mann Whitney U test, s.e.m.= standard error of the mean.

Table S6, related to Fig. 3. Individual data of the main efficacy endpoints of DDC mice treated with vehicle control or anti-CLDN1 mAb.

Group	Mouse ID	CPA %	Ishak score
Vehicle	1746	9.505	3
	1747	8.77	3
	1748	10.46	2
	1749	11.456	4
	1750	12.03	2
	1756	8.542	2
	1757	12.4	4
	1758	8.902	3
	1759	12.488	3
	1760	8.505	3
	1766	10.725	3
	1767	11.172	4
	1768	10.103	3
	1769	10.774	3
	1770	12.057	3
	1776	11.539	4
	1777	10.485	3
	1778	11.498	3
	1779	9.644	4
	1780	12.207	4
Median		**10.749**	
IQR		2.053	
Mean		**10.663**	
sd		1.328203	
CLDN1 mAb	1741	6.917	2
	1742	10.031	3
	1743	6.557	2
	1744	8.872	3
	1745	8.099	2
	1751	7.08	2
	1752	7.487	3
	1753	8.559	3
	1754	8.314	4
	1755	7.207	2
	1761	8.167	2
	1762	8.723	2

	1763	8.792	3
	1764	8.366	3
	1765	8.925	3
	1771	7.227	3
	1772	7.07	3
	1773	7.327	2
	1774	6.595	3
	1775	5.54	2
Median		**7.793**	
IQR		1.523	
Mean		**7.793**	
sd		1.064973	

Test	**T**
95% C.I.	-3.64 to -2.09
***p*-value**	**<0.0001**

Abbreviations: IQR = Interquartile range; sd = standard deviation; T = Student's T-test; 95% C.I. = 95% Confidence Interval.

Table S7, related to Fig. 4. Demographic and clinical characteristics of patients shown in **Fig. 4C-G**.

	Age(y)	*Sex*	*Chronic liver disease*	*Indication for liver resection*	*Fibrosis stage*	*Applied type of tissue*
353	83	M	NAFLD	HCC	F2	**diseased, non-tumorous**
351	78	M	NAFLD	CCM	F0	**diseased, non-tumorous**
410	70	M	-	CCM	F0	**healthy, non-tumorous**
471	70	M	-	GBC	F0	**healthy, non-tumorous**
525	50	F	-	BCM	F0	**healthy, non-tumorous**
452	75	M	-	NETM	F0	**healthy, non-tumorous**
506	48	F	-	CCM	F0	**healthy, non-tumorous**
514	31	F	-	CCM	F0	**healthy, non-tumorous**
515	44	M	-	CCM	F0	**healthy, non-tumorous**
480	-	-	-	CCM	F0	**healthy, non-tumorous**
481	-	-	-	CCM	F0	**healthy, non-tumorous**
484	-	-	-	CCM	F0	**healthy, non-tumorous**
488	-	-	-	CCM	F0	**healthy, non-tumorous**
489	-	-	-	HCC	F4	**diseased, non-tumorous**

Abbreviations: BCM= breast cancer metastasis, CCM= colon cancer liver metastasis, F= female, GBC= Gallbladder adenocarcinoma, HCC= Hepatocellular carcinoma, M= male, NAFLD= Non-alcoholic fatty liver disease, NASH=Non-alcoholic steatohepatitis, NETM: pancreatic neuroendocrine tumor metastasis; y= years.

Table S8, related to Fig. 4. Demographic and clinical characteristics of patients shown in **Fig.4H**.

	NASH #1	*NASH #2*	*NASH #3*	*NASH #4*	*NASH #5*
Age (years)	74	60	74	81	75
Sex (Male/Female)	Male	Male	Male	Male	Male
Fibrosis stage(*26*)	4	3	3	4	2
Obesity (Yes/No)	Yes	No	No	No	No
Diabetes (Yes/No)	Yes	Yes	No	No	Yes
Hypertension (Yes/No)	Yes	Yes	No	No	No

Abbreviations: NASH= Non-alcoholic steatohepatitis.

Table S9, related to Fig. 5. Genes used to define the scar-associatd myofibroblast*.

DCN	*TMSB10*	*FBLN1*	*RPL36*	*CYR61*	*MARCKSL1*
C1R	*EFEMP1*	*CD81*	*PRSS23*	*CCL2*	*THBS2*
LUM	*BGN*	*MMP2*	*IL32*	*RPS12*	*CTSC*
COL3A1	*MMP23B*	*PDGFRA*	*ANXA1*	*ADAMTSL2*	*TCEAL4*
C1S	*IFITM3*	*FBLN5*	*NR2F1*	*IGFBP7*	*EMP3*
C7	*PPIB*	*COLEC11*	*TSPAN4*	*CTSD*	*WBP5*
COL1A2	*NNMT*	*CD74*	*COL5A1*	*ITGBL1*	*RPLP1*
COL1A1	*NPC2*	*SPON2*	*ENG*	*IGFBP3*	*RPS17*
CFH	*COL6A1*	*COL6A3*	*RPL37*	*FSTL1*	*RPS23*
TIMP1	*MARCKS*	*COL14A1*	*ISLR*	*PPIC*	*RPS15*
PCOLCE	*AEBP1*	*G0S2*	*RPS15A*	*FCGRT*	*HLA-DPA1*
CST3	*THY1*	*LTBP4*	*PTGDS*	*PLTP*	*COL4A2*
OLFML3	*HLA-DRB1*	*RCN3*	*RRBP1*	*SSR2*	*TFPI*
CXCL12	*SRPX*	*IGFBP4*	*EFEMP2*	*RPS18*	*HLA-DRA*
CLEC11A	*COL6A2*	*LY6E*	*INMT*	*CLEC2B*	*IGF2*
GGT5	*S100A10*	*MGP*	*SPARC*	*IGFBP6*	*LAMB1*
CD63	*MEG3*	*RPL13*	*ECM1*	*TIMP2*	*CCL21*
FTL	*EMILIN1*	*LGALS3BP*	*CCDC80*	*VCAN*	*CEBPD*
RARRES2	*RPL12*	*TMEM176A*	*SERPING1*	*ALDH1A1*	*RARRES1*
ASPN	*S100A11*	*PRELP*	*FN1*	*TPT1*	*DAAM1*
S100A13	*LRP1*	*TYROBP*	*LXN*	*QSOX1*	
RBP1	*ADH1B*	*TMEM176B*	*MFAP4*	*RPS24*	
SERPINF1	*CYBA*	*IFITM1*	*RPL39*	*RAMP1*	
DPT	*RPL28*	*RPS28*	*VKORC1*	*F2R*	

*derived from(*16*).

Table S10, related to Fig. 7. Genes used to define the scar-associated myofibroblast type A*.

COLEC11	*HLA-A*	*EDNRB*	*CALM2*	*MASP1*	*PTGIR*
IGFBP7	*HLA-DRB1*	*HGF*	*CITED2*	*ALDH1A1*	*HLA-DRB5*
PPP1R14A	*HLA-B*	*HLA-C*	*TMEM204*	*TMSB4X*	*ITM2C*
GGT5	*C11orf96*	*TPM1*	*COX7A1*	*CTSD*	*SGCA*
CALD1	*LTBP4*	*ENG*	*BST2*	*HLA-DPA1*	*ARHGAP15*
TYROBP	*4-Sep*	*COL4A2*	*CCL21*	*MARCKS*	*RGS16*
B2M	*MYL9*	*RAMP1*	*RBPMS*	*ASPN*	*COL4A1*
ADAMTSL2	*C8orf4*	*IGFBP3*	*RBP1*	*GPX3*	

*derived from(*16*).

Table S11, related to Fig. 7. Genes used to define the scar-associated myofibroblast type B*.

COL1A2	*IGF1*	*NNMT*	*RPLP0*	*YBX3*	*LXN*
S100A6	*RARRES1*	*TSHZ2*	*VIM*	*MMP2*	*CCND2*
C3	*SERPINF1*	*ADIRF*	*ANXA1*	*RPSA*	*SFRP2*
FBLN1	*MDK*	*STEAP1*	*RPS3*	*PTGIS*	*IGFBP4*
CCDC80	*CLU*	*CTHRC1*	*S100A16*	*IGFBP2*	*DNAJB1*
COL1A1	*FSTL1*	*COL6A3*	*DHRS3*	*NR4A2*	*PLP2*
OGN	*SLIT3*	*LGALS1*	*VCAN*	*SVIL*	*CAV1*
SPARCL1	*ANXA2*	*OSR1*	*COL6A1*	*BOC*	*MGP*
S100A4	*IGFBP6*	*OAF*	*MMP23B*	*GPRC5A*	*CAPZB*
NBL1	*COL3A1*	*S100A10*	*CRABP2*	*PCOLCE*	

*derived from(*16*).

Table S12, related to Fig. 7. Demographic and clinical characteristics of patients recruited for isolation of HSCs.

ID	*Age(y)*	*Sex*	*Chronic liver disease*	*Indication for liver resection*	*Isolated cell type*
352	**48**	**M**	**No**	**CCM**	**HSCs**
372	**51**	**M**	**No**	**CCM**	**HSCs**
374	**59**	**F**	**No**	**CCM**	**HSCs**
383	**71**	**F**	**No**	**CCM**	**HSCs**
389	**82**	**F**	**NAFLD (F2)***	**CCA**	**HSCs**
397	**23**	**F**	**No**	**PHL**	**HSCs**
401	**36**	**F**	**No**	**CCM**	**HSCs**

*Fibrosis stage(*26*)

Abbreviations: CCA= Cholangiocellular Carcinoma, CCM= Colon cancer liver metastasis; HSC=Hepatic stellate cells, NAFLD= Non-alcoholic fatty liver disease, PHL= Primary hepatic leiomyosarcoma, y= years.

Table S13, related to Fig. 8. Individual Sirus-red positive areas in renal fibrosis UUO mice treated with vehicle control or CLDN1 mAb.

Control						CLDN1-specific mAb					
Mouse ID	Photo No.	Total area (pixel)	Positive area (pixel)	Positive area (%)	Positive area (%)	Mouse ID	Photo No.	Total area (pixel)	Positive area (pixel)	Positive area (%)	Positive area (%)
101	1	3145728	344415	10.95	8.88	201	1	2942661	91823	3.12	3.14
	2	3145728	277600	8.82			2	3145728	9667	0.31	
	3	3145728	616310	19.59			3	3145728	178982	5.69	
	4	3145728	106844	3.40			4	3145728	105012	3.34	
	5	2525427	41941	1.66			5	3145728	102614	3.26	
102	1	3145728	54042	1.72	6.88	202	1	2955677	149707	5.07	4.26
	2	1852892	282606	15.25			2	3145728	157964	5.02	
	3	2901737	105846	3.65			3	3145728	158958	5.05	
	4	2680358	270561	10.09			4	3145728	137962	4.39	
	5	1677944	61894	3.69			5	3145728	55942	1.78	
103	1	2613185	45756	1.75	12.74	203	1	3145728	106839	3.40	3.01
	2	3145728	79596	2.53			2	3145728	96460	3.07	
	3	3145728	105531	3.35			3	3145728	104407	3.32	
	4	2128925	256408	12.04			4	3145728	108886	3.46	
	5	1805725	795103	44.03			5	3145728	56876	1.81	
104	1	1907636	96743	5.07	5.62	204	1	2053687	221370	10.78	7.07
	2	3145728	116189	3.69			2	2922969	175727	6.01	
	3	2498956	300009	12.01			3	3145728	280234	8.91	
	4	3145728	197408	6.28			4	3145728	95235	3.03	
	5	3145728	32587	1.04			5	3145728	208497	6.63	
105	1	3145728	107920	3.43	5.12	205	1	3145728	26479	0.84	1.70
	2	3145728	228570	7.27			2	3145728	113376	3.60	
	3	3145728	57914	1.84			3	3145728	31501	1.00	
	4	3145728	163861	5.21			4	3145728	24949	0.79	
	5	3145728	247323	7.86			5	3145728	71784	2.28	
106	1	2391160	25941	1.08	5.31	206	1	3145728	56743	1.80	1.77
	2	2481193	192484	7.76			2	3145728	84916	2.70	
	3	2409692	128920	5.35			3	3145728	52829	1.68	
	4	3145728	46287	1.47			4	3145728	61369	1.95	
	5	3145728	343353	10.91			5	3145728	22164	0.70	
107	1	2952140	36770	1.25	9.96	207	1	3145728	44821	1.42	0.79
	2	1283270	262341	20.44			2	3145728	33427	1.06	
	3	1882451	145227	7.71			3	3145728	33393	1.06	
	4	3145728	140876	4.48			4	3145728	5123	0.16	
	5	2652902	421933	15.90			5	3145728	7575	0.24	
108	1	3145728	225836	7.18	5.42	208	1	3054515	39178	1.28	1.41
	2	3145728	302298	9.61			2	3016949	51887	1.72	
	3	3145728	207383	6.59			3	2771583	44394	1.60	
	4	3145728	88954	2.83			4	2615483	39127	1.50	
	5	3145728	28495	0.91			5	2568128	23833	0.93	

Table S14, related to Fig. 8. Individual Ashcroft scores in bleomycin pulmonary fibrosis mice treated with vehicle control or anti-CLDN1 mAb.

Group	Mouse ID	Photo No.																				Mean
		1	2	3	4	5	6	7	8	9	10	11	12	13	14	15	16	17	18	19	20	
Control	101																					
	102	5	3	3	3	3	3	1	2	2	2	1	2	1	2	1	2	2	2	2	1	2.2
	103	4	6	7	7	3	6	7	7	6	6	7	5	4	3	5	3	2	1	3	1	4.7
	104	5	3	3	3	3	3	2	3	3	4	3	3	3	3	3	3	2	3	1	1	2.9
	105	5	6	6	6	6	3	4	8	7	3	3	4	6	5	6	7	5	3	2	1	4.8
	106	4	5	3	4	5	5	3	3	5	6	6	3	3	2	2	4	3	4	3	3	3.8
	107	3	3	3	3	5	2	3	5	6	8	8	7	6	7	6	3	4	3	8	8	5.1
	108																					
	109	3	6	8	8	5	2	5	3	4	3	7	8	8	8	5	4	5	8	6	6	5.6
	110	2	1	2	1	1	1	1	1	2	1	1	1	1	1	1	1	1	1	2	1	1.2
	111	2	2	2	2	1	2	2	2	1	3	3	2	1	1	1	2	2	2	2	2	1.9
	112																					
	113																					
	114	4	5	4	4	2	2	2	3	3	4	3	2	1	2	2	2	3	3	3	3	2.9
	115	4	4	6	3	5	3	3	3	3	3	3	3	3	4	4	3	2	3	2	3	3.4
	116	7	7	7	7	7	7	7	7	7	7	7	8	7	7	6	6	5	4	3	3	6.3
	117	5	5	3	5	7	7	3	8	5	7	7	7	7	5	4	5	3	3	3	5	5.2
	118	5	7	6	5	7	6	6	3	4	5	6	3	3	8	5	5	4	3	4	3	4.9
CLDN1-specific mAb	201	2	3	3	2	2	3	1	3	1	1	1	3	1	3	4	1	3	2	3	2	2.2
	202																					
	203	1	1	1	3	0	2	3	3	1	2	0	0	1	1	0	2	2	2	4	3	1.6
	204	1	1	2	3	2	1	0	0	1	1	0	0	2	1	2	5	4	3	2	3	1.7
	205	4	3	3	3	3	3	3	4	3	3	2	4	3	2	3	3	3	3	3	5	3.2
	206	3	4	2	3	4	4	2	3	3	3	3	2	1	2	3	3	3	3	3	2	2.8
	207	3	4	3	3	3	3	3	3	2	2	2	2	3	3	3	4	3	3	2	3	2.9
	208	2	1	3	1	2	2	2	2	3	3	1	1	1	4	3	4	2	3	3	2	2.3
	209	3	1	3	3	3	3	1	3	3	3	3	1	2	4	2	3	3	3	3	2	2.6
	210																					
	211																					
	212	1	1	3	4	3	3	3	4	3	4	2	3	3	2	3	5	2	4	3	2	2.9
	213	2	3	3	3	3	3	3	3	3	4	5	7	8	8	8	8	7	3	7	5	4.8
	214	3	3	3	3	3	2	3	2	3	3	2	3	4	3	4	2	3	3	3	2	2.9
	215	3	5	3	6	4	5	3	3	4	2	3	3	4	6	6	8	2	4	3	3	4.0
	216	2	3	3	2	3	3	3	3	3	2	3	3	3	3	2	3	3	3	3	3	2.8
	217																					
	218																					

2333 **Table S15, related to Fig. 8.** *HAS*^{high} fibroblast marker genes*.

AC090498.1	ETF1	GNPTAB	CSTB	MESDC1	ANKRD37	ATPIF1	HLA-C
MT-CYB	KIAA1324L	LITAF	RCAN1	RAB3A	TLE1	ZFAND3	METAP2
A2M	PGM3	MYL9	MID1	SLC25A33	RCN3	CD70	PPP4R2
CDKN2A	PTGES3	ISG20L2	PKM	CEBPZ	OSER1	PFKFB3	NR2F2
GALNT13	FAT1	CDKN1A	MAP1LC3B	CACNA2D1	IGF2	VCAN	ADD3
HSP90AA1	CXorf40B	SLC16A1	MTRNR2L12	SMARCA1	CD276	EDNRA	WTAP
HSPE1	PTP4A1	GPRC5A	COL6A2	SEMA3C	YPEL2	EMP1	EFEMP1
LINC01605	CD9	PRRC2C	GXYLT2	SKIL	GOLM1	CDC42EP2	MT1M
HSPD1	CERCAM	MGP	ATXN7	UCK2	HINT1	SPCS1	ARPC5L
FHL2	ARF4	PNPLA8	CTSL	HBEGF	CREM	QSOX1	PDLIM4
KIAA1217	COL1A1	HAS1	RALGPS2	S1PR3	PPIC	ARMCX3	WT1
PDLIM3	EIF5A	PLK2	THBS3	FGF2	OAF	JARID2	FRZB
NAF1	FAM180A	FKBP4	MT-ND5	TOB1	BAG2	TFG	KDELR2
TNFSF9	MORF4L2	BTAF1	ARC	SFTPC	CCDC71L	SOCS3	IFITM3
LINC00152	ISLR	RPL17	GAS7	FLNA	THBS2	CXCL14	XBP1
MT-ATP8	INSIG1	ARHGAP5	CYB5A	RHOC	PCDH7	MAP2K3	CYP1B1
SELK	MEDAG	VEGFA	PITPNB	ATP5G2	ERVK3-1	ARSI	ADGRD1
SLC12A8	ZBTB21	IFITM2	CMTM3	PPRC1	NAV1	MYH9	LIMCH1
MT-CO2	MAP4K5	SLC4A7	TAF13	MT-ND4	CPNE8	WWTR1	H3F3A
TLL1	BLOC1S6	C16orf45	TCF21	SCGB1A1	ARHGDIB	MINOS1	SFPQ
AC113404.1	STIP1	KLHL21	IPMK	PTRH2	MAP3K4	SCG2	PSAP
MT-CO3	TPM2	FERMT2	BAZ1A	ECM1	ALDH2	HLA-DPB1	CHSY1
HSP90AB1	RP11-210L7.3	ROR1	HSPB8	ADAMTS16	YWHAQ	GLA	KDM5B
CDKN2B	AHSA1	PAMR1	VAT1	TEX10	COX4I2	PGAP1	PTGES

HSPA4L	GEM	TXN	JOSD1	CLDN11	EBF1	MAGED1	LAMC1
FEM1C	ITGB1	UBE2B	CTC-444N24.11	MICAL2	CALM1	LY96	USP2
ABL2	OSMR-AS1	ZNF460	VIM	TFB2M	IGF1	SRGN	ATP5L
HSPA8	MEG3	BAIAP2	NDEL1	CTSD	EIF3J	GOPC	PCBP2
MXRA5	KDM6B	ASB1	MCC	TUBB2A	EIF2S1	CHIC2	PDGFRL
MT-CO1	PTHLH	IQCJ-SCHIP1	UBAP1	NGF	SEPW1	RSL1D1	ZFC3H1
GPX3	SULF1	MYC	MIR22HG	JAG1	SAMD9	CTSK	BNC2
RP11-474O21.5	ACLY	COL3A1	TUBB3	HTRA3	COX4I1	PNO1	HNRNPAB
RABGEF1	MIR4435-2HG	HSD3B7	HMGN2	MAPRE1	GART	ANGPT1	SPG20
LINC01060	CCT2	HSPA1A	RUNX2	HMGN3	RCN1	CSNK1A1	MAPK1IP1L
UGDH	PDK4	GNG12	LRRC59	MLF1	STAG1	ANXA5	KRT18
GCLM	TES	ARL5B	BMP1	GTPBP4	LSM12	NNMT	SRP14
USP12	FAM3C	CEBPD	SDC2	DOT1L	DENND4A	LOX	LRRC17
TAGLN	CHMP1B	PLIN3	OSMR	CCNK	PXDN	TGIF1	PHGDH
NRIP1	NR4A3	PRKCI	MSC	3-Mar	CD248	EPHX1	CLIP1
DNAJA1	EIF1	ANKRD28	TSR1	TMEM263	SMS	ANK2	HNRNPF
DCBLD2	NR4A2	PRRX1	HBP1	RRM1	ANGPTL4	C1QTNF3	IGFBP7
CRABP2	ELOVL5	FBN1	NOTCH2	ADAMTSL1	SESN3	CDC42SE1	AMD1
ZBTB38	STX4	RARG	KIAA1462	CRIP2	RGS2	FKBP14	TMEM59
RLF	FNIP2	VAPB	TGM2	NDFIP2	SSR4	SH3D19	LOXL1
BAG3	SCGB3A1	CDK17	KPNA4	AC058791.1	TPBG	FLNB	TOR1AIP2
CHORDC1	SERTAD1	SLC19A2	SERTAD2	KTN1	UBQLN1	ARPC3	ANKLE2
SPARC	SGK1	RND3	ADAMTS2	NOP58	MYL6	FKBP5	CTTN
DYRK3	SLC30A1	BZW2	EGR3	KLF4	BDNF	NUP58	PER3
ZSWIM6	HERC4	TXNRD1	FOSB	ZMAT3	GALNT2	UQCR10	GLUD1
PLA2G4A	HAS2	HIVEP2	TUBA1C	FSCN1	RBP1	CXCL6	CCDC80
CPXM1	ZDBF2	RAB7A	NFE2L2	CCNT1	ZC3HAV1	CMSS1	SMDT1

SERPINH1	DPYSL3	PANX1	SMIM3	SLFN11	PSME1	ITPRIP	KPNA2
DOK5	PRRG3	SELM	RNF149	UBE2D3	RNASEK	HSPB1	PEG10
MT-ND4L	HDLBP	ALDH1A3	AKAP12	FNDC1	AGO2	OTUD4	COX6A1
HSPA4	COQ10B	CPZ	EGFL6	SEPP1	CLMP	TUBB2B	CHCHD10
ANXA1	ASCC3	CADPS2	CTNNAL1	TIMP2	H3F3B	RC3H1	GPC1
ARL4C	DNAJB6	ATP13A3	HMOX1	TCEB1	S100A4	NUPR1	MYL12A
COL1A2	MT-ND2	FBXO34	C10orf10	RPS6KA3	TAF1D	RARRES1	ARHGAP21
SQSTM1	TIPARP	IPO7	ITGAV	CIRBP	AFG3L2	SERINC5	EPB41L2
TCP1	MTRNR2L8	HRH1	MAPK6	DDX21	SH3PXD2B	EDIL3	LY6E
PHLDA1	TSC22D2	INPP1	RGMB	IDI1	NIFK	ADH1C	ADAMTS15
NT5E	P4HA1	TNFRSF10B	MMP2	CCDC109B	CD44	PTPN1	CXCL12
ARID5B	MT-ND3	TNFAIP6	METRNL	MYOF	FAM110B	TRAF4	ETNK1
ROR1-AS1	JAM3	UAP1	SPON2	BZW1	DDX3X	ABHD2	PLA2G5
SNAI2	TWIST1	PLAUR	TIMP3	NTM	SEMA4A	DSTN	GRPEL1
GJA1	PPP1R14A	UCHL3	MAP4K4	GPSM2	UHRF1BP1L	DSEL	CILP2
LIMA1	PTGIS	JUN	CNTN4	EMILIN2	TRIO	NFATC1	FBLN2
LRRC8C	LMCD1	CD74	UTP4	AFF4	KCNE4	FKBP10	SUMO2
ZFAND2A	TPM4	FGFR1	CLEC11A	NOP16	USP15	SPSB1	HMGB1
SPAG9	IL1R1	ERRFI1	AFAP1	TSPO	MIR222HG	UBE3A	NOV
HSPH1	ANGPTL2	PLOD2	NOLC1	CADM3	GABPB1	TMEM2	ALDH1A1
RPS26	RPL41	GABARAPL1	TNFRSF12A	CTNNB1	AOC3	SOX4	CA12
CHD1	REL	GNAI3	LRIF1	TTC3	RGS5	SRGAP1	HIGD1B
EIF4E	KCTD9	YWHAZ	ZFP36L1	AKIRIN1	GNL2	IL33	PERP
YWHAG	ELL2	SACS	CLIC4	FRS2	MDM2	FABP5	KLF2
CBLB	DDX3Y	FRMD6	IFI16	GSTP1	EMP2	SEC23A	PABPC1
DNAJB4	FAM198B	PPTC7	NXT1	GNL3	UFM1	COX8A	NFAT5

MSX2	C1QTNF6	COL4A1	MRPL18	HIST3H2A	SLC40A1	CCT3	C14orf2
RAB23	PPDPF	COL4A2	DNTTIP2	ITGA11	IL6R	PEBP1	BCAP31
PEA15	TICAM1	MAFF	DNAJB9	SLC20A1	SEMA3B	NUFIP2	HOTAIRM1
DRAM1	TOP1	NBPF14	ALG13	PRMT9	ELN	RGCC	SEMA6A
EIF4A3	COL6A1	WDR43	FKBP9	NDUFA4	HLA-DPA1	DES	NDUFA3
LHFPL2	ETV3	MLLT11	MED13	CREB3L1	COL5A1	PIM1	ACSL3
DNAJB1	WBP5	HNRNPA2B1	LATS2	CCT4	PFDN2	DDX5	OLFML3
IL6ST	SOD3	DNMBP	NUP153	ESYT2	HIVEP1	AHNAK	EIF5
ACTA2	SLPI	SDCBP	SERBP1	TPT1	HIPK3	FLRT2	PHLDB2
YES1	ABI3BP	CD55	C3orf58	CRY1	APP	IGFBP6	CD68
ADH1B	CREB5	NAA50	FOSL1	TRIM69	EIF1AX	PAICS	MAP3K8
GLIS3	MMP14	MAT2A	KLF3	HEG1	FLNC	SSC5D	PCDHGC3
MT-ND1	DPT	CAMSAP2	FAM114A1	CYP51A1	ANKH	KDELR3	ANXA2
HSPA9	PTGFRN	RCOR1	PCBP1	HNRNPH3	ARL4D	IER3	KRTCAP2
C1orf21	SYAP1	HSPA1B	USP36	MRC2	UBL3	CKAP4	COL5A2
SNX9	APOD	GPC6	ACSL4	TSC22D1	PHLDB1	RAB1A	INHBA
RYBP	GFPT2	HNRNPA0	TSPAN5	NDUFA4L2	EDF1	ASAH1	NPM1
TXNIP	PRSS23	CYCS	SAMD8	PXDC1	CD200	SNRPB	CD81
CACYBP	RUNX1	HECTD2	COX5B	FAP	DCLK1	NIP7	FILIP1
FSTL1	BIN1	WDR45B	SAR1A	AHNAK2	PPP1R15B	ATP1B3	HLA-A
GNPNAT1	MT-ND6	THBS1	HLA-DRB1	CSRNP1	EIF4G2	HSPA5	EEA1
RANBP2	FAM46A	STK17A	MEST	MEIS2	PPP2R2A	POLR1C	RP11-14N7.2
KLF6	PTGS2	SPRY2	SLC38A2	TSPAN3	KRAS	NR4A1	SLC39A14
ZFAND5	CALM2	IPO5	NRBF2	THAP2	NUP98	LHFP	FOSL2
U2AF1L5	DDX27	CMBL	TUBB6	SLC39A6	IFI27	HMGA1	LAMA4
ITIH5	NSUN2	DUSP5	SPHK1	CLIC2	ANTXR2	SEC31A	OPTN
JMJD1C	HNRNPU	H2AFJ	HLA-DRA	TOB2	COPS2	NR1D2	PAFAH1B1

HOMER1	COL14A1	APBB3	MMP23B	KLF9	MRPS6	PDGFD	NOTCH3
EPHB2	RASAL2	BACH1	S100A16	TMED5	B4GALT1	MYLK	DAZAP2
DCUN1D3	ZNF703	RAP1B	TSHZ2	PFKP	C2	ATF4	ATF3
PLXDC1	KLHL4	CLCF1	APOE	MCL1	MYO1E	PLAU	RASL11A
AES	GPM6B	KCTD20	LDHB	ZBTB16	SCGB3A2	LMOD1	PDPN
RBBP6	UGCG	HMCN1	C8orf4	ATP5D	PNP	SNHG12	TPI1
RELB	FTH1	MFAP5	ABCA1	ABCA9	TINAGL1	TRIB1	ARL6IP4
TNXB	PTP4A3	KITLG	F10	DBN1	GOLGA4	CAST	MIR155HG
HLA-DRB5	TALDO1	DCXR	PFDN5	LRRN4CL	CALU	OLFML2B	CFD
SLC3A2	PTRF	NDUFS5	SPATS2L	NUDT4	SAMHD1	LYZ	RORA
PLAGL1	PPP1R10	NEU1	CFI	WDR83OS	SGCE	EIF4G1	DUSP4
FAM126A	PTN	GUK1	ANTXR1	ACKR3	DBNDD2	CNN1	HIF1A
SFRP1	PTGDS	COL15A1	UGP2	CD82	FGF7	MGST3	PRR13
RPS19	NDUFB10	G3BP1	CAPN2	ARFGAP3	CD4	FNDC3B	UQCR11
RPL22L1	ATP6V0E1	BRD2	FKBP1A	EIF3A	NFIL3	LGALS3BP	CIB1
NDUFV2	CLEC2B	CHN1	NDUFA13	VPS28	S100A6	ZEB2	CD34
MBNL2	GPC3	RRBP1	USMG5	DNAJA4	ANAPC16	LDHA	S100A11
SCPEP1	GGT5	COX5A	EIF3K	NGFRAP1	TCEB2	LINC00657	GDF15
KRT8	MARCKS	SELENBP1	GPCPD1	EDNRB	LXN	ABLIM1	NCL
UQCRB	MFAP2	IL1RL1	CHPF	RDH10	ADIRF	SPTAN1	ADAM12
EGFR	TNS1	TACC1	GPNMB	RGN	GRINA	SYNCRIP	MACF1
SLC7A5	C2orf40	LPL	CLEC3B	NDUFB7	TGFB1I1	COX6B1	VASN
PCOLCE	STAT3	CTSS	LEPR	DKK3	SFRP4	ITGA1	CXCL8
ATP5J	ADGRF5	COMP	MT1A	ROBO2	NME3	MEF2C	LSP1
CCL26	SCN7A	DKK1	RNASE1	SGCA	S100A10	OSR1	AURKAIP1
MXRA8	RSRP1	NPNT	ARL6IP5	PIEZO2	CHRDL1	SLC16A7	SLC2A3
SYPL1	MT1X	HILPDA	TGFBR3	PSME2	CD302	MARCKSL1	TUBA1A

COMT	*KCNMA1*	*CXCL2*	*TBX2*	*PODN*	*BCL3*	*NBL1*
HGF	*DDIT4*	*HOPX*	*NDFIP1*	*04-sept*	*THY1*	*CES1*
CYBA	*SFTPB*	*ABHD5*	*TNFRSF1A*	*CSRP1*	*C7*	*ITGA8*
RBM39	*TYROBP*	*AKR1C1*	*SCARA5*	*IGFBP4*	*ATP6V1F*	*SH3BGRL*

***** Derived from(*41*).

2337 **Table S16, related to Fig.8.** *ACTA2*$^{+}$ myofibroblast marker genes*****.

FN1	*TFPI2*	*FAP*	*CD34*	*MGST1*	*SMPDL3A*	*TNFRSF1A*	*LPP*
LTBP2	*FGFR4*	*CD302*	*LGALS3*	*SOD3*	*CFH*	*ATP13A3*	*ID3*
LIMCH1	*SLC40A1*	*CD248*	*EFEMP1*	*PMP22*	*CPXM1*	*PLN*	*FHL1*
CDH11	*ASPN*	*ARC*	*CTGF*	*ANTXR1*	*SELENBP1*	*MAFF*	*SERPINA3*
ADIRF	*DNAJB1*	*CD55*	*SLC25A4*	*NOLC1*	*HNRNPF*	*EIF4A1*	*CILP*
PLA2G2A	*COL5A2*	*CHD1*	*NCL*	*TCF12*	*FAM162B*	*ARL4D*	*FIBIN*
A2M	*PALLD*	*MDK*	*MYH11*	*ADGRD1*	*IGFBP7*	*MYOC*	*FABP4*
MACF1	*EIF4A3*	*GJA4*	*NR4A2*	*WDR43*	*EZR*	*EGR3*	*C1R*
ITGBL1	*TCF21*	*CALM1*	*COL1A1*	*NAMPT*	*CLCF1*	*RARRES1*	*MAP1B*
CES1	*PLIN2*	*EFHD1*	*ESAM*	*KCTD12*	*MYL6*	*PDK4*	*C2orf40*
HAS1	*MT1M*	*HMGN1*	*NDNF*	*PCBP1*	*PDLIM5*	*SFPQ*	*KIAA1217*
MYC	*G0S2*	*PTP4A1*	*MMP19*	*PRSS23*	*SLC4A7*	*PIK3R1*	*HTRA1*
TM4SF1	*NPNT*	*ITM2A*	*RPL41*	*ABLIM1*	*MIR22HG*	*SPTBN1*	*SRGN*
MOXD1	*HSP90AB1*	*FOSL1*	*HNRNPAB*	*FKBP4*	*WISP2*	*SEMA3C*	*THBS1*
COL6A3	*TMEM119*	*DNAJA1*	*NT5E*	*CXCL12*	*CHMP1B*	*AEBP1*	*TGM2*
MAMDC2	*NR4A3*	*BCAM*	*WT1*	*INPP4B*	*CFB*	*SRSF3*	*SLC2A3*
ROBO2	*ANGPT1*	*ENC1*	*LMO4*	*CLEC3B*	*ACTG2*	*UBC*	*CEBPB*
ERRFI1	*SPINT2*	*TPM2*	*TNC*	*PI16*	*ADAMTS9*	*UGP2*	*SERPINA3.1*
COL8A1	*SLC38A5*	*LSP1*	*MTRNR2L12*	*KRT8*	*ZNF331*	*PHLDA2*	*MGP*
UGDH	*CTHRC1*	*HMOX1*	*ATF3*	*MXRA8*	*LGALS1*	*LMOD1*	*IFI6*
MFAP2	*SELK*	*ISYNA1*	*KLF9*	*PFDN2*	*CREB5*	*CRISPLD2*	*SERPINE1*
CCDC80	*PTGIS*	*OSR1*	*NOTCH3*	*FLNC*	*GABARAPL1*	*LGALS3BP*	*TXNIP*
MEDAG	*ADAMTS1*	*NDRG1*	*PLAU*	*11-sept*	*MEF2C*	*PIM3*	*CXCL1*
CDKN1A	*RGS5*	*3-Mar*	*PCOLCE2*	*ZYX*	*FAM46A*	*IL32*	*FHL2*
EMILIN1	*SFRP1*	*NRP2*	*SRSF2*	*RABGEF1*	*RANBP2*	*ITGA5*	*HIF1A*

GPRC5A	SMOC2	ITGA2	MTHFD2	PPP1R12A	ENO1	NUDT4	BGN
UAP1	DES	EPS8	ELL2	FIGF	YBX3	MT-CYB	FBN1
PLXDC2	LDHA	FKBP1A	FBLN5	OSTC	RP11-14N7.2	NRIP1	PDPN
MT1A	DIO2	SEPP1	MMP2	JUNB	GNL3	ARID5B	THBD
PLEKHH2	NOP16	NDUFA4L2	COL10A1	ITM2C	CCL11	S100A13	RGS16
QSOX1	CRIP1	HSD11B1	EGFL6	ENAH	HNRNPU	MMP14	BTG2
IGF2	TDO2	ETV1	GNG11	WDR1	UACA	HEYL	INHBA
C3	HIGD1B	PTP4A3	CTSB	YWHAG	INSIG1	EDNRA	RASD1
RHOB	LUM	RSPO3	LSAMP	ATP1A1	TUBB3	AKR1C1	CHRDL1
RARRES2	HSPH1	ELN	COL1A2	ACTA2	PLK2	TCF4	KLF2
GPC3	COL16A1	C1QTNF1	SPARC	TPT1	STMN1	TIMP3	C10orf10
SCN7A	DDX21	CNN2	LBH	TUBB2A	RSL1D1	CBLB	TSC22D3
DKK3	TUBB4B	SCARB2	LHFP	PA2G4	HSPB6	MINOS1	FGF7
ITGA8	SGK1	MFGE8	ZNF106	BTG3	ANGPTL4	FMO2	HSPB8
HSPD1	CDC42EP2	TAGLN2	ADGRF5	NPC2	XBP1	HSPA1A	TNFRSF12A
MT2A	CPE	PPIB	NAP1L1	LINC01133	PTMA	DDX3X	MEG3
POSTN	KRT18	HSPA8	SCARA5	CADM3	SNRPB	TXN	EGR1
CD82	TSPAN13	COL5A1	VEGFA	DSTN	F2R	SOCS3	COL12A1
COMP	GDF10	F3	TSPAN8	DNTTIP2	ARL6IP5	FAT1	AC090498.1
IGFBP6	HSP90AA1	C16orf45	ZFAND5	ABL2	MLLT11	SPSB1	PTGDS
EIF1	NKD2	EIF5A	HES4	RPS27	TUBA1B	MT1G	LINC00152
NBL1	IFITM1	ID4	NXT1	FOSL2	HSPB1	VASN	FOSB
MAT2A	DST	C1QTNF7	TIPARP	BAZ1A	HSPA1B	CST3	ZFP36
FST	SLPI	PLPP1	LRRN4CL	SLC16A1	EMP2	IGF1	CFD
COX4I2	ACKR3	FAT4	FHL5	C1QTNF3	RAB31	CYSTM1	CXCL2
HSPE1	ALDH1A3	TUBA1C	GNPNAT1	NR2F1	SH3BP5	PIM1	IGFBP3
ENPP2	SNHG15	PTK7	ALDH2	MMP23B	PDLIM4	EPAS1	SOD2
BAG3	ROBO1	COL15A1	MFAP4	FMO3	HSPA9	HMGA1	PTGS2

LTBP1	*BDKRB1*	*CYP7B1*	*DBNDD2*	*ADAMTS4*	*KLF3*	*CYR61*	*SFRP4*
ATP1B3	*AKAP12*	*STEAP4*	*PDGFRL*	*CEBPZ*	*EIF4E*	*MYO1B*	*CXCL3*
CYCS	*TNFRSF19*	*SRSF7*	*ALDH1A1*	*KLF4*	*CSRNP1*	*IFI16*	*DPT*
BMP5	*MCAM*	*SORBS2*	*SH3PXD2A*	*EDNRB*	*ACTN4*	*MT1X*	*DCN*
CTSL	*CREM*	*NR4A1*	*TOB1*	*NPM1*	*LAMB1*	*RRBP1*	*CRABP2*
GFPT2	*COL3A1*	*EIF1B*	*ETF1*	*KDM6B*	*ISG15*	*MARCKS*	*GPX3*
HMCN1	*SNCG*	*SLC20A1*	*PHLDA1*	*SNU13*	*CSRP2*	*SRPX*	*SFRP2*
MYL9	*PNRC1*	*AMD1*	*RGS3*	*SLIT2*	*PDGFRB*	*TPM1*	*ADH1B*
MFAP5	*LAMA2*	*LITAF*	*APOLD1*	*TCP1*	*NREP*	*TAGLN*	*ADM*
TINAGL1	*GSN*	*TCEB1*	*UBA2*	*CRYAB*	*ZFP36L1*	*COL6A1*	*ICAM1*
RGCC	*EBF1*	*RAN*	*DKK1*	*NOP58*	*PLAUR*	*GPNMB*	*CH25H*
SPON1	*COL13A1*	*H3F3B*	*SH3D19*	*ACTB*	*TXNRD1*	*PPP1R15A*	*PPP1R14A*
ACSL4	*PIEZO2*	*MAOB*	*CNN1*	*CYP1B1*	*TMSB10*	*HILPDA*	
VCAN	*PROCR*	*PMEPA1*	*NRP1*	*WNT2*	*SERTAD1*	*COL18A1*	
IFI27	*MYH10*	*STOM*	*SFTA1P*	*MT1E*	*IGFBP2*	*CXCL8*	

***** Derived from(*41*).

2341 **Table S17, related to Fig. 8.** *PLIN2*$^{+}$ lipomyofibroblast marker genes*****.

CTSL	*AOC3*	*ANGPT1*	*LARP4*	*METAP2*	*SARAF*	*ARF5*	*PLN*
MT-CYB	*EIF4A3*	*RABGEF1*	*KCTD20*	*NABP1*	*EMP3*	*MIR222HG*	*MINOS1*
BGN	*MGST1*	*PA2G4*	*ITGA8*	*NFIL3*	*ANAPC16*	*FAM180A*	*HIST1H4C*
MYL9	*DNAJC2*	*STK40*	*COX5B*	*C1S*	*PRRC2C*	*EIF3M*	*INPP4B*
TAGLN	*LIMA1*	*ZNF800*	*SLC43A3*	*OLFML3*	*ANXA6*	*MT1A*	*GJA4*
ACTA2	*MEG3*	*LINC00473*	*NRIP1*	*PHLDB1*	*RGN*	*NME3*	*ADAMTS9*
UAP1	*FBN1*	*IL1R1*	*THBS1*	*SRM*	*ARPC5*	*FGFR4*	*CNN3*
ACSL4	*NR4A3*	*CCND2*	*CD151*	*PRKCDBP*	*H3F3A*	*CSNK1A1*	*S100A4*
PLIN2	*RNF149*	*DDX27*	*ESYT2*	*NNMT*	*PLSCR1*	*LGALS3BP*	*ADIRF*
TMSB4X	*TSC22D1*	*RSPO3*	*COLEC12*	*PTP4A3*	*ILF2*	*NEAT1*	*LGALS1*
GFPT2	*NDUFA4L2*	*FBL*	*BAG3*	*SRSF1*	*DAZAP2*	*ARL6IP4*	*CNN2*
CRIP2	*MT2A*	*SRGAP1*	*LMOD1*	*TCEB1*	*04-sept*	*CDKN1A*	*ALDH2*
IGF2	*CAV2*	*TMED5*	*SNED1*	*IVNS1ABP*	*CHCHD10*	*APOLD1*	*RUNX1*
PPP1R14A	*ARL4D*	*KDM6B*	*FAM162B*	*AKIRIN1*	*EDNRB*	*NFIA*	*LITAF*
DKK3	*SLC4A7*	*CLDN11*	*FGF2*	*CRIP1*	*ELL2*	*CHURC1*	*OGN*
TPM2	*F3*	*SH3BGRL*	*PIM1*	*BICC1*	*H3F3B*	*RTN4*	*UGCG*
NOP16	*MYH9*	*GPNMB*	*PRDM2*	*SEMA3B*	*TGIF1*	*TCF21*	*HMOX1*
EIF1B	*CSRP1*	*SAT1*	*COX6A1*	*MAMDC2*	*ASAH1*	*SOD3*	*LTBP1*
GPRC5A	*C1R*	*FN1*	*FRZB*	*ADM*	*CTHRC1*	*SH3PXD2B*	*MFGE8*
CXCL12	*PNO1*	*LRRC59*	*TIPARP*	*INTS6*	*CES1*	*NUPR1*	*SLPI*
MT-ATP8	*SRSF2*	*EIF5A*	*B2M*	*CREM*	*CTSF*	*FIS1*	*ETS2*
FST	*THBS2*	*PTP4A1*	*PXDC1*	*CFD*	*PALLD*	*COX7C*	*CLEC3B*
DDX21	*BDKRB2*	*ASPN*	*DBNDD2*	*LURAP1L*	*RNASEK*	*JMJD1C*	*SRGN*
3-Mar	*GNPNAT1*	*MCL1*	*MT1X*	*MYL12A*	*GCLM*	*TMEM47*	*PIK3R1*
MT-CO2	*FLNA*	*PLTP*	*EIF1AX*	*CYCS*	*PTMS*	*CHMP1B*	*HSPA5*
ITM2A	*ATP1B3*	*C1orf21*	*WTAP*	*TWISTNB*	*SLC16A7*	*FCGRT*	*JUND*
SPSB1	*PIM3*	*VASH2*	*TWIST2*	*GABARAPL1*	*RPS29*	*LPP*	*TFPI2*
NCL	*BRIX1*	*HLA-C*	*TSPAN8*	*EIF4E*	*SPAG9*	*SRSF3*	*HSPB8*
DSTN	*HSPD1*	*FAM126A*	*TXNIP*	*MEF2C*	*TFRC*	*GJA1*	*GPC3*

HNRNPAB	SERPINF1	ALDH1A3	EIF3A	TCP1	RAN	HSPB6	S100A13
MYLK	UBC	NR2F2	TUBB2B	ABLIM1	TIMP3	HSPA2	IFITM1
ERRFI1	SFPQ	EDIL3	C2orf40	G3BP1	TGM2	TRIB1	CSRP2
IGFBP7	HNRNPF	DKC1	BZW2	CHN1	EPAS1	PEA15	TM4SF1
MEDAG	NDUFA4	SOD2	ABCA9	PPP1R12A	PDLIM7	PLAT	ARID5B
MT-CO1	ZFP36L2	FGFR1	EFEMP1	TUBA4A	EHD2	RPS26	CH25H
HSP90AB1	COX4I2	DAB2	BCCIP	TGFBR3	SPHK1	MACF1	HAS2
CYP1B1	PAMR1	SLC25A33	PCOLCE	H2AFJ	SNHG12	NREP	DUSP1
FGF7	ARHGDIB	NIP7	SRSF5	PEBP1	NEDD9	MFAP5	HOPX
PDLIM4	SRPX	CTGF	ENO1	HEYL	CTSB	MT1M	PTGDS
FKBP1A	FOSL1	PNRC1	EGR1	MT-ND6	LAMB1	COX7A2	KLF2
MYC	MGST3	C7	TRMT10C	REXO2	RP11-14N7.2	MSRB3	CXCL1
EIF1	TUBB2A	BIN1	SVEP1	ADD3	GSN	PTX3	PDGFRA
MT-ND4L	COL4A1	PAICS	HNRNPDL	MOXD1	EDF1	LRP1	BTG1
AC090498.1	MESDC1	PTGIS	PPP3CA	CLCF1	GLT8D2	NDUFB7	COL6A2
NOP58	DCAF13	EGFR	BCAM	ARPC3	COMP	S100A16	REL
VEGFA	IGF1	NAMPT	FUS	TNFAIP6	ADGRF5	PTN	ELN
SRSF7	NT5E	TUBB6	C10orf10	SDCBP	CCNL1	TCEAL4	NR4A2
WT1	PTRH2	CYBRD1	EXOSC4	TGFB1I1	HMGN2	RRAD	IGFBP2
CALD1	PLBD1	TXNRD1	TXN	BAIAP2	RASL12	IGSF10	S100A10
BTG3	CD82	B4GALT1	TUBB3	PLEKHH2	SORBS2	TUBA1B	FBLN2
MYL6	SH3BP5	CPXM2	SERTAD1	VAMP8	STRAP	MT-ND3	CRABP2
C16orf45	C16orf89	NOTCH3	TPBG	ISYNA1	TIMP2	C1QTNF3	HSPA1B
PDGFRL	HNRNPU	EMILIN2	CCDC109B	NEGR1	TGFBI	UQCR10	PLK2
LSP1	CYP26B1	GPX3	ABHD5	PCBP1	TNS1	DDX24	ARC
EGFL6	NFE2L2	TNXB	INPP1	STAT3	TMEM204	C9orf16	SFRP2
ATP13A3	XBP1	KRT18	RANBP2	INSIG1	F2R	PDGFRB	HSPA1A
PLAU	KLF3	TINAGL1	PLPP3	IPO7	CTSD	SLC39A14	QSOX1
CCDC80	MYH11	DES	RPF2	CREB5	BRD2	ACTG1	COL14A1
ZFP36L1	FSTL1	POSTN	RBM25	TBX2	EIF3K	JUNB	GADD45B

HSPA8	SNU13	ITGBL1	SGCA	CCDC47	ZC3H15	STEAP1	HIGD1B
MAT2A	OSR1	SYNCRIP	OSMR	CTSH	SLC3A2	HLA-DRB1	ID2
CHD1	BZW1	TOP1	PROS1	MIDN	KRT8	PSME1	CXCL3
CEBPZ	CPXM1	PLS3	ST3GAL1	SERTAD2	COX6B1	SCN7A	RGS2
PPDPF	STK17A	POLR1C	HNRNPA0	SNRPB	DDR2	C12orf57	NBL1
NPM1	TNFRSF1A	SLC40A1	TPT1	UGP2	C8orf4	ANK2	CXCL2
ATP5G2	GRPEL1	ABL1	CILP	FAM46A	CFL1	ENAH	RGCC
C3	SEPW1	CD34	GABARAP	FABP5	PRRX1	RARRES1	RHOB
EZR	METRNL	TOMM5	TFAM	ACTN1	UBE2N	ANKRD28	EMP1
AMD1	RFK	SCARA5	DDX3Y	CDH11	RPL22L1	HIF1A	FABP4
LBH	KLF4	TNC	ABCA8	TMEM176B	HLA-DPB1	TSKU	ATF3
NXT1	EDNRA	UCK2	RBM39	COX4I1	PDE5A	TLN1	THBD
CHRDL1	ABL2	IGFBP4	SLC16A1	RCAN2	MYL12B	SMOC2	CTSK
LTBP2	EBF2	EIF2S1	H2AFX	ADAMTS16	TSC22D3	GPM6B	G0S2
BDKRB1	NOP56	FBLN1	IGFBP6	SLC19A2	PARK7	COL15A1	PRG4
LRRN4CL	COL8A1	SLC20A1	SOAT1	HLA-DRA	HNRNPH1	FERMT2	SGK1
ETF1	MPZL1	TSPAN3	CYB5R3	MARCKSL1	ATPIF1	PLXDC2	FHL2
CAV1	COTL1	LIMCH1	SEMA6A	HIPK3	ABI3BP	SNAI2	APOE
WDR43	RGS5	SNRPD1	HMGN3	MYH10	TGFBR2	RAB13	BMP5
CBLB	HSP90AA1	CALM1	HSPA9	HAS1	SPCS1	HCFC1R1	NR4A1
IFI16	NIFK	GTPBP4	SYNGR2	CD4	GUCY1A3	MCAM	NFKBIA
ACKR3	CIRBP	DNTTIP2	TAF1D	PLA2G2A	RBBP6	ESAM	JUN
LDHA	ARPC5L	GLIS3	SPARC	FLNB	COX7A1	TACC1	CTSC
EGR3	BAZ1A	DDX5	EIF5	PITPNB	IL33	MRC2	GEM
KLF9	SERBP1	CFI	CCT2	FOSB	WDR83OS	MSN	PTGS2
ITGA1	A2M	PERP	HMGA1	RDH10	ATP5D	NDUFB10	CFB
PLAUR	TSHZ2	EIF3J	CRIM1	ACTN4	PODN	TMEM70	C11orf96
RPL41	TUBB4B	GSPT1	NME1	APP	PAG1	WFDC1	CNN1
ATP1A1	TUBA1C	STEAP2	PNPLA8	COX8A	SPINT2	ILK	TNFAIP3
CALM2	CD248	NAA50	EIF5B	VAT1	VIMP	NEXN	VCAN

DCN	*DNAJB1*	*IL6ST*	*USP36*	*EIF4A1*	*ACTG2*	*HMGN1*	*ADAMTS4*
SFRP1	*COL4A2*	*FAM198B*	*SPTSSA*	*UQCRB*	*SQSTM1*	*LXN*	*LMCD1*
GNL3	*TMEM176A*	*RIOK1*	*VASN*	*MT-ND2*	*HTRA3*	*MIR22HG*	*SERPINA3*
RSL1D1	*MLLT11*	*TRIO*	*UQCR11*	*SF1*	*TRAPPC1*	*LMNA*	*WISP2*
YWHAG	*MT-ND1*	*NUFIP2*	*ELOVL5*	*KPNA2*	*SNX9*	*TNFAIP2*	*IFI27*
PFDN2	*CPZ*	*ANGPTL4*	*DUSP6*	*CDC42EP2*	*GNG11*	*GAS7*	*COL3A1*
ZNF593	*SEMA3C*	*HSPH1*	*TNFRSF12A*	*WWTR1*	*HLA-B*	*SOCS3*	
UGDH	*RBMS1*	*OAF*	*ANXA1*	*ROBO2*	*FOSL2*	*MAFF*	
MT-CO3	*CD55*	*TXLNG*	*DDX3X*	*AKAP12*	*GUCY1B3*	*CCDC71L*	
ADAMTS15	*MT-ND5*	*SELM*	*SELK*	*LPL*	*ZFAS1*	*PDK4*	
NOLC1	*HRH1*	*MRTO4*	*RERG*	*CTNNAL1*	*NPNT*	*MALAT1*	
DNAJA1	*ITGA5*	*TPM1*	*DCLK1*	*CD9*	*PDPN*	*HSPE1*	
MTRNR2L12	*MT1G*	*CXCL8*	*DKK1*	*RGS16*	*CCL2*	*AKR1C1*	

***** Derived from(*41*).

Table S18, related to Suppl. Fig. 8. Overview of Non-GLP Study CRL 20229915 performed in cynomolgus monkeys with ALE.F02.

Study type and duration of dosing	Species, origin, number of animals	Animal ID	Doses (mg/kg/day)	Administration
Single dose, 42 days	Cynomolgus monkey (Vietnam) 1 male/group	2001	0.3mg/kg	IV bolus
		2002	3mg/kg	IV bolus
		2003	15mg/kg	IV bolus
Repeat dose, 28 days, 4 doses applied weekly	Cynomolgus monkey (Vietnam) 2 males/group	2004 2005	60mg/kg	IV infusion (30 min)
		2006 2007	150mg/kg	IV infusion (30 min)

The following Excel files are available online:

Data file S1. Raw data from figures.

Data file S2, related to Figure 6. CLDN1 interaction partners identified by mass spectrometry in anti-CLDN1 mAb- or Control mAb-treated Huh7 cells.